UNIVERSITY OF CALIFORNIA SAN DIEGO

Regulation of cytoplasmic dynein by LIS1

A Dissertation submitted in partial satisfaction of the requirements
for the degree of Doctor of Philosophy

in

Biochemistry and Molecular Biophysics

by

Kendrick HV Nguyen

Committee in charge:

Professor Andres Leschziner, Chair
Professor Mark Herzik, Co-Chair
Professor Itay Budin
Professor Galia Debelouchina
Professor Elizabeth Komives

2025

The Dissertation of Kendrick HV Nguyen is approved, and it is acceptable in quality and form for publication on microfilm and electronically.

University of California San Diego

2025

DEDICATION

I dedicate this work to my family, my parents Kim and Dennis Nguyen, and my siblings Chelsea, Cody, Kyle, and Karson. Thank you for your unconditional support, encouragement, and the foundation you have given me throughout my life and academic journey. I especially want to thank my mom, Kim, for fostering my curiosity and supporting my learning from the very beginning. I am deeply grateful for your love and support, especially during the most difficult times.

To my friends Noah, Matthew, Stevan, Edgar, Robert, Jon, and Saina, thank you for your friendship and for all the laughter along the way. I truly appreciate your presence and support throughout the years.

To my mentors Andres Leschziner, Mark Herzik, Elizabeth Komives, and Agnieszka Kendrick, thank you for all the support and encouragement you have given me throughout this long scientific journey. Taking a course with Elizabeth Komives during undergrad was what first got me interested in research, and that early spark was what set me down the path toward a PhD and a career in science. Mark Herzik helped build my foundation in protein biochemistry and cryo-EM, and I'm incredibly grateful for the time and care he put into mentoring me as an undergrad.

During my PhD, I've been lucky to have Andres Leschziner as an advisor. His support and guidance helped me grow as a scientist, and he played a key role in helping me refine my cryo-EM skills. He also challenged me to think more deeply and communicate more clearly about science, both in writing and in presentations. I'm also so grateful to Agnieszka Kendrick, who was an essential part of my training during her time as a postdoc in our lab. She taught me so much about the cytoskeletal field, and I really appreciated being able to bounce ideas off her. I learned a ton from those conversations and always enjoyed them.

Each of you has played a meaningful role in shaping the scientist I've become, and I genuinely thank you for that.

TABLE OF CONTENTS

LIST OF FIGURES

LIST OF TABLES

ACKNOWLEDGEMENTS

I would like to express my deepest gratitude to my advisor, Professor Andres Leschziner, for his unwavering support and guidance throughout my PhD. Under his mentorship, I not only learned the technical skills necessary for my research but also how to think critically and independently as a scientist. His support has been instrumental in shaping both my development and confidence as a researcher.

I am equally grateful to my co-advisor, Professor Mark Herzik, for his guidance and mentorship from the early days of my undergraduate research through my graduate studies. His mentorship laid the foundation for my understanding of cryo-EM and protein biochemistry, and his support has played a vital role in my scientific growth.

I would like to thank Professor Samara Reck-Peterson for her invaluable advice and guidance throughout my PhD. I am deeply grateful for the opportunity to learn from her and for the support she provided over the years.

I sincerely thank Professor Agnieszka Kendrick for her continued, generous mentorship throughout my PhD. I am especially grateful for the time and energy she dedicated to teaching me everything I know about dynein and the cytoskeletal field. Her patience, insight, and constant encouragement have left a lasting impact on me.

I am thankful to Dr. Mariusz Matyszewski for his thoughtful advice and support with cryo-EM during my PhD, which greatly enriched my work. I also want to thank Dr. Eva Karasmanis for her continued advice and encouragement, and Dr. Janice M. Reimer for her support early in my PhD, both of whom contributed significantly to my growth as a scientist.

I would also like to thank my committee members, Professor Elizabeth Komives, Professor Galia Debelouchina, and Professor Itay Budin, for their time, support, and thoughtful feedback throughout my PhD. Their expertise and perspectives have helped strengthen my work and guided me toward becoming a better scientist.

I would like to thank the Leschziner, Reck-Peterson, and Herzik labs for their positive and supportive environments, which made this journey more enjoyable. I also thank the cryo-EM community at UC San Diego for fostering a welcoming and collaborative atmosphere to learn and grow in the field. I am additionally grateful to the Molecular Biophysics Training Grant at UC San Diego for supporting my research and professional development.

Chapter 2 in full, is a reprint of the material as it appears in *Nature Structural & Molecular Biology*: *Lis1 relieves cytoplasmic dynein-1 autoinhibition by acting as a molecular wedge*. Karasmanis, E.P.; Reimer, J.M.; Kendrick, A.A.; Nguyen, K.H.V.; Rodriguez, J.A.; Truong, J.B.; Lahiri, I.; Reck-Peterson, S.L.; Leschziner, A.E. The dissertation author contributed significantly to this work.

Chapter 3, in full, is a reprint of the material as it appears in *Nature Structural & Molecular Biology*: *Multiple steps of dynein activation by Lis1 visualized by cryo-EM.* Kendrick, A.A.; Nguyen, K.H.V.; Ma, W.; Karasmanis, E.P.; Amaro, R.E.; Reck-Peterson, S.L.; Leschziner, A.E. The dissertation author contributed significantly to the design, data collection, and analysis in this work.

Chapter 4, in full, has been accepted for publication in *Nature Communications* as *Cryo-EM captures early intermediate steps in dynein activation by LIS1*. Nguyen, K.H.V.; Karasmanis,

E.P.; Kendrick, A.A.; Reck-Peterson, S.L.; Leschziner, A.E. The dissertation author was the first author and primary contributor to this work.

VITA

2020 Bachelor of Science in Pharmacological Chemistry, University of California San Diego

2023 Master of Science in Biochemistry and Molecular Biophysics, University of California San Diego

2025 Doctor of Philosophy Biochemistry and Molecular Biophysics, University of California San Diego

PUBLICATIONS

Karasmanis, E.P., Reimer, J.M., Kendrick, A.A., **Nguyen, K.H.V.**, Rodriguez, J.A., Truong, J.B., Lahiri, I., Reck-Peterson, S.L., Leschziner, A.E. Lis1 relieves cytoplasmic dynein-1 autoinhibition by acting as a molecular wedge. *Nat Struct Mol Biol* **30**, 1357–1364 (2023). https://doi.org/10.1038/s41594-023-01069-6

Kendrick, A.A., **Nguyen, K.H.V.**, Ma, W., Karasmanis, E.P., Amaro, R.E., Reck-Peterson, S.L., Leschziner, A.E. Multiple steps of dynein activation by Lis1 visualized by cryo-EM. *Nat Struct Mol Biol* (2025). https://doi.org/10.1038/s41594-025-01558-w

Nguyen, K.H.V., Karasmanis, E.P., Kendrick, A.A., Reck-Peterson, S.L., Leschziner, A.E. Cryo-EM captures early intermediate steps in dynein activation by LIS1. *Nat Commun* (accepted) (2025). Preprint can be found in bioRxiv: https://doi.org/10.1101/2025.01.10.632485

ABSTRACT OF THE DISSERTATION

Regulation of cytoplasmic dynein by LIS1

by

Kendrick HV Nguyen

Doctor of Philosophy in Biochemistry and Molecular Biophysics

University of California San Diego, 2025

Professor Andres Leschziner, Chair
Professor Mark Herzik, Co-Chair

Cytoplasmic dynein-1 (dynein) is a microtubule-based motor protein that plays a central role in organizing the contents of the cell during both interphase and cell division. Dynein transports various cellular cargos (vesicles, protein complexes, RNAs, organelles, viruses, and others) and plays key roles in spindle positioning, organization, and chromosome movement. For dynein to carry out these functions, it must undergo an activation process, in which dynein is converted from an autoinhibited state (Phi) to an active state. Once activated, dynein assembles into an active transport complex with dynactin and an activating adaptor, forming the dynein–dynactin–activator (DDA) complex, although the exact mechanism of this process is unknown. A critical regulator of dynein is LIS1, a highly conserved protein that has been shown to enhance

dynein activation and assembly both in vivo and in vitro. This thesis presents an interdisciplinary investigation that combines cryo-electron microscopy (cryo-EM) with in vivo and in vitro functional assays to explore how LIS1 enhances dynein's activation. Chapter 2 focuses on the discovery of a novel dynein–LIS1 intermediate called "Chi." In this state, two LIS1 dimers are bound between the motor domains of a dynein dimer. Functional experiments demonstrated that the unique contacts formed in Chi are essential for dynein function in yeast and for the in vitro assembly of active human DDA complexes. Chapter 3 investigates the role of ATP in modulating dynein activation by LIS1. Cryo-EM heterogeneity mining resolved sixteen distinct structures of monomeric dynein and dynein–LIS1 complexes. The results revealed that LIS1 increases dynein's basal ATPase activity and promotes conformations that are structurally compatible with activation. Chapter 4 identifies a previously unknown dynein structure called "Pre-Chi," that could precede Chi in the dynein activation pathway. This state features a single LIS1 dimer interacting with one face of the dynein motor domains. Mutational analysis showed that disrupting this interaction compromises dynein motility, underscoring Pre-Chi's importance in the initial transition of dynein from autoinhibition. Together, the work presented in this thesis provides new insights into the stepwise mechanism by which LIS1 promotes dynein activation. These findings demonstrate the power of cryo-EM combined with biochemical and cellular approaches to uncover the regulatory mechanisms of large molecular machines.

Chapter 1: Introduction to the regulation of dynein activation and assembly by LIS1

1.1 Cytoskeletal microtubule-based transport

For cells to function properly, they need to organize their internal components, including vesicles, protein complexes, RNAs, organelles, and even invading viruses. The organization of these internal components needs to be done at specific time and space in a crowded cellular environment. A complex task at this level cannot be achieved by simple diffusion alone; rather, it depends on a directed transport system along the microtubule cytoskeleton[1–11]. Microtubules are polar and dynamic structures that have faster-growing plus ends typically located closer to the cell periphery and minus ends near the microtubule-organizing centers (MTOCs) adjacent to the nucleus (Fig. 1.1)[12,13]. Two classes of ATP-consuming motor proteins travel along the microtubule tracks, the plus-end-directed kinesins and minus-end-directed dynein. In humans, there are over 45 kinesin genes with multiple isoforms capable of long range cargo transport[14]. In contrast, a single cytoplasmic dynein-1 ("dynein" here), is responsible for all minus-ended cargo transport (Fig. 1.1)[15]. In addition to long-range intracellular transport, microtubules and the motors that travel on them, including dynein, are critical for organizing mitotic spindles, driving chromosome segregation, and mitotic spindle formation. Defects in transport system components are associated with neurodevelopmental and neurodegenerative diseases, and cancer[16].

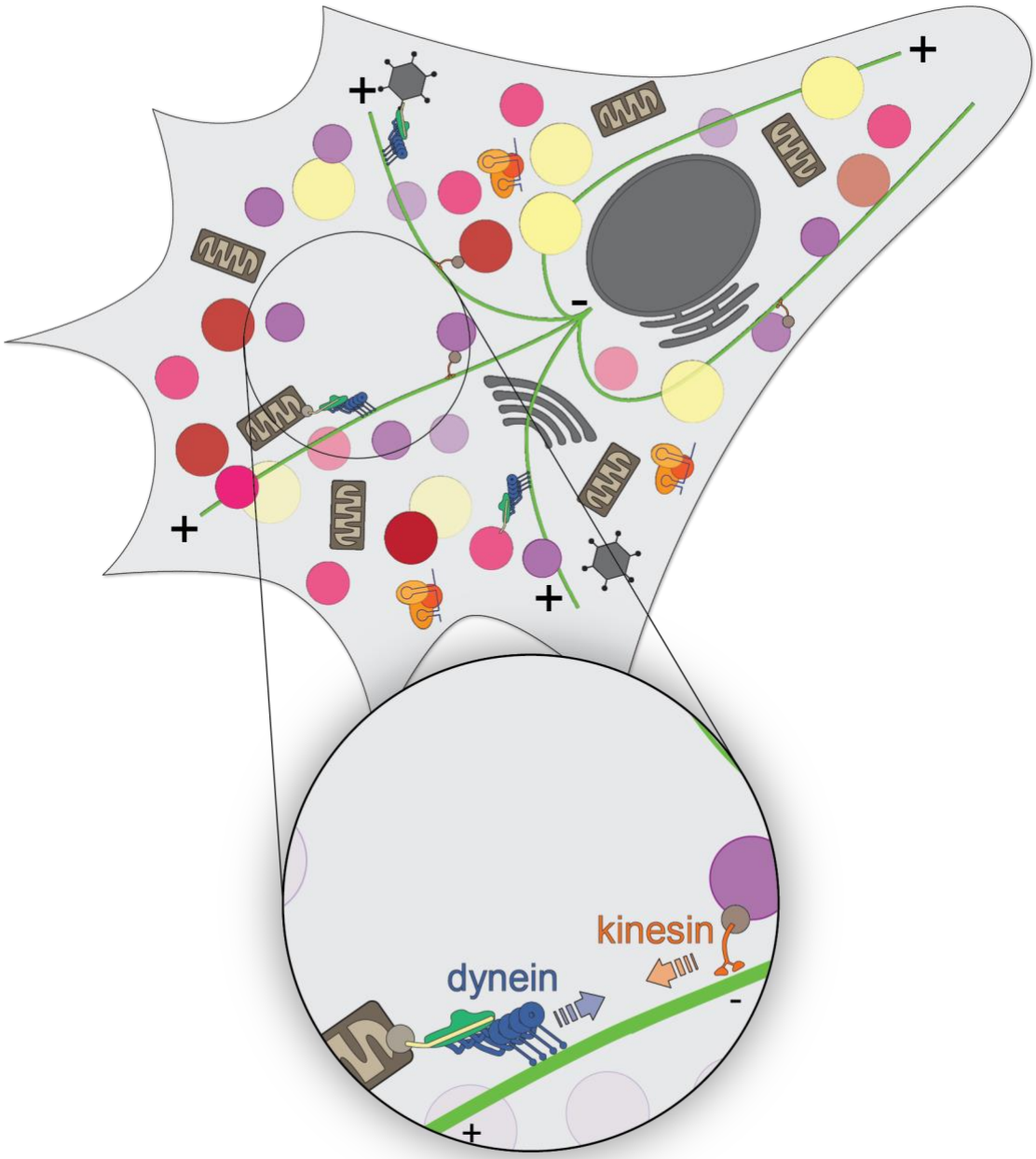

Figure 1.1 Microtubule-based transport. Schematic representation of the microtubule-based transport system in cells. Larger cellular components require active transport for their proper organization. This is provided by the ATP-driven microtubule-based motors dynein and kinesin, which move in opposite directions.

1.2 Cytoplasmic Dynein-1 (dynein)

Dynein is a ~1.4 MDa complex that consists of dimers of six polypeptide chains. The largest chain is called the heavy chain; this chain can be divided into two domains: an N-terminal "tail," which is the dimerization domain, and a C-terminal "motor" domain (Fig. 1.2a-b)[15,17]. Dynein is a member of the AAA+ (ATPases Associated with diverse cellular Activities) family[18], where the motor domain contains a ring of six AAA+ modules, a microtubule-binding domain (MTBD), a stalk connecting the MTBD to the AAA+ ring, a buttress extending from AAA5 that contacts the stalk, and a tail with a flexible "linker" that transmits mechanical forces leading to a power stroke (Fig. 1.2c)[19]. The remaining polypeptide chains are known as the "accessory chains" and bind directly to the tail of dynein. In humans, this consists of two copies each of "intermediate" (IC), "light intermediate" (LIC), and three (TCTEX, LC8, and ROBL) "light" chains (LC) (Fig. 1.2d)[20–23].

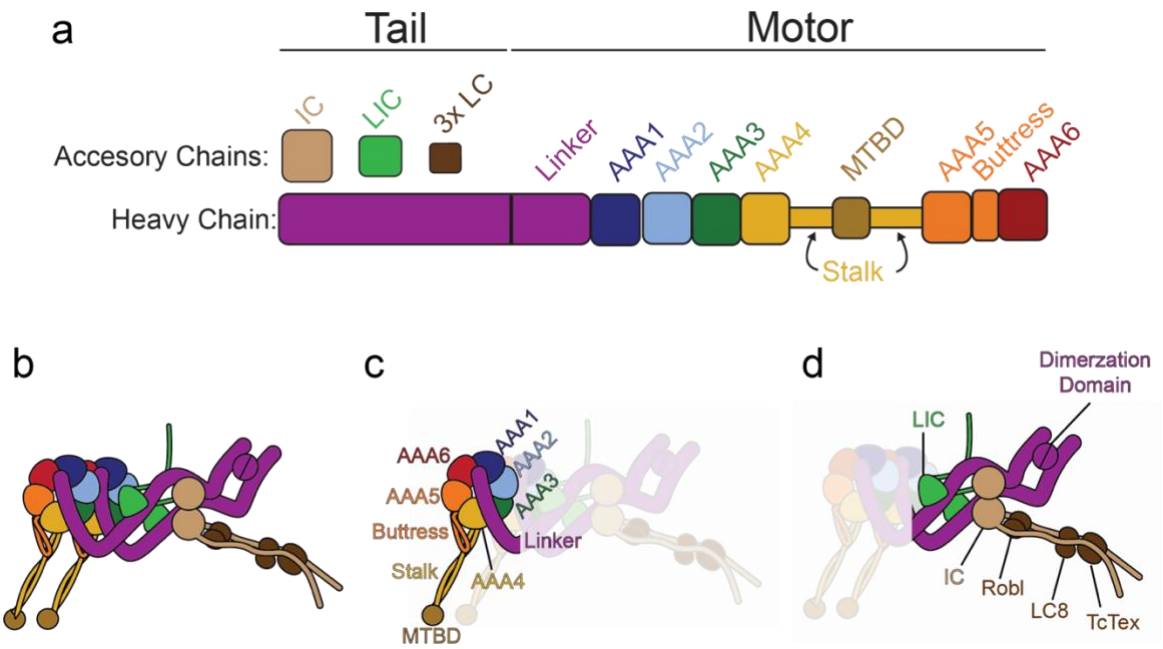

Figure 1.2 Domain organization and structure of dynein. a. Subunit and domain organization of full-length dynein. Individual domains and accessory chains (heavy chain (HC), intermediate chain (IC), light intermediate chain (LIC), and three light chains (LC)) are color-coded. **b.** Schematic representation of full-length dynein dimer with the subunit and domains colored coded the same in a. **c.** A single motor domain is highlighted from the schematic representation in b, with each subunit annotated in the motor domain with their respective color. **d.** The tail domain is highlighted in the schematic representation in b, with each accessory chain and the dimerization domain annotated with their respective color. This figure is adapted from (Nguyen et al., 2025).

Dynein's AAA modules are unique because they are one of the few AAA+ ATPases encoded by a single gene[24–26]. The modules are conserved among other AAA+ ATPases; they consist of an N-terminal "large" subdomain (AAAL) and a C-terminal "small" subdomain (AAAS)[24–26]. ATP binding and hydrolysis occur in a tripartite interface between a module consisting of AAAL and AAAS and a large subdomain from an adjacent AAAL module ($AAAL^{a}$) (Fig. 1.3a-b). AAAL contains a Walker-A motif (or P-loop) that binds the α and ß phosphates of ATP. Additionally, AAAL, has a sensor-I asparagine residue that helps coordinate the water molecule for the nucleophilic attack on the γ-phosphate of the ATP. Lastly, AAAL

contains a Walker-B motif, which has a glutamate residue. During ATP hydrolysis, this glutamate activates a water molecule by deprotonating it, which allows the water molecule to undergo a nucleophilic attack on the γ-phosphate of the ATP. AAAS contributes to the tripartite interface via a sensor-II arginine residue that is also involved in the binding of ATP to the tripartite interface. AAAL[a] contains an arginine finger responsible for stabilizing the transition state of ATP-hydrolysis (Fig. 1.3c-d)[24–26]. In dynein, not all the AAA modules can bind and hydrolyze ATP. Among the six AAA+ modules, four (AAA1, AAA2, AAA3, and AAA4) bind ATP, but only three (AAA1, AAA3, AAA4) hydrolyze it[27–31]. AAA5 and AAA6 have lost their capability to bind and hydrolyze ATP and serve as a structural base for the stalk and buttress[25].

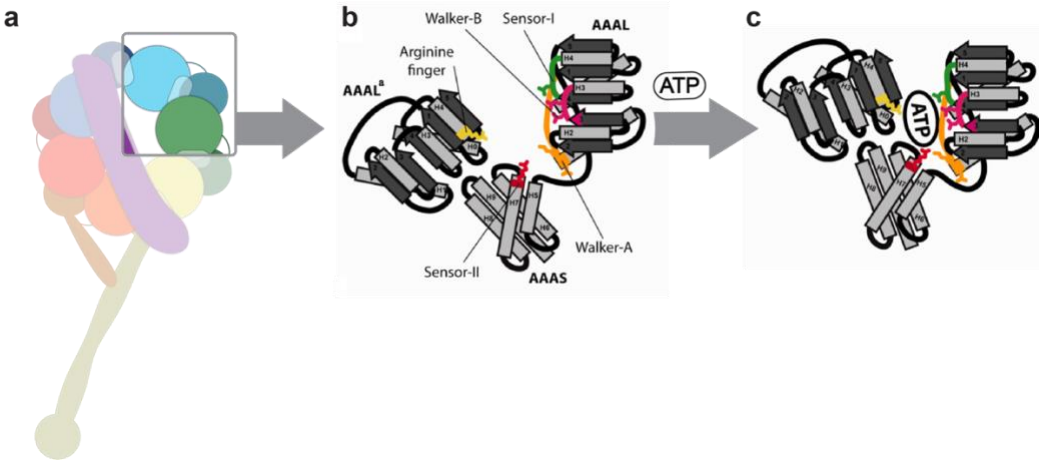

Figure 1.3 ATP tripartite binding interface of a dynein AAA module. a. Dynein monomer motor domain highlighting tripartite interface at AAA2 and AAA3 modules. **b.** Zoom in on the tripartite interface between AAA modules. The nucleotide-binding pocket between the large subdomain (AAAL) and the small subdomain (AAAS) of AAA2 and an adjacent large subdomain (AAAL[a]) of AAA3 is annotated. AAAL contains the Walker-A (orange) and Walker-B motifs (pink) as well as the sensor-I (green). The sensor-II (red) is in the AAAS and the arginine finger (yellow) is associated with the adjacent AAAL. **c.** ATP binding leads to the closure of the binding site and brings the catalytic residues into close contact. This figure is adapted from (Schmidt et al., 2016) and (Kendrick et al., 2025).

AAA+ motor domain of dynein converts the chemical energy of ATP into movement and force via a process called a mechanochemical cycle[19,26]. During this process, ATP binding and

hydrolysis at the primary catalytic site, AAA1, initiate extensive conformational changes. These include the opening and closing of the AAA ring, repositioning of the linker to produce the power stroke, and structural rearrangements in the buttress and the stalk (coiled coils CC1 and CC2) (Fig. 1.4), which modulate dynein's interaction with microtubules via the microtubule-binding domain[28,32,33]. This regulation arises from the relative sliding of CC1 against CC2. The helices within the stalk adopt one of two primary registers, termed α and β, which correspond to high and low microtubule-binding affinities, respectively (Fig. 1.4c-d)[34,35]. The AAA3 and AAA4 modules are allosteric regulators of dynein's mechanochemical cycle[28,33,36].

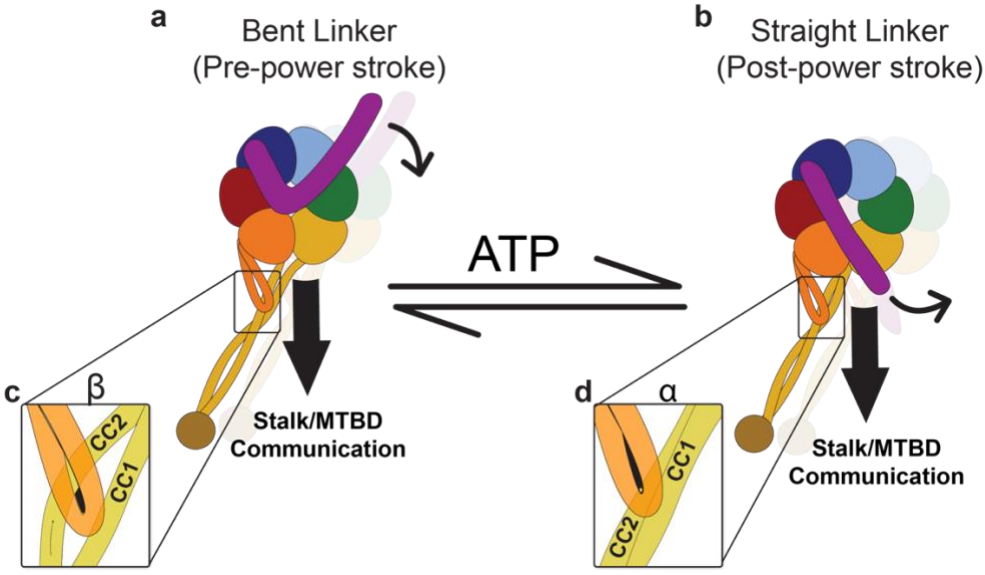

Figure 1.4 Dynein conformational changes under its mechanochemistry cycle. a. Bent linker conformation (Pre-power stroke) of a dynein monomer. **b.** Straight linker conformation (Power-power stroke) of a dynein monomer. **c.** Close-up of the β register from a. **d.** Close-up of the α register from b. This figure is adapted from (Kendrick et al., 2025).

1.3 Dynein activation and assembly

In yeast, and its primary function in this system is to position the mitotic spindle during cell division[17,37]. On the other hand, dynein in higher eukaryotes, such as mammalian cells, has additional essential roles for cellular function. In each case, dynein requires additional cofactors

to form an active transport complex capable of moving along microtubules. This active transport complex comprises one or two dynein dimers (1.4 MDa per dimer), a 23 subunit 1.1 MDa dynactin complex, and a cargo-specific coiled-coil protein called an activating adaptor that links the dynein and dynactin complex to its specific cargo (Fig. 1.5a). This complex is called the Dynein – Dynactin – Activating adaptor complex (DDA) (Fig. 1.5b). There are about 20 known activating adaptors in humans, including BICD2, which links the dynein complex to Golgi-derived vesicles and the nuclear pore complex[15].

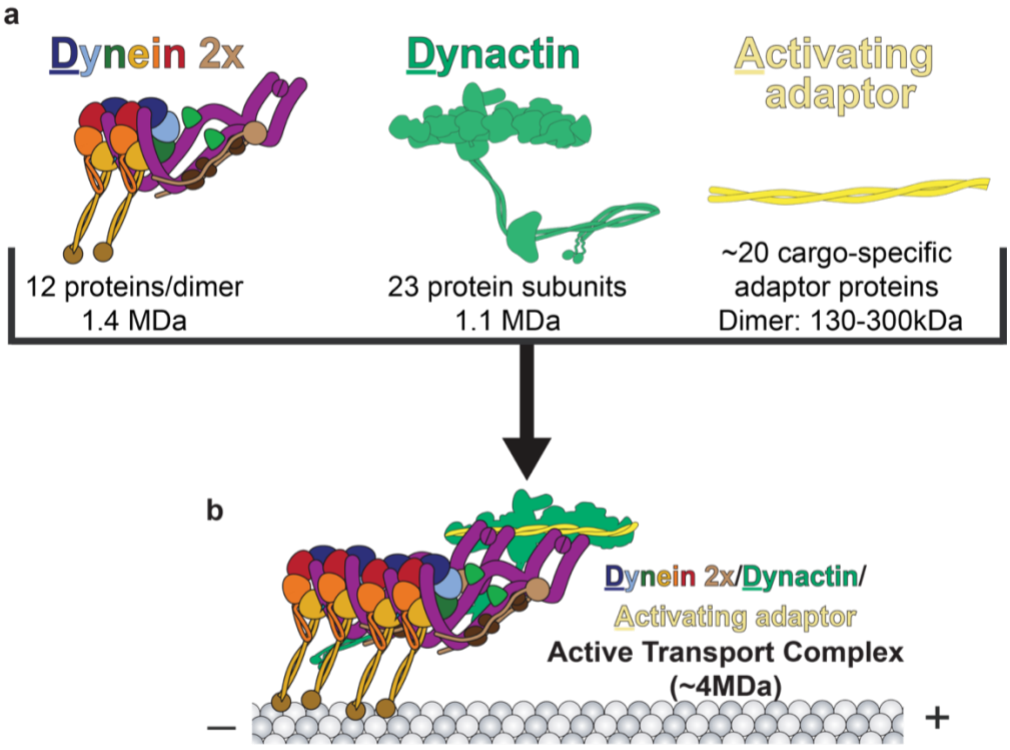

Figure 1.5 Dynein active transport complex and its components. a. Cartoon representation of each component for the dynein active transport complex. This consists of dynein, dynactin, and an activating adaptor. The size and complexity of each is noted below its representative cartoon. Activating adaptors have ~20 different proteins that are cargo specific. **b.** Cartoon representation of an active transport complex or DDA. This figure is adapted from (Nguyen et al., 2025).

1.4 LIS1 and its regulation of dynein

Cellular and structural studies have shown that dynein primarily exists in an autoinhibited pseudo-twofold symmetric state called "Phi" incompatible with binding to microtubules, dynactin, and an activating adaptor, and the relieve from this conformation is regulated by LIS1[22,38,39]. LIS1, an essential dynein regulator, is genetically linked to the dynein pathway from fungi to mammals and is mutated in patients with the neurodevelopmental disease lissencephaly[19,40–42]. LIS1 is a dimer (~90kDa) with an N-terminal LisH domain and a coiled-coil region called LIS1-N, both required for dimerization. The C-termini contain the β-propellers that bind to the dynein motor domain (Fig. 1.6a) [43,44]. LIS1 binds to dynein at two sites, one between AAA3 and AAA4 ($site_{ring}$) and one in the stalk region ($site_{stalk}$) (Fig. 1.6 b-c)[45–49].

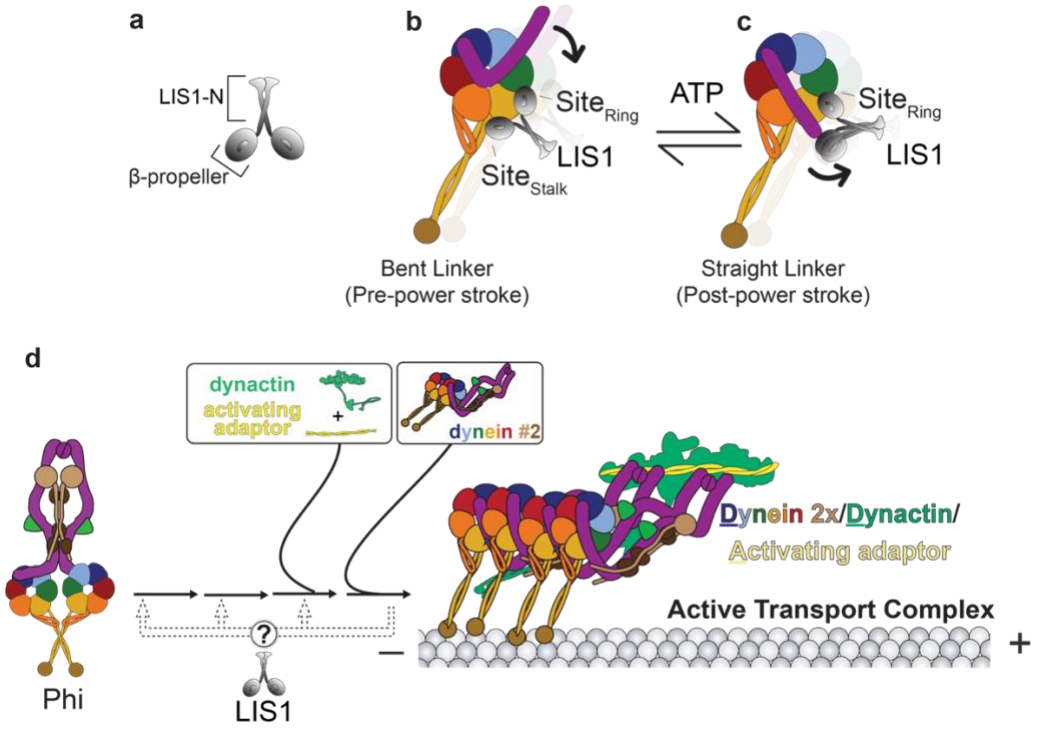

Figure 1.6 LIS1 role in dynein regulation. a. Cartoon model of Lis1. Lis1 is a homodimer consisting of an N-terminal dimerization domain (LIS1-N) and a carboxy-terminal β-propeller domain. **b.** LIS1 binding at $site_{ring}$ and $site_{stalk}$ for Bent linker (Pre-power stroke). **c.** LIS1 binding at $site_{ring}$ at straight linker (Post-power stroke). **d**. LIS1 enhances the dynein activation and assembly, but it is unknown how it does it and the dynein-LIS1 intermediate states or other intermediate complexes involved that are between Phi autoinhibition and an active transport complex. This figure is adapted from (Nguyen et al., 2025) and (Kendrick et al., 2025).

LIS1 is conserved in yeast (*Saccharomyces cerevisiae)*, where it's called Pac1 or Lis1 and in filamentous fungi (*Aspergillus nidulans*), in which it's called NudF. Since this thesis discusses human and yeast systems, I will use the human nomenclature (LIS1) throughout chapters 1 and 5 for consistency, even when referring to the non-human protein. Both dynein and regulators like LIS1 are conserved and non-essential in fungi, making them a model for dynein and dynein regulators[50–52]. Mutations in dynein that block the formation of Phi can partially rescue LIS1 deletion in *Saccharomyces cerevisiae* and the *Aspergillus nidulans*, supporting LIS1's role in relieving dynein's Phi-mediated autoinhibition[50–52]. In addition, in vitro assays

show that LIS1 enhances the formation of DDA complexes containing two dynein dimers, which move faster than complexes containing a single dynein dimer, supporting its role in active dynein complex assembly[48,53,54]. Altogether, LIS1 plays essential roles in the activation of dynein, including relieving autoinhibition and helping assemble the fully active DDA transport complexes (Fig. 1.6d)[48,50–57].

1.5 Outstanding questions and summary of the thesis

A significant conformational change must take place for Phi to be relieved from its pseudo-twofold symmetric conformation and transition into a parallel conformation compatible with forming an active transport complex (Fig.1.6d). However, the mechanism by which dynein transitions from its autoinhibited state to a fully assembled and active DDA transport complex is not yet fully understood. Since LIS1 plays multiple roles in promoting dynein activation and DDA assembly in both in vivo and in vitro systems, several dynein-LIS1 intermediate complexes likely exist. Understanding the structural and functional nature of these intermediates is essential for determining how dynein is activated and assembled by LIS1. To address this, I will use cryo-electron microscopy (cryo-EM) to capture as many intermediate dynein-LIS1 states along the dynein activation and assembly pathway as possible and test their functional consequences in vivo or in vitro. Together, this analysis can provide a mechanistic perspective on how LIS1, a critical dynein regulator, enhances the activation and assembly of dynein.

In Chapter 2, we determined the first example of a dynein-LIS1 intermediate structure in the dynein activation pathway. This structure, termed ‘Chi,’ consists of two yeast dynein motor domains with two yeast LIS1 dimers wedged between them on both faces of the dynein motors. Using a structure-function approach, we showed that Chi-specific interfaces are required for

LIS1's regulation of dynein in *Saccharomyces cerevisiae* in vivo and the formation of active human DDA complexes in vitro. From this data, we propose that Chi is an intermediate state after Phi in the dynein activation pathway (Fig. 1.6d).

Next, we wanted to understand if dynein's mechanochemistry is important for its activation and assembly, given that LIS1 is the only dynein cofactor that binds directly to its motor domain. We wanted to use a structural approach to capture multiple conformations (dynein undergoing its mechanochemical cycle) and composition (LIS1 binding). However, many previously characterized dynein structures (including Chi) were intentionally "trapped" in specific states using mutations or non-hydrolyzable ATP analogs like ATP-Vanadate[23,45–49,56]. While these approaches provided valuable insights, they limited our ability to observe the conformational and compositional landscape of dynein activation and assembly by LIS1. The recent advances in cryo-EM hardware and software have enabled the identification of structural ensembles in samples prepared under native-like reaction conditions[58–66]. We can allow dynein to go through its mechanochemical cycle in the presence of ATP, thus capturing multiple states ("heterogeneity mining"). In Chapter 3, we used this "heterogeneity mining" approach to obtain sixteen high-resolution structures of a monomeric yeast dynein in the presence or absence of yeast LIS1, including seven unique structures from the same dataset. The data support a model where LIS1 increases dynein's basal ATP hydrolysis rate (without microtubules) and promotes conformations compatible with the active transport complex assembly.

To study dynein activation by LIS1 under more physiological conditions, we next wanted to determine the dynein-LIS1 intermediate species during dynein activation. For this, we incubated a sample containing freshly purified full-length human dynein (Phi is predominant

under these conditions), human LIS1, and ATP. We used full-length dynein for two reasons: (1) to observe how the tails rearrange during activation, a key step in forming the DDA complex, and (2) because starting from predominantly Phi state will allow us to capture the earliest dynein-LIS1 intermediates during activation. In Chapter 4, we solved a novel structure of dynein-LIS1 from this sample, in which a single LIS1 dimer is bound to one face of the motor domains of full-length dynein. Since Chi has two LIS1 dimers wedged on both dynein motor faces, we propose that this novel structure precedes Chi; we termed it "Pre-Chi". Mutations that disrupt Pre-Chi led to motility defects in vitro, emphasizing the importance of the Pre-Chi state in the initial relief of dynein autoinhibition.

Since this thesis investigates LIS1's roles in dynein activation using both yeast and human systems, Chapters 2 and 3 focus on yeast and will use the nomenclature Lis1 throughout these chapters. Chapter 4 focuses on the human system and will use the nomenclature LIS1 throughout this chapter. For Chapters 1 and 5, we use the human nomenclature (LIS1) throughout for simplicity, even when referring to the non-human protein.

The work presented in this thesis provides key insights into how LIS1 promotes dynein activation by forming intermediate states like Chi and Pre-Chi. These structures reveal a stepwise mechanism for relieving dynein autoinhibition to assemble it into active transport complexes with dynactin and an activating adaptor. We also show that in the presence of ATP, LIS1 shifts dynein toward more active conformations and increases its basal ATPase activity, further promoting activation. More broadly, this work highlights how combining cryo-EM with in vitro and in vivo assays can reveal the mechanisms of complex molecular machines like dynein and set the stage for future studies on dynein regulation by LIS1 or other cofactors.

1.6 References

1. Lacey, M. L. & Haimo, L. T. Cytoplasmic dynein is a vesicle protein. *Journal of Biological Chemistry* **267**, 4793–4798 (1992).
2. Okada, Y., Yamazaki, H., Sekine-Aizawa, Y. & Hirokawa, N. The neuron-specific kinesin superfamily protein KIF1A is a uniqye monomeric motor for anterograde axonal transport of synaptic vesicle precursors. *Cell* **81**, 769–780 (1995).
3. Nakagawa T, Setou M, Seog D, Ogasawara K, Dohmae N, Takio K, Hirokawa N. A novel motor, KIF13A, transports mannose-6-phosphate receptor to plasma membrane through direct interaction with AP-1 complex. Cell. 2000 Nov 10;103(4):569-81. doi: 10.1016/s0092-8674(00)00161-6. PMID: 11106728.
4. Hirokawa, N. Kinesin and Dynein Superfamily Proteins and the Mechanism of Organelle Transport. *Science* **279**, 519–526 (1998).
5. Schnapp, B. J., Vale, R. D., Sheetz, M. P. & Reese, T. S. Single microtubules from squid axoplasm support bidirectional movement of organelles. *Cell* **40**, 455–462 (1985).
6. Schroer, T. A., Steuer, E. R. & Sheetz, M. P. Cytoplasmic dynein is a minus end-directed motor for membranous organelles. *Cell* **56**, 937–946 (1989).
7. García-Mata, R., Bebök, Z., Sorscher, E. J. & Sztul, E. S. Characterization and Dynamics of Aggresome Formation by a Cytosolic Gfp-Chimera✪. *J Cell Biol* **146**, 1239–1254 (1999).
8. Johnston, J. A., Illing, M. E. & Kopito, R. R. Cytoplasmic dynein/dynactin mediates the assembly of aggresomes. *Cell Motility* **53**, 26–38 (2002).
9. Bullock, S. L. & Ish-Horowicz, D. Conserved signals and machinery for RNA transport in Drosophila oogenesis and embryogenesis. *Nature* **414**, 611–616 (2001).
10. Kanai, Y., Dohmae, N. & Hirokawa, N. Kinesin Transports RNA: Isolation and Characterization of an RNA-Transporting Granule. *Neuron* **43**, 513–525 (2004).
11. Wilkie, G. S. & Davis, I. *Drosophila wingless* and Pair-Rule Transcripts Localize Apically by Dynein-Mediated Transport of RNA Particles. *Cell* **105**, 209–219 (2001).
12. Hyman, A. & Karsenti, E. The role of nucleation in patterning microtubule networks. *Journal of Cell Science* **111**, 2077–2083 (1998).
13. Mitchison, T. & Kirschner, M. Dynamic instability of microtubule growth. *Nature* **312**, 237–242 (1984).
14. Hirokawa, N., Noda, Y., Tanaka, Y. & Niwa, S. Kinesin superfamily motor proteins and intracellular transport. *Nat Rev Mol Cell Biol* **10**, 682–696 (2009).
15. Reck-Peterson, S. L., Redwine, W. B., Vale, R. D. & Carter, A. P. The cytoplasmic dynein transport machinery and its many cargoes. *Nat Rev Mol Cell Biol* **19**, 382–398 (2018).
16. Lipka, J., Kuijpers, M., Jaworski, J. & Hoogenraad, C. C. Mutations in cytoplasmic dynein and its regulators cause malformations of cortical development and neurodegenerative diseases. *Biochemical Society Transactions* **41**, 1605–1612 (2013).
17. Reck-Peterson SL, Yildiz A, Carter AP, Gennerich A, Zhang N, Vale RD. Single-molecule analysis of dynein processivity and stepping behavior. Cell. 2006 Jul 28;126(2):335-48. doi: 10.1016/j.cell.2006.05.046. PMID: 16873064; PMCID: PMC2851639.
18. Mocz, G. & Gibbons, I. R. Model for the Motor Component of Dynein Heavy Chain Based on Homology to the AAA Family of Oligomeric ATPases. *Structure* **9**, 93–103 (2001).
19. Cianfrocco, M. A., DeSantis, M. E., Leschziner, A. E. & Reck-Peterson, S. L. Mechanism and Regulation of Cytoplasmic Dynein. *Annu. Rev. Cell Dev. Biol.* **31**, 83–108 (2015).
20. Urnavicius L, Zhang K, Diamant AG, Motz C, Schlager MA, Yu M, Patel NA, Robinson CV, Carter AP. The structure of the dynactin complex and its interaction with dynein. *Science* **347**, 1441–1446 (2015).
21. Urnavicius L, Lau CK, Elshenawy MM, Morales-Rios E, Motz C, Yildiz A, Carter AP. Cryo-EM shows how dynactin recruits two dyneins for faster movement. *Nature* **554**, 202–206 (2018).
22. Zhang K, Foster HE, Rondelet A, Lacey SE, Bahi-Buisson N, Bird AW, Carter AP. Cryo-EM Reveals How Human Cytoplasmic Dynein Is Auto-inhibited and Activated. *Cell* **169**, 1303-1314.e18 (2017).
23. Chaaban, S. & Carter, A. P. Structure of dynein–dynactin on microtubules shows tandem adaptor binding. *Nature* **610**, 212–216 (2022).
24. Cho, C. & Vale, R. D. The mechanism of dynein motility: Insight from crystal structures of the motor domain. *Biochimica et Biophysica Acta (BBA) - Molecular Cell Research* **1823**, 182–191 (2012).

25. Gleave, E. S., Schmidt, H. & Carter, A. P. A structural analysis of the AAA+ domains in Saccharomyces cerevisiae cytoplasmic dynein. *J Struct Biol* **186**, 367–375 (2014).
26. Schmidt, H. & Carter, A. P. Review: Structure and mechanism of the dynein motor ATPase. *Biopolymers* **105**, 557–567 (2016).
27. Gibbons, I. R., Gibbons, B. H. & Mocz, G. Multiple nucleotide-binding sites in the sequence of dynein. **352**, (1991).
28. Kon, T., Mogami, T., Ohkura, R., Nishiura, M. & Sutoh, K. ATP hydrolysis cycle–dependent tail motions in cytoplasmic dynein. *Nat Struct Mol Biol* **12**, 513–519 (2005).
29. Kon T, Oyama T, Shimo-Kon R, Imamula K, Shima T, Sutoh K, Kurisu G. The 2.8 Å crystal structure of the dynein motor domain. *Nature* **484**, 345–350 (2012).
30. Cho, C., Reck-Peterson, S. L. & Vale, R. D. Regulatory ATPase Sites of Cytoplasmic Dynein Affect Processivity and Force Generation. *Journal of Biological Chemistry* **283**, 25839–25845 (2008).
31. Schmidt, H., Gleave, E. S. & Carter, A. P. Insights into dynein motor domain function from a 3.3-Å crystal structure. *Nat Struct Mol Biol* **19**, 492–497 (2012).
32. Bhabha G, Cheng HC, Zhang N, Moeller A, Liao M, Speir JA, Cheng Y, Vale RD. Allosteric Communication in the Dynein Motor Domain. *Cell* **159**, 857–868 (2014).
33. DeWitt, M. A., Cypranowska, C. A., Cleary, F. B., Belyy, V. & Yildiz, A. The AAA3 domain of cytoplasmic dynein acts as a switch to facilitate microtubule release. *Nat Struct Mol Biol* **22**, 73–80 (2015).
34. Gibbons IR, Garbarino JE, Tan CE, Reck-Peterson SL, Vale RD, Carter AP. The Affinity of the Dynein Microtubule-binding Domain Is Modulated by the Conformation of Its Coiled-coil Stalk. *Journal of Biological Chemistry* **280**, 23960–23965 (2005).
35. Rao, L., Berger, F., Nicholas, M. P. & Gennerich, A. Molecular mechanism of cytoplasmic dynein tension sensing. *Nat Commun* **10**, 3332 (2019).
36. Imamula, K., Kon, T., Ohkura, R. & Sutoh, K. The coordination of cyclic microtubule association/dissociation and tail swing of cytoplasmic dynein. *Proc Natl Acad Sci U S A* **104**, 16134–16139 (2007).
37. Moore, J. K., Stuchell-Brereton, M. D. & Cooper, J. A. Function of Dynein in Budding Yeast: Mitotic Spindle Positioning in a Polarized Cell. *Cell Motil Cytoskeleton* **66**, 546–555 (2009).
38. Amos, L. A. Brain dynein crossbridges microtubules into bundles. *Journal of Cell Science* **93**, 19–28 (1989).
39. Torisawa T, Ichikawa M, Furuta A, Saito K, Oiwa K, Kojima H, Toyoshima YY, Furuta K. Autoinhibition and cooperative activation mechanisms of cytoplasmic dynein. *Nat Cell Biol* **16**, 1118–1124 (2014).
40. Reiner O, Carrozzo R, Shen Y, Wehnert M, Faustinella F, Dobyns WB, Caskey CT, Ledbetter DH. Isolation of a Miller-Dieker lissencephaly gene containing G protein P-subunlt-llke repeats. **364**, 5 (1993).
41. Xiang, X., Osmani, A. H., Osmani, S. A., Xin, M. & Morris, N. R. NudF, a nuclear migration gene in Aspergillus nidulans, is similar to the human LIS-1 gene required for neuronal migration. *MBoC* **6**, 297–310 (1995).
42. Kardon, J. R. & Vale, R. D. Regulators of the cytoplasmic dynein motor. *Nat Rev Mol Cell Biol* **10**, 854–865 (2009).
43. Tarricone C, Perrina F, Monzani S, Massimiliano L, Kim MH, Derewenda ZS, Knapp S, Tsai LH, Musacchio A. Coupling PAF Signaling to Dynein Regulation: Structure of LIS1 in Complex with PAF-Acetylhydrolase. *Neuron* **44**, 809–821 (2004).
44. Kim MH, Cooper DR, Oleksy A, Devedjiev Y, Derewenda U, Reiner O, Otlewski J, Derewenda ZS. The Structure of the N-Terminal Domain of the Product of the Lissencephaly Gene *Lis1* and Its Functional Implications. *Structure* **12**, 987–998 (2004).
45. Huang, J., Roberts, A. J., Leschziner, A. E. & Reck-Peterson, S. L. Lis1 Acts as a "Clutch" between the ATPase and Microtubule-Binding Domains of the Dynein Motor. *Cell* **150**, 975–986 (2012).
46. Toropova K, Zou S, Roberts AJ, Redwine WB, Goodman BS, Reck-Peterson SL, Leschziner AE. Lis1 regulates dynein by sterically blocking its mechanochemical cycle. *eLife* **3**, e03372 (2014).
47. DeSantis ME, Cianfrocco MA, Htet ZM, Tran PT, Reck-Peterson SL, Leschziner AE. Lis1 Has Two Opposing Modes of Regulating Cytoplasmic Dynein. *Cell* **170**, 1197-1208.e12 (2017).
48. Gillies JP, Reimer JM, Karasmanis EP, Lahiri I, Htet ZM, Leschziner AE, Reck-Peterson SL. Structural basis for cytoplasmic dynein-1 regulation by Lis1. *eLife* **11**, e71229 (2022).
49. Reimer, J. M., DeSantis, M. E., Reck-Peterson, S. L. & Leschziner, A. E. Structures of human dynein in complex with the lissencephaly 1 protein, LIS1. *eLife* **12**, e84302 (2023).
50. Marzo, M. G., Griswold, J. M. & Markus, S. M. Pac1/LIS1 stabilizes an uninhibited conformation of dynein to coordinate its localization and activity. *Nat Cell Biol* **22**, 559–569 (2020).
51. Qiu, R., Zhang, J. & Xiang, X. LIS1 regulates cargo-adapter–mediated activation of dynein by overcoming its autoinhibition in vivo. *Journal of Cell Biology* **218**, 3630–3646 (2019).

52. Qiu, R., Zhang, J., Rotty, J. D. & Xiang, X. Dynein activation *in vivo* is regulated by the nucleotide states of its AAA3 domain. *Current Biology* **31**, 4486-4498.e6 (2021).
53. Elshenawy MM, Kusakci E, Volz S, Baumbach J, Bullock SL, Yildiz A. Lis1 activates dynein motility by modulating its pairing with dynactin. *Nat Cell Biol* **22**, 570–578 (2020).
54. Htet ZM, Gillies JP, Baker RW, Leschziner AE, DeSantis ME, Reck-Peterson SL. LIS1 promotes the formation of activated cytoplasmic dynein-1 complexes. *Nat Cell Biol* **22**, 518–525 (2020).
55. Kormanec, J., Schaaff-Gerstenschläger, I., Zimmermann, F. K., Perečko, D. & Küntzel, H. Nuclear migration in Saccbaromyces cerevisiae is controlled by the highly repetitive 313 kDa NUM1 protein. *Molec. Gen. Genet.* **230**, 277–787 (1991).
56. Ton WD, Wang Y, Chai P, Beauchamp-Perez C, Flint NT, Lammers LG, Xiong H, Zhang K, Markus SM. Microtubule-binding-induced allostery triggers LIS1 dissociation from dynein prior to cargo transport. *Nat Struct Mol Biol* (2023) doi:10.1038/s41594-023-01010-x.
57. Markus, S. M., Marzo, M. G. & McKenney, R. J. New insights into the mechanism of dynein motor regulation by lissencephaly-1. *eLife* **9**, e59737 (2020).
58. Zheng SQ, Palovcak E, Armache JP, Verba KA, Cheng Y, Agard DA. MotionCor2: anisotropic correction of beam-induced motion for improved cryo-electron microscopy. *Nat Methods* **14**, 331–332 (2017).
59. Rohou, A. & Grigorieff, N. CTFFIND4: Fast and accurate defocus estimation from electron micrographs. *Journal of Structural Biology* **192**, 216–221 (2015).
60. Punjani, A., Rubinstein, J. L., Fleet, D. J. & Brubaker, M. A. cryoSPARC: algorithms for rapid unsupervised cryo-EM structure determination. *Nat Methods* **14**, 290–296 (2017).
61. Scheres, S. H. W. RELION: Implementation of a Bayesian approach to cryo-EM structure determination. *Journal of Structural Biology* **180**, 519–530 (2012).
62. Scheres, S. H. W. Chapter Six - Processing of Structurally Heterogeneous Cryo-EM Data in RELION. in *Methods in Enzymology* (ed. Crowther, R. A.) vol. 579 125–157 (Academic Press, 2016).
63. Zhong, E. D., Bepler, T., Berger, B. & Davis, J. H. CryoDRGN: reconstruction of heterogeneous cryo-EM structures using neural networks. *Nat Methods* **18**, 176–185 (2021).
64. Kinman, L. F., Powell, B. M., Zhong, E. D., Berger, B. & Davis, J. H. Uncovering structural ensembles from single-particle cryo-EM data using cryoDRGN. *Nat Protoc* **18**, 319–339 (2023).
65. Bepler, T., Kelley, K., Noble, A. J. & Berger, B. Topaz-Denoise: general deep denoising models for cryoEM and cryoET. *Nat Commun* **11**, 5208 (2020).
66. Punjani, A. & Fleet, D. J. 3D variability analysis: Resolving continuous flexibility and discrete heterogeneity from single particle cryo-EM. *Journal of Structural Biology* **213**, 107702 (2021).

Chapter 2: Lis1 relieves cytoplasmic dynein-1 autoinhibition by acting as a molecular wedge

2.1 Results

Structure of a Lis1-mediated dynein dimer

We have previously determined a high-resolution cryo-EM structure of the *S. cerevisiae* dynein motor domain (carrying an E2488Q substitution in the Walker B motif of its AAA3 domain) in the presence of ATP-vanadate and bound to two yeast Lis1 β-propellers, most likely coming from the same Lis1 dimer[1]. Although this data set appeared to consist primarily of particles containing one dynein motor domain bound to one Lis1 dimer, we revisited it to look for other structures. To our surprise, additional data processing revealed several two-dimensional (2D) class averages that contained two dynein motor domains, even though the dynein that we used for cryo-EM sample preparation was engineered to be monomeric. Using this subset of particles, we solved a structure of two dynein motor domains in complex with two Lis1 dimers to 4.1 Å. We called this structure 'Chi' because the dynein conformation resembles the Greek letter Chi and because Chi follows Phi in the Greek alphabet (Fig. 2.1a-b, Supplementary Fig. 2.1, and Table 2.1). In our structure, two dynein motor domains, each bound by a Lis1 dimer, come together through dynein–Lis1 interactions, which, to the best of our knowledge, have not been previously reported. This arrangement is consistent with previous studies that have reported the binding of two Lis1 dimers to dynein in solution[2–4]. In our Chi structure, the closed conformation of dynein's ring and the characteristic bulge in the stalk near its contact site with the buttress indicate a weak microtubule-binding state[5]. The overall structure of each dynein–Lis1 complex is very similar to the structures that we have solved of individual dynein motor domains bound to a Lis1 dimer, also in a weak microtubule-binding state[1,6].

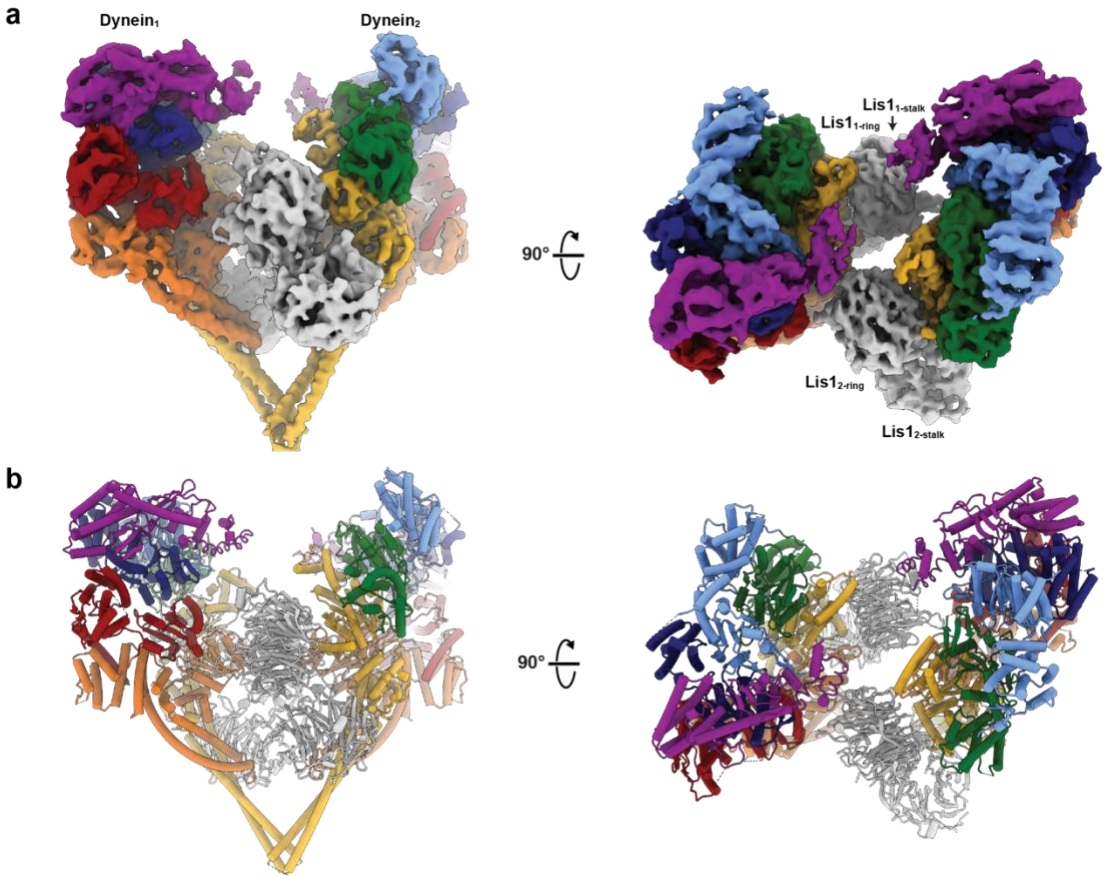

Figure 2.1 Structure of the Chi dynein–Lis1 complex. a. Cryo-EM map of the Chi dynein–Lis1 complex (non-symmetry expanded), shown in two orientations. The different Lis1 β-propellers that bind to previously identified sites on dynein are labeled. **b**, Model of the Chi dynein–Lis1 complex, shown in the same two orientations as in the map in **a**.

Importantly, the Chi conformation is not a consequence of the E2488Q substitution in dynein, or the use of ATP-vanadate in the sample: we also observed Chi in a data set collected from a sample containing wild-type dynein monomer, ATP, and Lis1 (Supplementary Fig. 2.2 and Table 2.1). The presence of only a single class average of Chi in that data set prevented us from obtaining a 3D reconstruction.

Dynein's autoinhibited Phi conformation is characterized by interactions between its two motor domains that make them point in opposite directions (they are effectively 'cross-legged')

(Figs. 2.1b and 2.2a), which prevents the motor from being able to bind to microtubules[7]. The Phi conformation is incompatible with the binding of Lis1 to dynein, as Lis1 bound to one dynein clashes with the second dynein in Phi (Supplementary Fig. 2.3a).

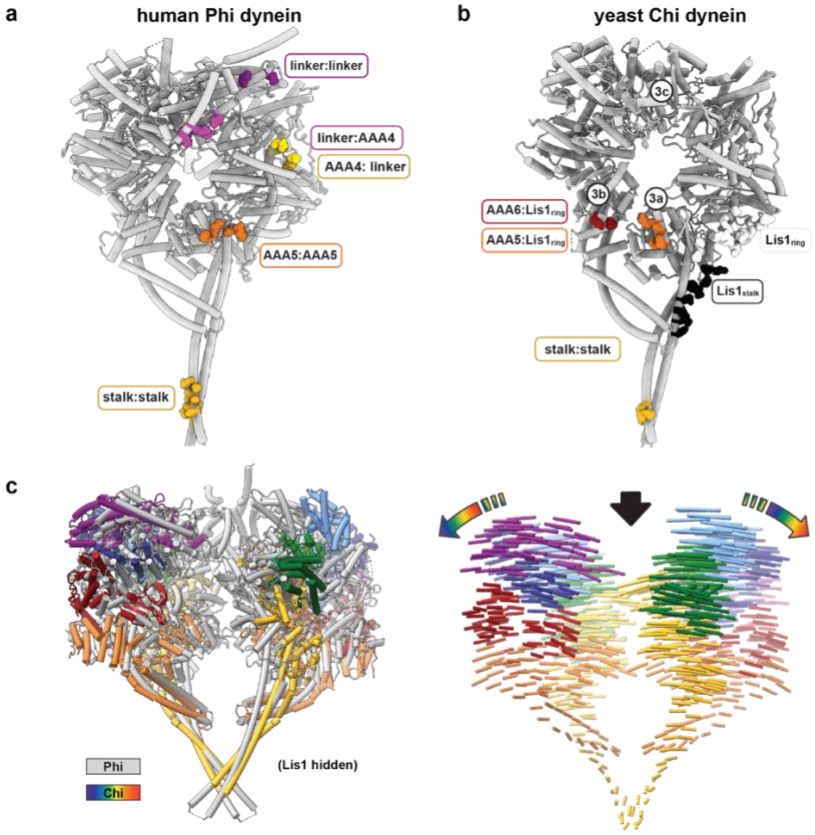

Figure 2.2 Comparison of dynein in Chi and Phi.

a, Interfaces in human dynein involved in stabilizing Phi (PDB: 5NUG). **b**, Interfaces in yeast dynein involved in stabilizing Chi. Note that all but one (stalk–stalk) of the interfaces in Chi also involve Lis1, which we do not show in this panel. The circled labels (1.3a, 1.3b, 1.3c) refer to panels in Figure 1.3, in which interfaces are shown in detail. **c**, Overlay of dynein in Phi (gray) and Chi (rainbow). As in panel (b), we omitted Lis1 in the Chi structure for clarity. The left panel shows the two structures superimposed. The right panel shows interatomic vectors linking equivalent alpha carbons in Phi and Chi. The length of the cylinders is proportional to the displacement of that atom between the two structures.

In Chi, the Lis1 proteins bound to the dynein motor domains act as wedges that keep the two dyneins apart, preventing most of the interactions that stabilize Phi (Fig. 2.2a-b and Supplementary Fig. 2.3b). The one exception is a contact between dynein's stalk helices, which acts as a hinge where Phi opens to accommodate Lis1 and transitions to Chi (Fig. 2.2a-b). The dynein–dynein Phi contacts that are disrupted in Chi are replaced by new contacts between Lis1 bound to $site_{ring}$ on one dynein and the AAA5 (Fig. 2.3a) and AAA6 (Fig. 2.3b) domains of the opposite dynein. The AAA5 and AAA6 Chi-specific interactions involve residues on Lis1's β-propeller that are different from those involved in all previously characterized Lis1–dynein and Lis1–Lis1 contacts (Fig. 2.3d-g). The Lis1 bound to $site_{stalk}$ does not interact with the opposite dynein molecule in Chi (Fig. 2.1a-b).

Figure 2.3 Interactions involved in stabilizing Chi.

a–**c**, Chi is stabilized by three interfaces that, to the best of our knowledge, have not been previously reported: AAA5–Lis1$_{ring}$ (a); AAA6–Lis1$_{ring}$ (b); and a linker–linker interaction (c). In **a**, Chi is viewed from the dynein stalk and towards the motor domain. Figure 1.2b shows the location of these interactions in the context of full dynein. All three panels show the cryo-EM map colored by domain, with Lis1 in gray. The insets show the region of Chi that is highlighted in the main panel. **d**–**g**, Location of interaction interfaces in the Lis1$_{ring}$–Lis1$_{stalk}$ dimer. **d**, Our model of Chi. Dynein is shown in surface representation (filtered to 8 Å), and Lis1 is shown as a ribbon diagram. The area within the square is enlarged in **e**. **e**, Residues involved in the four Lis1 interactions (binding of Lis1 to site$_{ring}$ and site$_{stalk}$, the Lis1–Lis1 dimer interface, and the interactions stabilizing Chi) are shown as sphered and colored by interface. Dynein is shown in white. **f**, The Lis1 dimer is viewed facing the dynein monomer, with which the Lis1–ring and Lis1–stalk interactions are formed. The dynein in front was removed for clarity. **g**, The Lis1 dimer viewed from the other side, facing the dynein monomer with which the Chi-stabilizing interactions are made. The dynein in front was removed for clarity.

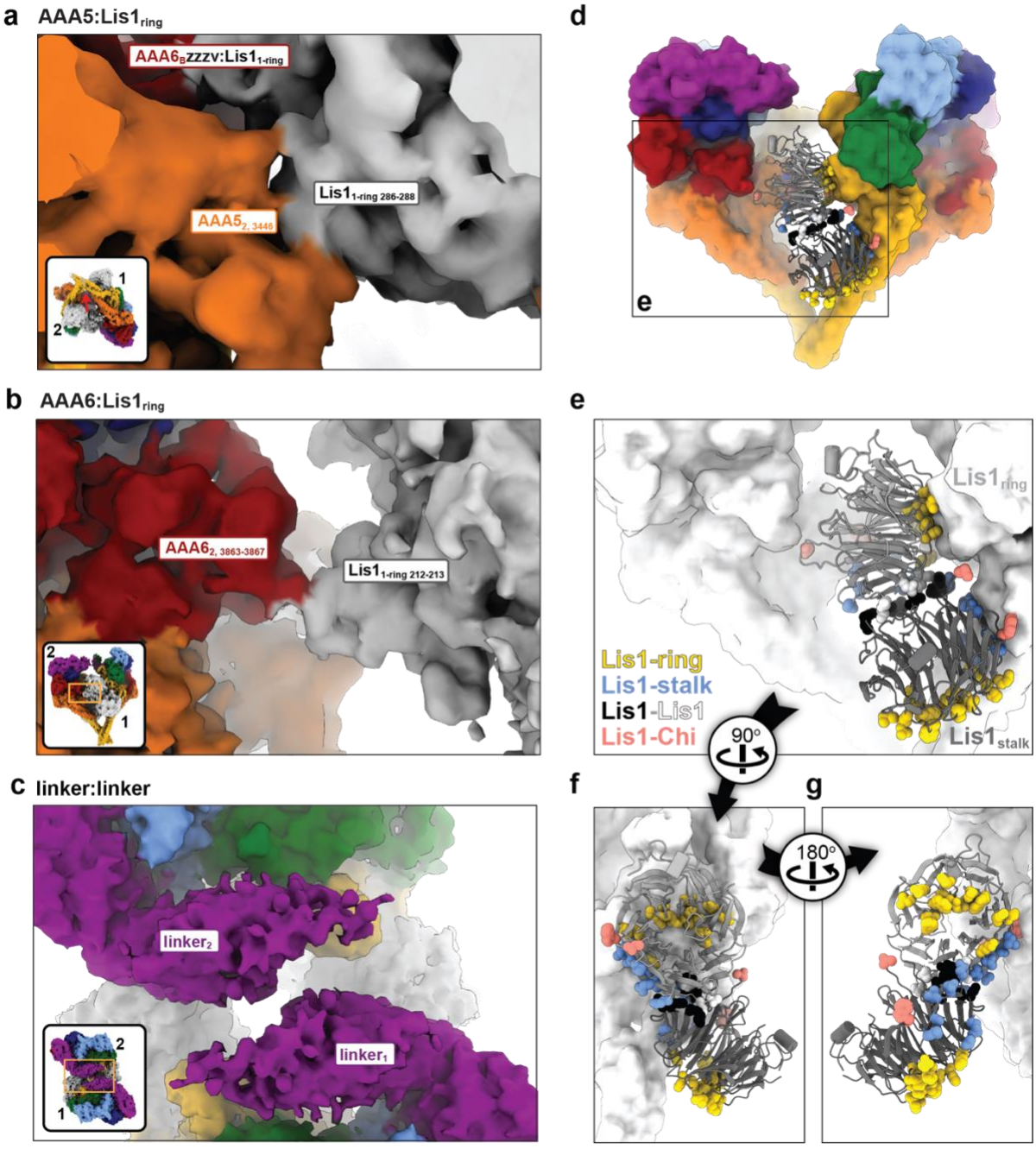
a AAA5:Lis1ring
AAA6BzzzV:Lis1 1-ring
Lis1 1-ring 286-288
AAA5 2, 3446
b AAA6:Lis1ring
AAA6 2, 3863-3867
Lis1 1-ring 212-213
c linker:linker
linker2
linker1
d
e
e
Lis1ring
Lis1-ring
Lis1-stalk
Lis1-Lis1
Lis1-Chi
Lis1stalk
90°
f
g
180°

The differences between Phi and Chi include changes in the conformation of the linker domain (Supplementary Fig. 2.4). In Phi dynein, the linker is bent and docked on AAA2 and AAA3 (Supplementary Fig. 2.4a), which is the same conformation seen in dynein alone in its 'pre-power stroke' state[8]. In contrast, in Chi, the linker is disengaged from AAA2 and AAA3 and shifted towards the opposing dynein molecule (Fig. 2.3c and Supplementary Fig. 2.4b-c); this accommodates the increased distance between the motor domains caused by the presence of Lis1 (Fig. 2.2c). This change in the linker conformation in turn causes a shift in the interface mediating the linker–linker interaction (Fig. 2.3c and Supplementary Fig. 2.4d-f); however, the resolution of the linker domain is too low to determine the exact nature of the residues involved.

The major features of the Chi structure—the disruption of most Phi-stabilizing interactions, a shift in the linker–linker interface, and the dependence of these on the presence of Lis1 and new interactions between Lis1 and dynein—suggest that Chi is an early intermediate in the activation of dynein that provides a mechanistic explanation for the role of Lis1 in this process. We set out to test this hypothesis and validate our structural model in vivo using *S. cerevisiae* and in vitro using recombinant human dynein–dynactin–activating adapter complexes.

Dynein and Lis1 Chi contacts are required in vivo in yeast

We first sought to determine whether the new contact sites between Lis1 and dynein at AAA5 (Fig. 2.4a) and AAA6 (Fig. 2.4b) that form Chi are important for the dynein pathway in vivo. For this, we turned to experiments in *S. cerevisiae*. In yeast, dynein functions to align the mitotic spindle, such that, upon the completion of mitosis, both the mother and daughter cell inherit a nucleus[9–13]. Deletion of the gene encoding dynein (*DYN1*; GeneID: 853928) and dynactin subunits, as well as Lis1, causes nuclear segregation defects that are readily quantifiable

because they produce binucleate cells[14]. To disrupt the Chi-specific interactions (Fig. 2.4a-b), we mutated Asn213 in Lis1 to Ala (Lis1^{N213A}), Trp288 to Asp (Lis1^{W288D}), or both (Lis1$^{N213A\ W288D}$) in the endogenous locus of yeast Lis1 (*PAC1*; GeneID: 854443). Western blots of strains containing FLAG-tagged versions of the mutants confirmed that Lis1^{N213A}, Lis1^{W288D}, and Lis1$^{N213A\ W288D}$ were expressed at wild-type levels (Supplementary Fig. 2.5a-b). We found that, among cells expressing any of these three mutants, the percentage of cells containing two nuclei was increased, similar to cells in which Lis1 was deleted (Fig. 2.4c). We obtained similar results when we disrupted Chi on dynein's side. On the basis of our structure, we introduced F3446A in AAA5 and E3867A in AAA6 (Dyn1$^{F3446A\ E3867A}$; Fig. 2.4a-b). Although we did not build the side chain for E3867 in our model owing to the lower resolution of that part of the map, this residue is a good candidate for mediating the interaction between dynein and Lis1-N213. These substitutions in dynein resulted in an increase in the percentage of binucleate cells similar to that observed following deletion of dynein (Fig. 2.4d). This suggests that the dynein–Lis1 interactions involved in forming Chi are required for Lis1's regulation of dynein in vivo.

Figure 2.4 Role of Chi in dynein's function in vivo in S. cerevisiae.

a, The yeast Chi AAA5–Lis1 $_{ring}$ interface. Trp288 in Lis1 was mutated to Asp. **b**, The yeast Chi AAA6-Lis1 $_{ring}$ interface. Asn213 was mutated to Ala. We did not build the side chain of E3867 beyond its β-carbon owing to the lower resolution of this part of the map. **c**, Quantitation (mean ± s.e.m.) of the percentage of cells displaying an aberrant binucleate phenotype for wild type (WT, dark gray), Lis1 deletion (light gray), Lis1^{N213A} (orange), Lis1^{W288D} (red), or Lis1$^{N213A\ W288D}$ (maroon). WT $n = 12$, ΔLis1 $n = 11$, Lis1^{N213A} $n = 10$, Lis1^{W288D}, and Lis1$^{N213A,\ W288D}$ $n = 8$ biological replicates from independent cultures, with at least 200 cells per condition in each replicate. Statistical analysis was done using a one-way ANOVA with Tukey's multiple comparison test. WT and ΔLis1 ****$P < 0.0001$, WT and Lis1^{N213A}****$P < 0.0001$, WT and Lis1^{W288D} **$P = 0.0001$, WT and Lis1$^{N213A\ W288D}$ ****$P < 0.0001$. Differences not noted are not statistically significant. **d**, Quantitation (mean ± s.e.m.) of the percentage of cells displaying an aberrant binucleate phenotype for wild type (blue), Dyn1 deletion (light blue), Dyn1$^{F3446A,\ E3867A}$ (green), and Dyn1$^{F3446A,\ E3867A,\ D2868K}$ (dark green). $n = 3$ biological replicates, with at least 200 cells per condition per replicate. Statistical analysis was done using a one-way ANOVA with Tukey's multiple comparison test. WT and ΔDyn1 ***$P = 0.0002$, WT and Dyn1$^{F3446A\ E3867A}$ *$P = 0.01$, ΔDyn1 and Dyn1$^{F3446A\ E3867A\ D2868K}$ ***$P = 0.0002$, Dyn1$^{F3446A\ E3867A}$ and Dyn1$^{F3446A\ E3867A\ D2868K}$ *$P = 0.015$. Example images of endogenous dynein localization (*DYN1-3XGFP*) in dividing yeast cells expressing a fluorescently tagged SPB (*SPC110-tdTomato*) component and tubulin (*TUB1-CFP*). Scale bars are three μm. **f**–**h**, Quantification of dynein localization. Graphs show the number (mean ± s.e.m.) of dynein foci per cell localized to the cortex (**f**), SPB (**g**), and microtubule plus ends (**h**) in WT, Lis1Δ, Lis1^{N213A}, Lis1^{W288D}, and Lis1$^{N213A\ W288D}$ yeast strains, from three biological replicates. Statistical analysis was performed on the means of each biological replicate using a one-way ANOVA with Tukey's multiple comparison test. **f**, WT and ΔLis1 **$P = 0.0011$, WT and Lis1^{N213A} ***$P = 0.0007$, WT and Lis1^{W288D} ***$P = 0.0002$, WT and Lis1$^{N213A\ W288D}$ ***$P = 0.003$. **g**,WT and ΔLis1 **$P = 0.0023$, WT and Lis1^{N213A} *$P = 0.0396$, WT and Lis1^{W288D} ***$P = 0.0009$, WT and Lis1$^{N213A\ W288D}$ ***$P = 0.0003$. **h**, WT and ΔLis1 ***$P = 0.0006$, WT and Lis1^{N213A} *$P = 0.02$, WT and Lis1^{W288D} *$P = 0.049$, WT and Lis1$^{N213A\ W288D}$***$P = 0.0039$. n.s. (not significant), $P = 0.069$ to >0.9981. $n \geq 40$ cells per biological replicate; >120 cells total per condition. **i**, Quantitation (mean ± s.e.m.) of the percentage of cells displaying an aberrant binucleate phenotype for wild type (WT, dark gray), Lis1 deletion (light gray), Lis1^{N213A} (orange), Lis1^{W288D} (red), Lis1$^{N213A\ W288D}$ (maroon), Lis1 WT with the Phi-breaking dynein mutant dynein^{D2868K}(striped dark gray), Lis1 deletion with dynein^{D2868K} (striped light gray), Lis1^{N213A} with dynein^{D2868K}(striped orange), Lis1^{W288D} with dynein^{D2868K} (striped red), and Lis1$^{N213A\ W288D}$ with dynein^{D2868K}(striped maroon). The WT condition is the same as in **d**. $n = 3$ biological replicates, with at least 200 cells per condition per replicate. Statistical analysis was done using a one-way ANOVA with Tukey's multiple comparison test. WT and ΔLis1 ****$P < 0.0001$, WT and Lis1^{N213A} **$P = 0.0035$ WT and Lis1^{W288D} *$P = 0.045$, WT and Lis1$^{N213A\ W288D}$ **$P = 0.0014$, ΔLis1 and ΔLis1 with dynein^{D2868K} **$P = 0.0046$, Lis1$^{N213A\ W288D}$ and Lis1$^{N213A\ W288D}$ with dynein^{D2868K} **$P = 0.0036$, Lis1^{N213A} and Lis1^{N213A} with dynein^{D2868K} *$P = 0.0134$, Lis1^{W288D} and Lis1^{W288D} with dynein^{D2868K} *$P = 0.0244$, Lis1$^{N213A,\ W288D}$. Differences not noted are not statistically significant.

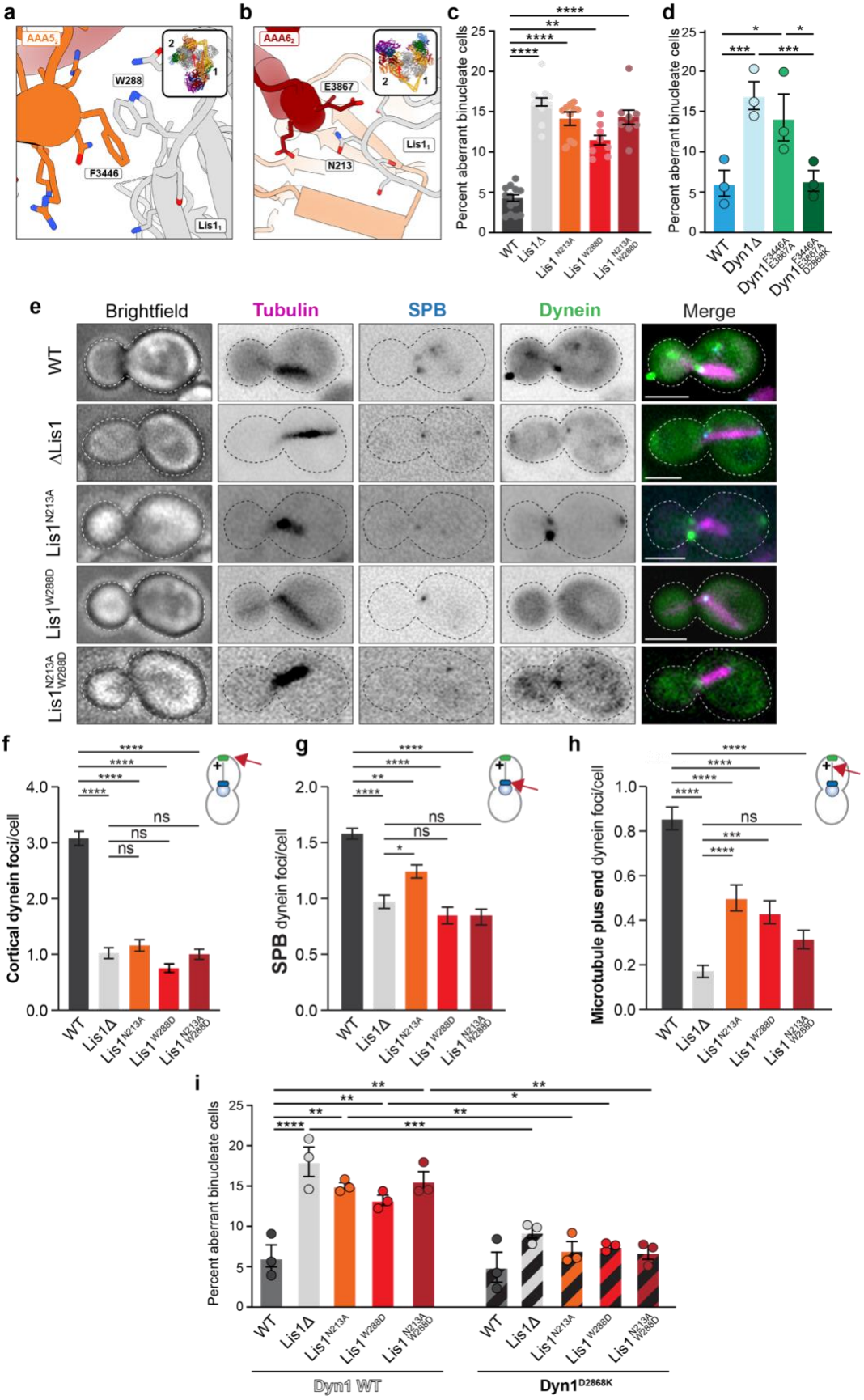
a
AAA5₂
W288
F3446
Lis1₁
b
AAA6₂
E3867
N213
Lis1₁
c
Percent aberrant binucleate cells
WT
Lis1Δ
Lis1 N213A
Lis1 W288D
Lis1 N213A W288D
d
Percent aberrant binucleate cells
WT
Dyn1Δ
Dyn1 F3446A E3867A
Dyn1 F3446A E3867A D2868K
e
Brightfield
Tubulin
SPB
Dynein
Merge
WT
ΔLis1
Lis1N213A
Lis1W288D
Lis1N213A W288D
f
Cortical dynein foci/cell
ns
g
SPB dynein foci/cell
h
Microtubule plus end dynein foci/cell
i
Percent aberrant binucleate cells
Dyn1 WT
Dyn1D2868K

Dynein localization in yeast depends on dynein and Lis1 Chi contacts

Next, we wanted to determine how the Lis1–dynein interactions involved in forming Chi contribute to dynein's localization in yeast cells (Fig. 2.4e-h). Yeast dynein assembles into fully active complexes with dynactin and Num1, the presumed yeast dynein activating adapter, at the cell cortex[9,15]. From this site, active dynein pulls on spindle pole body (SPB)-attached microtubules to align the mitotic spindle, which ultimately favors equal segregation of nuclei between mother and daughter cells. Dynein reaches the cortex by first localizing to microtubule plus ends, through either kinesin-dependent transport or cytosolic recruitment[16–18]. Dynein also localizes to the SPB, where microtubule minus ends are found[17]. Lis1 is required for dynein's localization to all three sites[10,14,19]. To assess how the mutants that target the new interactions between dynein and Lis1 in Chi affect dynein localization, we introduced Lis1^{N213A}, Lis1^{W288D} and Lis1$^{N213A\ W288D}$ at the endogenous Lis1 (*PAC1*) locus. In these strains, dynein, α-tubulin, and a spindle pole body component were also tagged with a fluorescent protein (*DYN1-3XGFP*, *TUB1-CFP*, and *SPC110-tdTomato*, respectively) (Fig. 2.4e)[6,14] and used to measure the number of dynein foci that were found at the cell cortex (Fig. 2.4f), SPBs (Fig. 2.4g), or microtubule plus ends (Fig. 2.4h) in each cell. All three mutants showed a striking reduction in the number of dynein foci at the cell cortex, similar to the strain with Lis1 deletion (Fig.2.4f). Because the cortex is the site of dynein–dynactin–Num1 assembly, these data suggest that the Chi conformation is important for the assembly of active dynein complexes in vivo. All three mutants also significantly affected the ability of dynein to localize to microtubule plus ends. One mechanism dynein uses to reach microtubule plus ends is through kinesin transport in a complex that also contains Lis1 and Bik1/CLIP170[10,20,21]. Thus, it is possible that this transport complex

uses the dynein–Lis1 interactions we identified in Chi, or potentially the Chi conformation itself. Together, our data show that the contacts we observe between dynein and Lis1 in the Chi structure are required for active dynein complex assembly and function in vivo.

Phi-disrupting mutations bypass the need for Chi in yeast

We hypothesize that Chi follows Phi as an intermediate in dynein's activation pathway. This model predicts that mutations that prevent dynein from forming the autoinhibited Phi conformation should bypass the need for Chi to form. We tested this using genetic epistasis experiments. We generated yeast double mutant strains containing each of our Chi-breaking Lis1 substitutions (Lis1^{N213A}, Lis1^{W288D}, or Lis1^{N213A,W288D}) combined with a Phi-breaking substitution in the endogenous dynein/*DYN1* locus (dynein^{D2868K})[22], and performed nuclear segregation assays. In agreement with our model, introducing dynein with the Phi-breaking substitution into the strains carrying the Chi-breaking Lis1 mutants restored the percentage of cells with two nuclei to wild-type levels (Fig. 2.4i). We observed the same when dynein^{D2868K} was introduced into the Lis1-deletion strain (Fig. 2.4i). Introducing the Phi-breaking substitution into dynein already carrying Chi-disrupting alterations (dynein$^{F3446A\ E3867A\ D2868K}$) also fully rescued the increase in the percentage of binucleate cells (Fig. 2.4d).

Dynein and LIS1 Chi contacts are required for human dynein complex assembly

To assess the importance of the Chi conformation, or more generally of the new dynein–Lis1 interaction involved in stabilizing it, in the assembly of active human dynein–dynactin–activating adapter complexes at the molecular level, we next turned to reconstituting the complexes using human proteins. In vitro, human Lis1 protein (herein, LIS1) enhances the

formation of dynein–dynactin–activating adapter complexes containing two dynein dimers, which move faster than the single dynein dimer complexes that form in the absence of LIS1[2,23]. To do this, we first had to identify Chi-disrupting substitutions in human LIS1 that were predicted to be equivalent to the ones we identified in yeast. Directly overlaying our recent structure of a human dynein–LIS1 complex[24] onto each motor domain of yeast Chi did not work, as LIS1 bound to site$_{ring}$ is too far away from the opposite dynein to form the Chi-stabilizing interactions with AAA5 and AAA6 (Fig. 2.5a). This difference is due to human LIS1 having shorter peripheral loops and being slightly rotated relative to yeast Lis1[24] when bound to dynein. To circumvent this problem, we modeled human Chi by aligning a copy of our structure of human dynein bound to two LIS1s to each motor domain in Chi dynein, and then manually moving the models so that they were within interacting distance while still maintaining the stalk–stalk interaction observed in both Chi and Phi dynein. Using this model, we made two sets of human LIS1 substitutions: p.N203A, p.D205A, and p.Y225A to disrupt both the LIS1–AAA5 and LIS1–AAA6 interfaces, and p.N203A, p.D205A, and p.D245A to disrupt the LIS1–AAA6 interface alone. Two of the sites we mutated in human LIS1, N203 and D245, are also conserved in yeast; Y225 corresponds to the W288 that we mutated in yeast Lis1 (Supplementary Fig. 2.6a).

Figure 2.5 Role of Chi in human dynein's ability to move on microtubules.

a, A model of the human Chi $AAA6_2$ and $AAA5_2$–$LIS1_1$ interface. The arrow in the inset indicates the area highlighted in the main panel. **b**, Single-molecule velocity (median ± interquartile range) of TMR–dynein–dynactin–BICD2 complexes in the absence (white circles) or presence (black circles) of different human LIS1 constructs. The data points are represented as triangles, circles, squares, and hexagons corresponding to single measurements within each technical replicate. Four technical replicates were collected for each condition, and the number of data points (n) per each replicate is listed (no LIS1, $n = 142, 91, 152, 131$; LIS1, $n = 147, 118, 119, 120$; $LIS1^{N203A\ D205A\ Y225A}$, $n = 149, 91, 120, 103$; $LIS1^{N203A\ D205A\ D245A}$, $n = 147\ 109\ 128\ 108$). No LIS1 and LIS1 $***P = 0.0002$, LIS1 and $LIS1^{N203A\ D205A\ Y225A}$ $**P = 0.0051$, LIS1 and $LIS1^{N203A\ D205A\ D245A}$ $**P = 0.004$. One-Way ANOVA with Tukey's multiple comparison test. **c**, Processive runs (mean ± s.e.m.) of TMR–dynein–dynactin–BICD2 complexes in the absence (white circle) or presence (black circle) of different unlabeled human LIS1 constructs. The data points are represented as triangles, circles, squares, and hexagons corresponding to single measurements within each technical replicate. Four replicates per condition were collected, and the number of data points (n) per each replicate is listed (no LIS1, $n = 14, 20, 20, 8$; LIS1, $n = 7, 16, 7, 5$; $Lis1^{N203A\ D205A\ Y225A}$, $n = 15, 7, 16, 9$; $Lis1^{N203A,\ D205A\ D245A}$, $n = 17, 9, 17, 9$). No LIS1 and LIS1 $*P = 0.023$. One-Way ANOVA with Tukey's multiple comparison test. **d**, Representative kymographs from single-molecule motility assays with purified TMR–dynein–dynactin–BICD2 in the absence (white circle) or presence (black circle) of different human LIS1 constructs. Scale bars, 10 μm (x) and 40 s (y). **e**, Schematic of the hypothesis for how Lis1 relieves dynein autoinhibition.

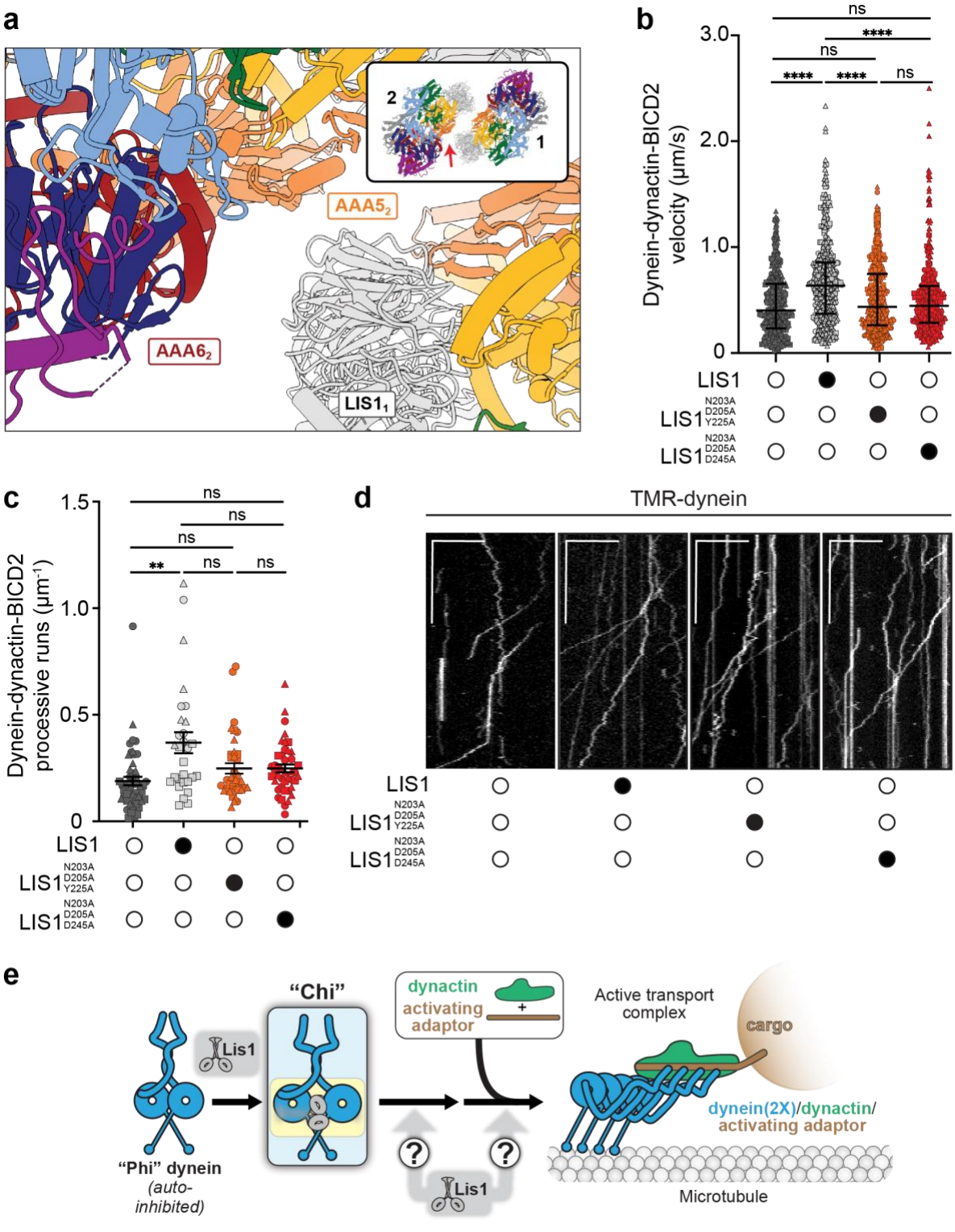
a
AAA5$_2$
AAA6$_2$
LIS1$_1$
2
1
b
Dynein-dynactin-BICD2 velocity (μm/s)
3.0
2.0
1.0
0
ns
****
ns
****
****
ns
LIS1
LIS1 N203A D205A Y225A
LIS1 N203A D205A D245A
c
Dynein-dynactin-BICD2 processive runs (μm^{-1})
1.5
1.0
0.5
0
ns
ns
ns
**
ns
ns
LIS1
LIS1 N203A D205A Y225A
LIS1 N203A D205A D245A
d
TMR-dynein
LIS1
LIS1 N203A D205A Y225A
LIS1 N203A D205A D245A
e
"Chi"
dynactin activating adaptor
+
Active transport complex
cargo
Lis1
"Phi" dynein
(auto-inhibited)
?
?
Lis1
dynein(2X)/dynactin/ activating adaptor
Microtubule

Next, we purified these mutant human LIS1 constructs (Supplementary Fig. 2.6b) and examined their ability to activate human dynein–dynactin complexes containing the BICD2 activating adapter in single-molecule motility assays. In these assays, activation of motility is read out by observing an increase in dynein complex velocity in the presence of LIS1, which results from the enhanced formation of dynein complexes containing two dynein dimers[2,23,25]. As we have shown previously, pre-incubation of dynein–dynactin–BICD2 with 300 nM wild-type human LIS1 increased the velocity and number of processive runs of these complexes (Fig. 2.5b-d)[23]. By contrast, there was no significant difference between dynein velocity and the number of processive runs when dynein–dynactin–BICD2 complexes were pre-incubated with the two human LIS1 mutants ($LIS1^{N203A\ D205A\ Y225A}$ and $LIS1^{N203A\ D205A\ D245A}$), as compared with complexes that were formed in the absence of LIS1 (Fig. 2.5b-d). We also observed an increase in the number of diffusive events in the presence of LIS1 mutants (Supplementary Fig. 2.6c). These data indicate that the dynein–Lis1 contact sites found in the Chi structure are important for human LIS1's role in forming the activated human dynein–dynactin–activating adapter complex, either by relieving the autoinhibited Phi conformation or by playing a role in a later step in the assembly of activated complexes, or a combination of both.

2.2 Discussion

On the basis of the data presented here, we propose that Chi is an intermediate state in the dynein activation pathway, providing the first structural and mechanistic explanation for how Lis1 relieves dynein autoinhibition. We propose that the wedging of Lis1 between the two dynein motor domains primes dynein for binding dynactin and activating adapter protein(s).

The Chi conformation has important implications for dynein activation. In dynein's autoinhibited Phi state, the 'tails,' which precede the motor domain, make many contacts with each other until they reach their 'neck' region, where they move away from each other before rejoining again at the linker domain. Switching to the active dynactin-bound form requires the tail to undergo a large conformational change that turns the loose twofold symmetry present in Phi into the translational ('parallel') symmetry dynein adopts when bound to dynein and an activating adapter (Fig. 2.5e). This rearrangement involves breaking the linker–linker contacts, as well as many of the interactions between the tails and associated chains. We hypothesize that the Chi conformation primes dynein for binding dynactin and an activating adapter protein by stabilizing an intermediate conformation of the tail. In Chi, binding of Lis1 forces the linkers apart, which would cause some of these interactions to break. This would pull the dynein heavy chains apart from each other, disrupting the neck and potentially transmitting conformational changes all the way up the tail.

2.3 Methods

Electron microscopy sample preparation

Grids were prepared and imaged as previously described[1]. Briefly, monomeric yeast dynein^{E2488Q} was randomly biotinylated using water-soluble Sulfo ChromaLink biotin and then dialyzed into TEV buffer. Grid samples containing 150 nM dynein^{E2488Q}, 650 nM Lis1, 1.2 mM ATP, and 1.2 mM Na_3VO_4 were applied to streptavidin affinity grids and vitrified[26,27].

For the imaging of wild-type yeast dynein monomer in the presence of ATP and Lis1, purified fresh dynein (not frozen) was incubated with apyrase for 30 min (apyrase, 0.1 U mL^{-1}, NEB) prior to gel filtration on a Superose 6 Increase column pre-equilibrated in buffer

containing 50 mM Tris, pH 8, 150 mM KCl, 2 mM EDTA, and 1 mM DTT. Eluted protein was concentrated to about 5 μM and diluted 1:1 with Lis1 or TEV buffer and incubated on ice for 10 min (final concentrations: 2.5 μM dynein, 2.5 μM Lis1). After an additional 30-s incubation on ice in the presence of ATP (final concentration: 1.25 mM ATP) samples were applied to plasma-cleaned (Solarus, Gatan) UltrAuFoil Holey Gold R 1.2/1. μM3 grids (Quantifoil). A vitrobot (FEI) was used to blot excess sample and plunge freeze the grids in liquid ethane. Grids were stored in liquid nitrogen until they were ready to be imaged.

Electron microscopy image collection and processing

Details on image collection and initial processing have been reported elsewhere[1]. Following particle picking in crYOLO[28], particles were extracted and binned to 3.93 Å pixel^{-1} in Relion 3.0[29]. Multiple rounds of 2D classification were carried out first in Relion 3.0 and subsequently in cryoSPARC[30] to remove bad particles. Some class averages showed particles with more than one dynein molecule. Using particles from all good 2D classes, initial ab initio reconstructions failed to reconstruct a volume containing more than one dynein molecule. Particles belonging to 2D class averages that potentially contained more than one dynein molecule were manually selected and used in an ab initio reconstruction that resulted in an initial map for Chi dynein bound to Lis1. This volume was used together with our previously published map of monomeric dynein^{E2488Q} bound to Lis1 (EMDB-23829) to separate monomeric dynein^{E2488Q} from Chi dynein using heterogeneous refinement. We performed one additional round of heterogeneous refinement to further remove any monomeric dynein molecules. Using our final particles, we ran non-uniform refinement with C_2 symmetry and optimized per-group CTF parameters enabled to give us a 4.1-Å map.

Wild-type yeast dynein monomer incubated in the presence of ATP and Lis1 was imaged using a Talos Arctica operated at 200 kV and equipped with a K2 Summit direct electron detector (Gatan). Automated data collection was performed using Leginon. A total of 4,525 movies was collected at ×36,000 magnification (1.16 Å pixel^{-1}). The dose was ~4.63 e^{-} Å^{-2} s^{-1} with a total exposure time of 11 s divided into 200 ms frames, for a total of 40 frames. The defocus range was set to 0.8–2.4 µm. All movies were aligned in CryoSPARC live[31] using MotionCor2[32] of the dose-weighted frames. CTF was estimated in dose-weighted images using CTFFIND4[33]. Images with CTF fits worse than 5 Å were excluded from further processing. Particles were initially selected using blob finder in CryoSPARC, and these peaks were used for Topaz model training and final particle picking using Topaz[34]. Particles were extracted and binned to 4.64 Å pixel^{-1}. Multiple rounds of 2D classification, with a varying number of online-EM interactions (30–40) and a batch size per class of between 200 and 400 dependent on the number of particles in each classification were carried out in cryoSPARC to remove bad particles.

Model building and refinement

Symmetry expansion followed by local refinement was used to improve the overall resolution of the motor domain to 3.6 Å. The yeast dynein^{E2448Q}–(Lis1)$_2$ model (PDB:7MGM) was docked, and rigid body fit into the map using Phenix real space refine[35]. Discrepancies between the model and map were fixed manually in COOT6[36] and then refined using a combination of Phenix real space refine and Rosetta Relax (v.13)[37]. Once the monomer model was finished, it was placed in the original map and refined using a similar strategy.

The resolution of the Chi map did not allow us to distinguish between ATP and ADP.Vi. Therefore, we chose to model ATP at AAA1, AAA2, and AAA3, to be consistent with our previously published structure of the yeast dynein motor domain bound to two Lis1s, which was obtained from the same data set[1].

Cloning, plasmid construction, and mutagenesis

The pDyn1 plasmid (pACEBac1 expression vector containing insect cell codon-optimized dynein heavy chain (*DYNC1H1*) fused to a His-ZZ-TEV tag on the amino terminus and a carboxy terminal SNAPf tag (New England Biolabs) and the pDyn2 plasmid (the pIDC expression vector with codon-optimized *DYNC1I2*, *DYNC1LI2*, *DYNLT1*, *DYNLL1*, and *DYNLRB1*) were a gift from A. Carter (LMB-MRC). The pDyn1and pDyn2 plasmids were recombined in vitro with a Cre recombinase (New England Biolabs) to generate the pDyn3 plasmid. The presence of all six dynein chains was verified by PCR. The pFastBac plasmid with codon-optimized human full-length Lis1 (*PAFAH1B1*) fused to an N-terminal His-ZZ-TEV tag was a gift from A. Carter (LMB-MRC). The BICD2s construct (amino acids 25–398) fused to sfGFP on the N terminus and inserted into a pET28a expression vector was obtained as described previously[38]. Substitutions in LIS1 were made using a multi-site-directed mutagenesis kit (Agilent) and the following primers: 5′-TGTGAATGTCTTCACACAGGCGCCAGTTTGCACTTCCCAC-3′, 5′-GGTACGGCCAAATCAAGCTGGCACTCTGATAGCCAG-3′, and 5′-CAGTAGCCATCATGCCCGCTGGAGCTCATATAGTGTCTGCCTC-3′. The yeast gene encoding Lis1 (*PAC1*) previously cloned into a Topo 2.1 vector using the TOPO TA Cloning Kit (Thermo Fisher), was mutated using a site-directed mutagenesis kit (Agilent) with the primers: 5′-GGATGTTTTATTTACCAATTATACGGCCTCCAGCAAGAAGAACTATTTGGTG-3′ and

5′-cACCAAATAGTTCTTCTTGCTGGAGGCCGTATAATTGGTAAATAAAACATCC-3′ to insert the N213A substitution. *PAC1* or *pac11-N213A* were mutated using the primers 5′-TTTGGGACTTCCACAATGGTGACTCGTTGAAAACATTTCAGCC-3′ and 5′-GGCTGAAATGTTTTCAACGAGTCACCATTGTGGAAGTCCCAAA-3′ to insert the W288D substitution. *DYN1(3396–3921aa)* was cloned into a pBlueHeron vector through Gibson assembly and was mutagenized with the primers 5′-GATTAGAAAATGCAATTAGAGCCGGAAGTGTAGTTATAATTC-3′ and 5′-GAATTATAACTACACTTCCGGCTCTAATTGCATTTTCTAATC-3′ to introduce the F3446A substitution. *dyn1-F3446A* was mutated using a site-directed mutagenesis kit (Agilent) with the primers 5′-GAGGAGACAAAGGCGGCAGAAGCACATGAGAAATTCAAAATGT-3′ and 5′-ACATTTTGAATTTCTCATGTGCTTCTGCCGCCTTTGTCTCCTC-3′ to introduce the E3867A substitution.

Yeast strains

The *S. cerevisiae* strains used in this study are listed in Supplementary Table 2.1. The endogenous genomic copy of *PAC1* (encoding Lis1) was deleted using PCR-based methods as previously described[39]. In brief, *K. lactis URA3* with homology arms complementary to regions upstream and downstream of the *PAC1* or *DYN1* genomic locus was generated using PCR. This fragment was transformed into a strain with the preferred genetic background using the lithium acetate method[40] and screened by colony PCR. Point mutants were generated using QuikChange site-directed mutagenesis (Agilent) and verified by DNA sequencing. Mutated fragments were re-inserted into the kl*URA3* strains to reintroduce the mutated *PAC1* or *DYN1* gene. Positive clones lacking URA3 (kl*URA3*-) were selected in the presence of 5-fluoroorotic acid, screened by colony PCR, and verified by DNA sequencing.

Nuclear segregation assay

Single colonies were picked and grown at 30 °C. Log-phase *S. cerevisiae* cells growing at 30 °C were transferred to 16 °C for 16 h. Cells were fixed with 75% ethanol for 1 h, sonicated for 5 s at 40% amplitude, and mounted in medium containing DAPI. Imaging was performed using an Apo TIRF 100 ×1.49 NA objective (Nikon, Plano Apo) on a Nikon Ti2 microscope with a Yokogawa-X1 spinning disk confocal system, MLC400B laser engine (Agilent), Prime 95B back-thinned sCMOS camera (Teledyne Photometrics), and a piezo Z-stage (Mad City Labs). The samples were blinded during imaging. The percentage of aberrant binucleate cells was calculated as the number of binucleate cells divided by the sum of wild-type and binucleate cells. Eight to 12 biological replicates from independent colonies were done for Figure 2.4c, and three were done for Figure 2.4d,i. At least 200 cells were counted for each biological replicate per condition.

Live-cell imaging

Single colonies were picked and grown at 30 °C. Log-phase live *S. cerevisiae* cells were mounted on a thin agarose pad made from SC medium pressed between two glass slides. Live cells genetically modified to express fluorescently labeled DYN1-3XGFP, CFP-TUB1, and SPC110-tdTomato were imaged using a Yokogawa W1 confocal scanhead mounted to a Nikon Ti2 microscope with an Apo TIRF 100 ×1.49 NA objective (Nikon, Plano Apo). The microscope was run with NIS Elements using the 488 nm 515 nm and 561 nm lines of a six-line (405 nm, 445 nm, 488 nm, 515 nm, 561 nm, and 640 nm) LUN-F-XL laser engine and Prime95B cameras (Photometrics). The DYN1-3×GFP foci localizing to the spindle pole body (SPB), microtubule plus end, and cell cortex were outlined as regions of interest in Fiji[41], recorded, and analyzed for three replicates of at least 120 cells for each sample.

S. cerevisiae immunoprecipitations and western blots

Log-phase *S. cerevisiae* cells grown at 30 °C were pelleted at 4,000*g*, resuspended in water, and flash frozen in liquid nitrogen. Liquid-nitrogen-frozen yeast cell pellets were lysed by grinding in a chilled coffee grinder, resuspended in dynein-lysis buffer (30 mM HEPES pH 7.4, 50 mM potassium acetate, 2 mM magnesium acetate, 1 mM EGTA, 10% glycerol, 1 mM DTT) supplemented with 1 mM Pefabloc, 0.2% Triton X-100, cOmplete EDTA-free protease inhibitor cocktail tablet (Roche), and 1 mM Pepstatin A (Cayman Chemical Company), and spun at 50,000*g* for 1 h. The protein concentration of the clarified supernatants was quantified using a Bradford Protein Assay (Bio-Rad), and equal amounts of clarified lysates were incubated with anti-FLAG M2 Affinity Gel (Sigma) overnight at 4 °C. Beads were washed with dynein-lysis buffer, boiled in SDS sample buffer, and loaded onto a NuPAGE Bis-Tris gel (Invitrogen). Gels were transferred to a PVDF membrane that was blocked with PBS-T (PBS1X and 0.1% Tween-20) containing 5% milk and 1% BSA for 1 h at room temperature and blotted with a rabbit anti-FLAG antibody (1:3,000; Proteintech 20543-1-AP) overnight at 4 °C. Membranes were then incubated with a goat-anti-rabbit IRDye 6800RD secondary antibody (LI-COR) and were scanned in a ChemiDoc Imaging system (Bio-Rad).

Protein expression and purification

S. cerevisiae dynein

Protein purification steps were done at 4 °C unless otherwise indicated. *S. cerevisiae* dynein constructs were purified from *S. cerevisiae* using a ZZ tag as previously described[42]. Briefly, liquid-nitrogen-frozen yeast cell pellets were lysed by grinding in a chilled coffee grinder and resuspended in dynein-lysis buffer supplemented with 0.1 mM Mg-ATP, 0.5 mM Pefabloc, 0.05% Triton X-100, and cOmplete EDTA-free protease inhibitor cocktail

tablet (Roche). The lysate was clarified by centrifuging at 264,900*g* for 1 h. The clarified supernatant was incubated with IgG Sepharose beads (GE Healthcare Life Sciences) for 1 h. The beads were transferred to a gravity flow column, washed with dynein-lysis buffer supplemented with 250 mM potassium chloride, 0.1 mM Mg-ATP, 0.5 mM Pefabloc, and 0.1% Triton X-100, and with TEV buffer (10 mM Tris-HCl pH 8.0, 150 mM potassium chloride, 10% glycerol, 1 mM DTT, and 0.1 mM Mg-ATP). Dynein was cleaved from IgG beads via incubation with 0.15 mg mL^{-1} TEV protease (purified in the Reck-Peterson lab) overnight at 4 °C. Cleaved dynein was concentrated using 100 kDa MWCO concentrator (EMD Millipore), filtered by centrifugation with Ultrafree-MC VV filter (EMD Millipore) in a tabletop centrifuge, and flash frozen in liquid nitrogen.

S. cerevisiae Lis1

S. cerevisiae Lis1 was purified from *S. cerevisiae* using 8×His and ZZ tags as previously described[43]. In brief, liquid-nitrogen-frozen pellets were ground in a pre-chilled coffee grinder, resuspended in buffer A (50 mM potassium phosphate pH 8.0, 150 mM potassium acetate, 150 mM sodium chloride, 2 mM magnesium acetate, 5 mM β-mercaptoethanol, 10% glycerol, 0.2% Triton X-100, 0.5 mM Pefabloc) supplemented with 10 mM imidazole (pH 8.0) and cOmplete EDTA-free protease inhibitor cocktail tablet, and spun at 118,300*g* for 1 h. The clarified supernatant was incubated with Ni-NTA agarose (QIAGEN) for 1 h. The Ni beads were transferred to a gravity column, washed with buffer A + 20 mM imidazole (pH 8.0), and eluted with buffer A + 250 mM imidazole (pH 8.0). The eluted protein was incubated with IgG Sepharose beads for 1 h. IgG beads were transferred to a gravity flow column and washed with buffer A + 20 mM imidazole (pH 8.0) and with modified TEV buffer (50 mM Tris-HCl pH 8.0, 150 mM potassium acetate, 2 mM magnesium acetate, 1 mM EGTA, 10% glycerol, 1 mM DTT).

Lis1 was cleaved from the IgG beads by the addition of 0.15 mg mL^{-1} TEV protease (purified in the Reck-Peterson lab) for 1 h at 16 °C. Cleaved proteins were filtered by centrifuging with Ultrafree-MC VV filter (EMD Millipore) in a tabletop centrifuge and flash frozen in liquid nitrogen.

Human dynein

Full-length human SNAP-tagged dynein was expressed in Sf9 cells, as described previously[23,44]. Briefly, frozen Sf9 cell pellets from 2× 600 mL culture were resuspended in 80 mL of dynein-lysis buffer with 0.1 mM Mg-ATP, 0.5 mM Pefabloc, 0.05% Triton X-100, and cOmplete EDTA-free protease inhibitor cocktail tablet (Roche) and lysed using a Dounce homogenizer (10 strokes with a loose plunger and 15 strokes with a tight plunger). The lysate was clarified by centrifuging at 183,960*g* for 88 min in a Type 70 Ti rotor (Beckman). The clarified supernatant was incubated with 4 mL of IgG Sepharose 6 Fast Flow beads (GE Healthcare Life Sciences) for 3–4 h on a roller. The beads were transferred to a gravity flow column, washed with 200 mL of dynein-lysis buffer and 300 mL of TEV buffer (50 mM Tris-HCl pH 8.0, 250 mM potassium acetate, 2 mM magnesium acetate, 1 mM EGTA, 1 mM DTT, 0.1 mM Mg-ATP, 10% (vol/vol) glycerol). For fluorescent labeling of the C-terminal SNAPf tag, dynein-coated beads were labeled with 5 µM SNAP-Cell-TMR (New England Biolabs) in the column for 10 min at room temperature, and unbound dye was removed with a 300 mL wash with TEV buffer at 4 °C. The beads were then resuspended and incubated in 15 mL of TEV buffer supplemented with 0.5 mM Pefabloc and 0.2 mg mL^{-1} TEV protease (purified in the Reck-Peterson lab) overnight on a roller. The supernatant containing cleaved protein was concentrated using a 100 kDa MWCO concentrator (EMD Millipore) to 500 µL and purified via size-exclusion chromatography on a TSKgel G4000SWXL column (TOSOH Bioscience) with

GF150 buffer (25 mM HEPES pH 7.4, 150 mM potassium chloride, 1 mM magnesium chloride, 5 mM DTT, 0.1 mM Mg-ATP) at 1 mL min^{-1}. The peak fractions were collected, buffer-exchanged into a GF150 buffer supplemented with 10% glycerol, concentrated to 0.1–0.5 mg mL^{-1} using a 100 kDa MWCO concentrator (EMD Millipore). Purity was evaluated on SDS–PAGE gels, and protein aliquots were snap frozen in liquid N_2 and stored at –80 °C.

Human dynactin

Dynactin (p62-HaloTag-3×FLAG) was purified from a stable 293T cell line, as previously described[23,38,44]. Briefly, frozen pellets from 293T cells (160 × 15-cm plates) were resuspended in dynein-lysis buffer supplemented with 0.1 mM Mg-ATP, 0.5 mM Pefabloc, 0.05% Triton, and cOmplete EDTA-free protease inhibitor cocktail tablet (Roche), and gently mixed at 4 °C for 15 min. The lysed cells were then centrifuged at 500,000*g* in a Ti70 rotor (Beckman) at 4 °C for 30 min. The clarified lysate was retrieved and added to 3 mL packed anti-FLAG M2 agarose resin (Sigma) and incubated with gentle mixing at 4 °C for 16 h. After incubation, the lysate-resin mixture was centrifuged at 1,000*g* for 2 min at 4 °C to pellet the resin, and the supernatant was decanted. The resin was transferred to a column at 4 °C, and the column was washed with 100 mL low-salt wash buffer (30 mM HEPES, pH 7.4; 50 mM potassium acetate; 2 mM magnesium acetate; 1 mM EGTA, pH 7.5; 10% glycerol; 1 mM DTT; 0.5 mM ATP; 0.5 mM Pefabloc; 0.02% Triton X-100), 100 mL high-salt wash buffer (30 mM HEPES, pH 7.4; 250 mM potassium acetate; 2 mM magnesium acetate; 1 mM EGTA, pH 7.5; 10% glycerol; 1 mM DTT; 0.5 mM ATP; 0.5 mM Pefabloc; 0.02% Triton X-100), and finally with 50 mL of low-salt wash buffer. The resin was resuspended in 800 µL of low-salt wash buffer containing 2 mg mL^{-1} 3×-FLAG peptide (ApexBio) and incubated for 30 min at 4 °C. The mixture was retrieved and centrifuged through a small filter column to remove the resin. The

eluate was then loaded onto a Mono Q 5/50 GL 1 mL column on an AKTA FPLC (GE Healthcare). The column was washed with 5 mL of Buffer A (50 mM Tris-HCl, pH 8.0; 2 mM magnesium acetate; 1 mM EGTA; 1 mM DTT) and then subjected to a 26 mL linear gradient from 35–100% Buffer B mixed with Buffer A (Buffer B = 50 mM Tris-HCl, pH 8.0; 1 M potassium acetate; 2 mM magnesium acetate; 1 mM EGTA; 1 mM DTT), followed by an additional 5 mL 100% Buffer B. Fractions containing pure dynactin (~75–80% Buffer B) were pooled and buffer-exchanged through iterative rounds of dilution and concentration on a 100 kDa MWCO centrifugal filter (Amicon Ultra, Millipore) using GF150 buffer with 10% glycerol. Purity was evaluated on SDS–PAGE gels and protein aliquots were snap frozen in liquid N_2 and stored at –80 °C.

Human LIS1

LIS1 constructs were purified from frozen SF9 cell pellets from a 600 mL culture, as described previously[45]. Lysis and clarification steps were similar to full-length dynein purification except lysis was performed in LIS1-lysis buffer (30 mM HEPES pH 7.4, 50 mM potassium acetate, 2 mM magnesium acetate, 1 mM EGTA, 300 mM potassium chloride, 1 mM DTT, 0.5 mM Pefabloc, 10% (vol/vol) glycerol) supplemented with cOmplete EDTA-free protease inhibitor cocktail tablet (Roche) per 50 mL was used. The clarified supernatant was incubated with 0.5 mL of IgG Sepharose 6 Fast Flow beads (GE Healthcare Life Sciences) for 2-3 hours on a roller. The beads were transferred to a gravity flow column, washed with 20 mL of LIS1-lysis buffer, 100 mL of modified TEV buffer (10 mM Tris-HCl pH 8.0, 2 mM magnesium acetate, 150 mM potassium acetate, 1 mM EGTA, 1 mM DTT, 10% (vol/vol) glycerol) supplemented with 100 mM potassium acetate, and 50 mL of modified TEV buffer. LIS1 was cleaved from IgG beads via incubation with 0.2 mg mL^{-1} TEV protease overnight on a roller.

The cleaved LIS1 was filtered by centrifuging with an Ultrafree-MC VV filter (EMD Millipore) in a tabletop centrifuge. Purity was evaluated on SDS–PAGE gels, and protein aliquots were snap frozen in liquid N_2 and stored at –80 °C.

Human BICD2

BICD2 construct containing N-terminal sfGFP was expressed and purified as previously described[38]. In brief, BL-21[DE3] cells (New England Biolabs) were grown at optical density at 600 nm of 0.4–0.6, and protein expression was induced with 0.1 mM IPTG for 16 h at 18 °C. Frozen cell pellet from a 2 L culture was resuspended in 60 mL of lysis buffer (30 mM HEPES pH7.4, 50 mM potassium acetate, 2 mM magnesium acetate, 1 mM EGTA, 1 mM DTT and 0.5 mM Pefabloc, 10% (vol/vol) glycerol) supplemented with cOmplete EDTA-free protease inhibitor cocktail tablet (Roche) per 50 mL and 1 mg mL^{-1} lysozyme. The resuspension was incubated on ice for 30 min and lysed by sonication. The lysate was clarified by centrifuging at 500,000*g* for 30 min in Type 70 Ti rotor (Beckman). The clarified supernatant was incubated with 2 mL of IgG Sepharose 6 Fast Flow beads (GE Healthcare Life Sciences) for 2 h on a roller. The beads were transferred into a gravity flow column, washed with 100 mL of activating-adapter-lysis buffer supplemented with 150 mM potassium acetate and 50 mL of cleavage buffer (50 mM Tris-HCl pH 8.0, 150 mM potassium acetate, 2 mM magnesium acetate, 1 mM EGTA, 1 mM DTT, 0.5 mM Pefabloc, and 10% (vol/vol) glycerol). The beads were then resuspended and incubated in 15 mL of cleavage buffer supplemented with 0.2 mg mL^{-1}TEV protease overnight on a roller. The supernatant containing cleaved protein was concentrated using a 50 kDa MWCO concentrator (EMD Millipore) to 1 mL, filtered by centrifuging with Ultrafree-MC VV filter (EMD Millipore) in a tabletop centrifuge, diluted to 2 mL in buffer A (30 mM HEPES pH 7.4, 50 mM potassium acetate, 2 mM magnesium acetate, 1 mM EGTA, 10%

(vol/vol) glycerol, and 1 mM DTT), and injected into a MonoQ 5/50 GL column (GE Healthcare and Life Sciences) at 1 mL min^{-1}. The column was prewashed with 10 CV of buffer A, 10 CV of buffer B (30 mM HEPES pH7.4, 1 M potassium acetate, 2 mM magnesium acetate, 1 mM EGTA, 10% (vol/vol) glycerol, and 1 mM DTT) and again with 10 CV of buffer A at 1 mL min^{-1}. For elution, a linear gradient was run over 26 CV from 0–100% buffer B. The peak fractions containing sfGFP-BICD2s were collected and concentrated using a 50 kDa MWCO concentrator (EMD Millipore) to 0.2 mL. Protein was then diluted to 0.5 mL in GF150 buffer and further purified using size-exclusion chromatography on a Superose 6 Increase 10/300GL column (GE Healthcare and Life Sciences) with GF150 buffer at 0.5 mL min^{-1}. The peak fractions were collected, buffer-exchanged into a GF150 buffer supplemented with 10% glycerol, concentrated to 0.2–1 mg mL^{-1} using a 50 kDa MWCO concentrator (EMD Millipore), and flash frozen in liquid nitrogen.

TIRF microscopy

Imaging was performed with an inverted microscope (Nikon, Ti-E Eclipse) equipped with a 100×1.49 N.A. oil immersion objective (Nikon, Plano Apo). The *xy* position of the stage was controlled by ProScan linear motor stage controller (Prior). The microscope was equipped with an MLC400B laser launch (Agilent) equipped with 405 nm (30 mW), 488 nm (90 mW), 561 nm (90 mW), and 640 nm (170 mW) laser lines. The excitation and emission paths were filtered using appropriate single bandpass filter cubes (Chroma). The emitted signals were detected with an electron multiplying CCD camera (Andor Technology, iXon Ultra 888). Illumination and image acquisition was controlled by NIS Elements Advanced Research software (Nikon).

Single-molecule motility assays

Single-molecule motility assays were performed in flow chambers using the TIRF microscopy setup described above. To reduce non-specific binding biotinylated and PEGylated coverslips (Microsurfaces) with microtubules polymerized from tubulin prepared from bovine brain, as previously described[38]. Microtubules contained ~10% biotin-tubulin to allow for attachment to streptavidin-coated coverslip and ~10% Alexa Fluor 488 (Thermo Fisher Scientific) tubulin for visualization. Imaging was done in dynein-lysis buffer supplemented with 20 μM taxol, 1 mg mL^{-1} casein, 5 mM Mg-ATP, 71.5 mM β-mercaptoethanol, and an oxygen scavenger system containing 0.4% glucose, 45 μg mL^{-1} glucose catalase (Sigma-Aldrich), and 1.15 mg mL^{-1}glucose oxidase (Sigma-Aldrich). Images were recorded every 0.3 s for 3 min. Movies showing significant drift were not analyzed.

All movies were collected by measuring TMR–dynein signal with the following protein concentrations: 83.5 pM TMR-dynein, 665 pM unlabeled dynactin, 5 nM BICD2, and 300 nM LIS1. For conditions missing LIS1, the corresponding matching buffer was used. The dynein, dynactin, and BICD2 complexes were incubated on ice for 10 min prior to LIS1 or buffer addition. Each protein mixture was then incubated on ice for an additional 10 min prior to TIRF imaging.

TIRF motility data analysis

The velocity of moving particles was calculated from kymographs generated in Fiji as described previously[18]. Velocities were calculated only from molecules that moved processively (continuously moving along a microtubule track) for more than five frames. Non-motile or diffusive events were not considered in velocity calculations. Processive events were defined as events that move unidirectionally and do not exhibit directional changes greater than 600 nm.

Diffusive events were defined as events that exhibit at least one bidirectional movement greater than 600 nm in each direction. Static events were defined as events that do not exhibit movement (less than 600 nm in each direction). Single-molecule movements that change apparent behavior (for example, shift from non-motile to processive) were considered multi-velocity events and counted as multiple events. Processive runs were calculated by counting the number of processive events for each microtubule in individual movies and dividing this number by the microtubule length. The percentage of diffusive events was calculated as diffusive events / (diffusive + stationary + processive) × 100.

Statistical analysis

Brightness and contrast were adjusted in Fiji for all images, videos, and kymographs. All statistical tests were generated using GraphPad Prism 9. The exact value of *n*, evaluation of statistical significance, *P* values, and specific statistical analysis are described in the corresponding figures and figure legends. All TIRF experiments were analyzed from four independent replicates, and individual analysis of each replicate showed similar results. For velocity analysis, frequency distributions were first calculated for each replicate, and data were fit to a Gaussian distribution to calculate mean values. Nuclear segregation assays in Figure 2.4c included 8–12 biological replicates from independent cultures per condition. Statistics were generated for all biological replicates (8–12) within each condition. Nuclear segregation assay analysis for Figure 2.4c,i included three biological replicates from independent cultures for each condition, and statistics were generated for the three biological replicates within each condition using a one-way ANOVA with Tukey's multiple comparisons test of each mean. Live-cell imaging experiments to assess dynein localization include three biological replicates from three independent cultures. Each replicate included >40 mid-stage mitotic cells with an *n* of

at least 120 cells per condition. Each cell was assessed for the number of dynein foci at the cortex, spindle pole body or microtubule tips. Statistical analysis was performed on the means of each biological replicate using a one-way ANOVA with Tukey's multiple comparison test.

Data availability

Cryo-EM maps and molecular models have been deposited in the EM Data Bank and Protein Data Bank, respectively. Accession codes are listed here and in Table 2.1. Dynein^{E2488Q} bound to Lis1 in Chi conformation: EMD-27810 and PDB 8DZZ; dynein^{E2488Q} bound to Lis1 in Chi conformation, symmetry expanded: EMD-27811 and PDB 8E00.

2.4 Supplementary Figures

Supplementary Figure 2.1 Cryo-EM data processing workflow.

a, Processing workflow for Chi. Particles belonging to teal maps were carried into the next round of processing. **b**, Cryo-EM map of Chi (dynein^{E2488Q}-Lis1)$_2$ colored by local resolution. **c**, Fourier shell correlation (FSC) plot for Chi. **d**, Symmetry expansion followed by local refinement map of dynein^{E2488Q}-(Lis1)$_2$. **e**, Local refinement of symmetry expanded dynein^{E2488Q}-(Lis1)$_2$ colored by local resolution. **f**, FSC plot for local refinement map.

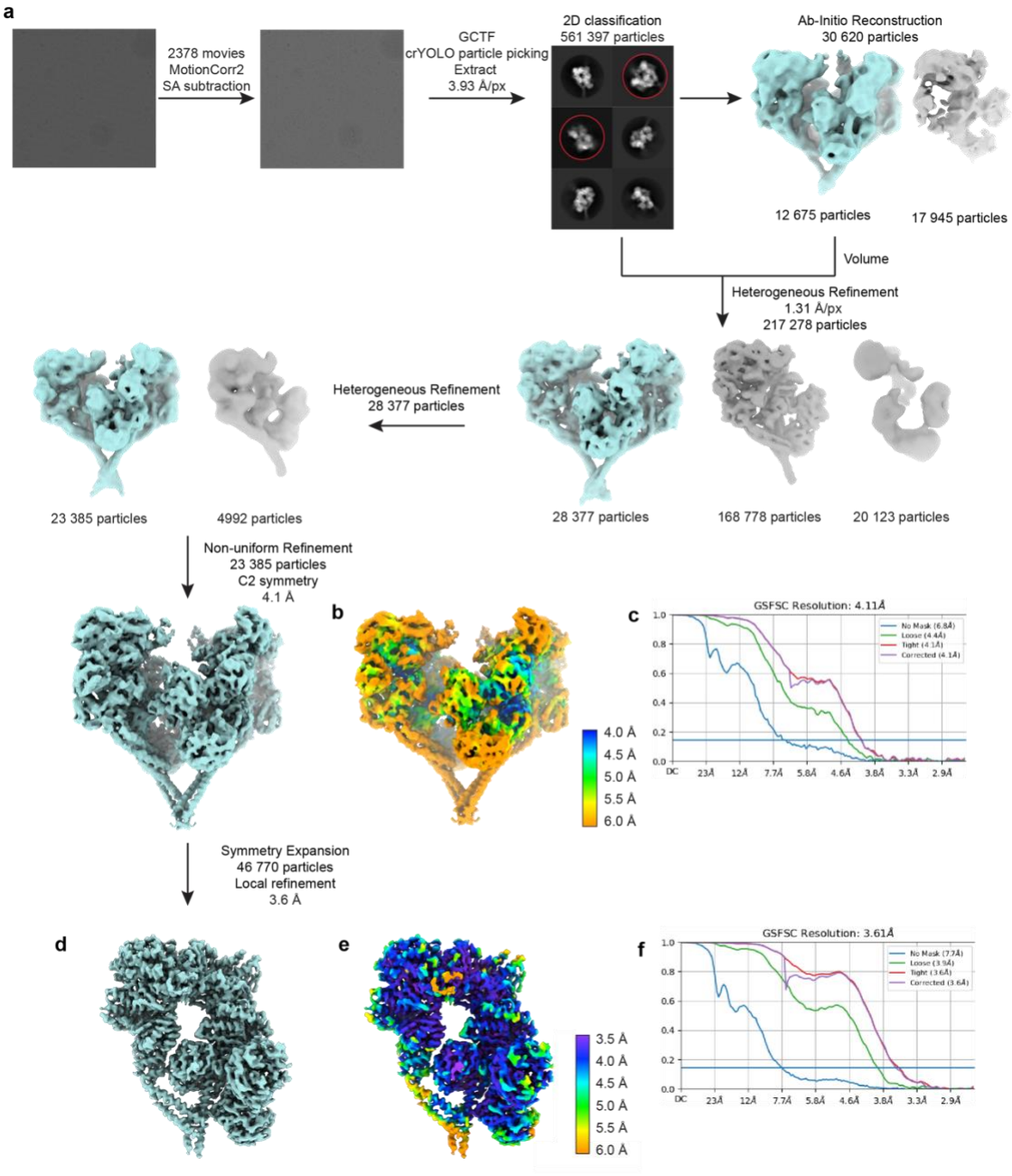
a
2378 movies
MotionCorr2
SA subtraction
GCTF
crYOLO particle picking
Extract
3.93 Å/px
2D classification
561 397 particles
Ab-Initio Reconstruction
30 620 particles
12 675 particles
17 945 particles
Volume
Heterogeneous Refinement
1.31 Å/px
217 278 particles
Heterogeneous Refinement
28 377 particles
23 385 particles
4992 particles
28 377 particles
168 778 particles
20 123 particles
Non-uniform Refinement
23 385 particles
C2 symmetry
4.1 Å
b
4.0 Å
4.5 Å
5.0 Å
5.5 Å
6.0 Å
c
GSFSC Resolution: 4.11Å
Symmetry Expansion
46 770 particles
Local refinement
3.6 Å
d
e
3.5 Å
4.0 Å
4.5 Å
5.0 Å
5.5 Å
6.0 Å
f
GSFSC Resolution: 3.61Å

Supplementary Figure 2.2 The wild-type yeast dynein motor domain can form Chi in the presence of ATP. a, Class average from a data set of wild-type yeast dynein motor domain incubated in the presence of Lis1 and ATP. **b**, Our model of Chi, rendered as a surface at 10 Å resolution, shown in the same orientation as the class average in (a), which corresponds to Chi being viewed from the stalks and towards the motor domains. **c**, The model in (b) is rotated to show a more canonical view of Chi. Note that Lis1-stalk$_2$ appears to have partial density in the class average.

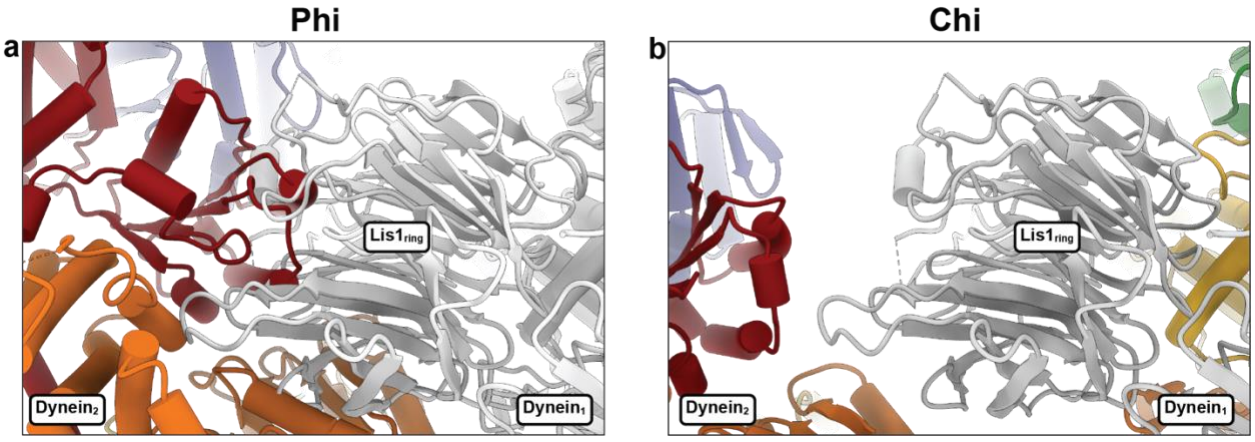

Supplementary Figure 2.3 Binding of Lis1 to dynein is sterically incompatible with Phi.

a, Phi dynein (PDB 5NUG) was aligned to dynein in Chi, which is shown in gray in this panel. Phi's dynein$_2$, shown in color, clashes with the Lis1 bound at site$_{ring}$ in Chi's dynein$_1$. **b**, Close up of our model of Chi equivalent to the view in (a), showing Lis1 bound at site$_{ring}$ on dynein$_1$. Part of dynein$_2$, with which the Lis1 at site$_{ring}$ interacts in Chi, is also shown.

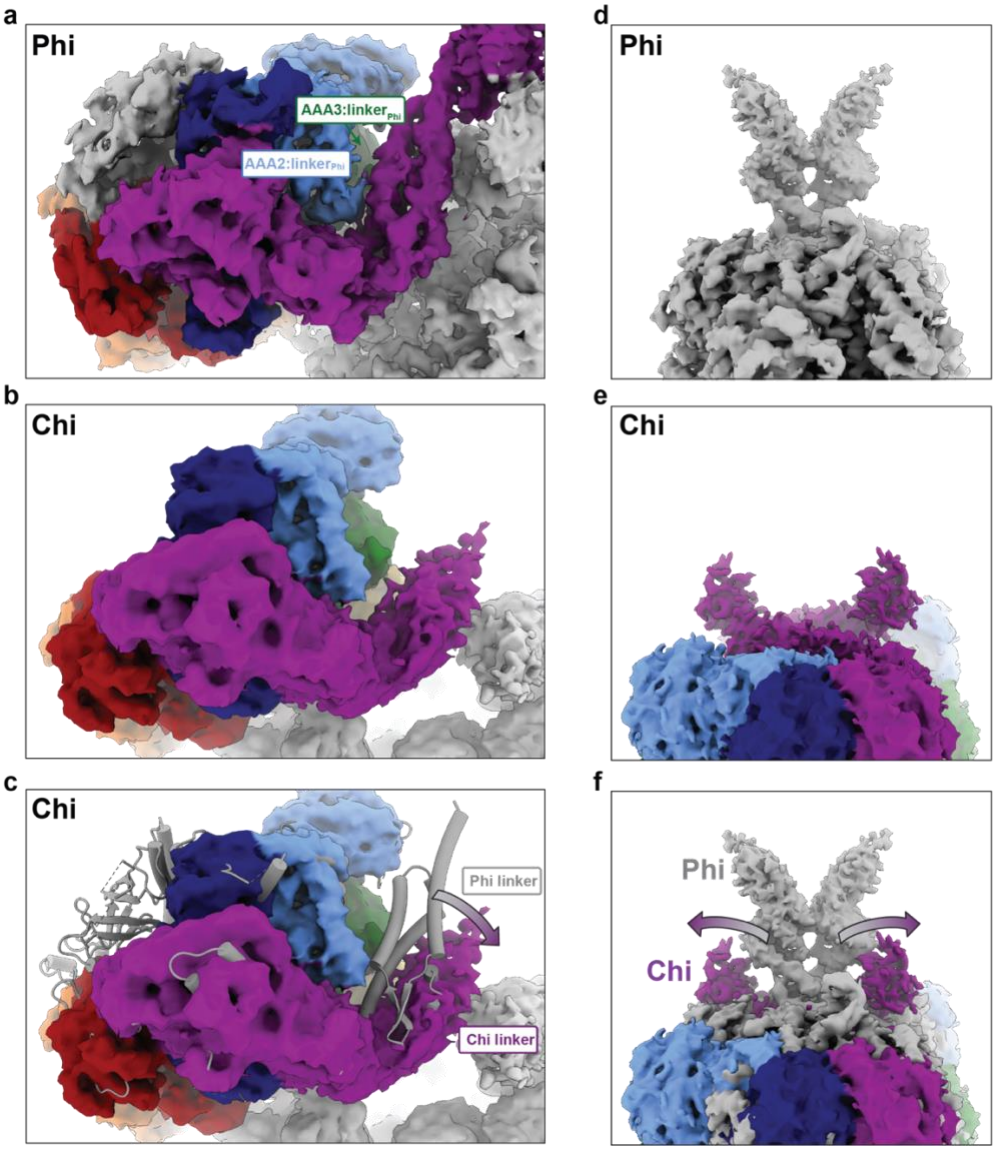

Supplementary Figure 2.4 The conformation of the linker is different in Chi and Phi.

a, The linker docks onto AAA2 and AAA3 in Phi. **b**, In contrast, the linker is disengaged from the AAA ring in Chi. **c**, Overlay of Phi (a) and Chi (b) highlights the different positions of the linker. **d**, **e**, The N-termini of the linker adopt different paths in Phi (d) and Chi (e). **f**, Overlay of Phi (d) and Chi (e) shows how the linkers are pulled apart in Chi.

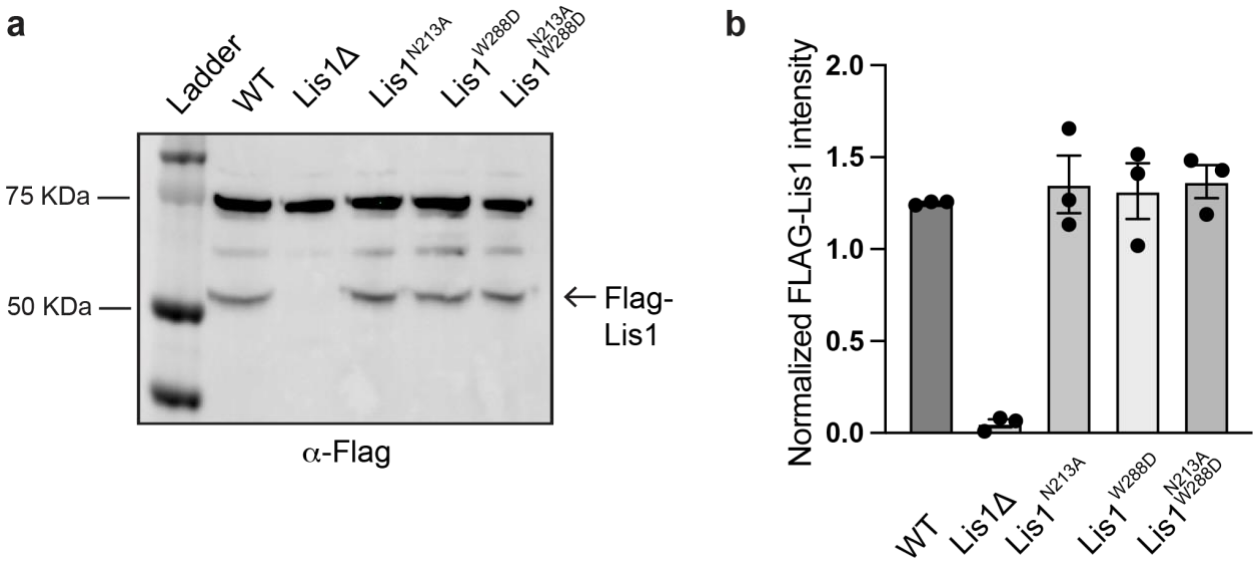

Supplementary Figure 2.5 Western blot analysis of Lis1 mutant expression.

a, Cell lysates from wild type (WT), Lis1Δ or mutant Lis1 ($Lis1^{N213A}$, $Lis1^{W288D}$ and $Lis1^{N213A, W88D}$) *S. cerevisiae* strains containing Flag-tagged Lis1 (Pac1) were immunoprecipitated using anti-Flag agarose beads and immunoblotted for the FLAG peptide (α-FLAG). **b**, Quantitative analysis (mean ± s.e.m.) of Lis1 expression (α-FLAG band) normalized against the non-specific band observed at ~75 KDa for three independent immunoprecipitations. Statistics were generated using a One-way ANOVA with Tukey multiple comparisons of each mean test. **** WT and ΔLis1, ΔLis1 and $Lis1^{N213A}$, ΔLis1 and $Lis1^{W288D}$, ΔLis1 and $Lis1^{N213A, W288D}$ $p < 0.0001$. Differences not noted are not statistically significant. Source data are provided with the manuscript.

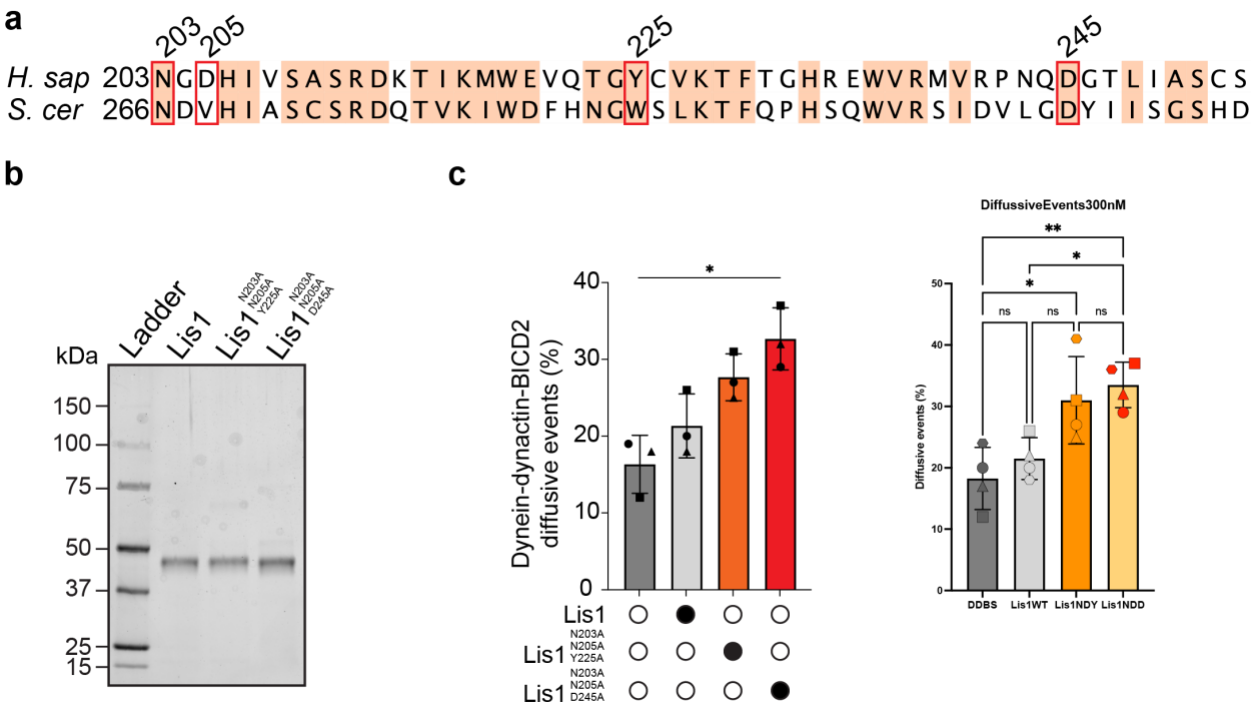

Supplementary Figure 2.6 Chi mutations in human LIS1.

a, Sequence conservation between *S. cerevisiae* (*S. cer*) and human (*H. sap*) Lis1 in the vicinity of the dynein binding site in the Chi structure. Residues with 70% conservation or higher are shaded in light red. The residues mutated in this study: N203, D205, Y225, and D245 are highlighted by red boxes. **b**, Sodium dodecyl sulfate–polyacrylamide gel electrophoresis (SDS–PAGE) of the human LIS1 constructs used for motility assays. **c**, Comparison of percent diffusive events (mean ± SEM) from single-molecule TMR-dynein-dynactin-BICD2 assays performed in the absence (white circle) or presence (black circle) of different LIS1 constructs. The data points are represented as triangles, circles, and squares, corresponding to the mean diffusive events measured within each technical replicate. Four replicates per condition were collected and the number of data points (n) per each replicate is listed (no LIS1, n = 14/20/20/8; LIS1, n = 7/16/7/5; LIS1$^{N203A, D205A, Y225A}$, n = 15/7/16/9; LIS1$^{N203A, D205A, D245A}$, n = 17/9/17/9). ** no LIS1 and LIS1$^{N203A, D205A, D245A}$ p = 0.0051, * no LIS1 and LIS1$^{N203A, D205A, Y225A}$ p = 0.017, * LIS1 and LIS1$^{N203A, D205A, D245A}$ ** p = 0.025 ns, not statistically significant, One-Way ANOVA with Tukey multiple comparisons of each mean. Source data are provided with the manuscript.

2.5 Tables

Table 2.1 Cryo-EM data collection, refinement and validation statistics.

	Dynein^{E2488Q} bound to Lis1 in Chi conformation. EMD-27810 PDB 8DZZ	Dynein^{E2488Q} bound to Lis1 in Chi conformation, symmetry expansion EMD-27811 PDB 8E00	Dynein bound to Lis1 in the presence of ATP
Data collection and processing			
Magnification	38 000	38 000	36 000
Voltage (kV)	300	300	200
Electron exposure (e–/Å^2)	58.3	58.3	51.0
Defocus range (μm)	2 – 2.7	2 – 2.7	0.8 – 2.4
Pixel size (Å)	1.31	1.31	1.16
Symmetry imposed	C2	C1	
Initial particle images (no.)	561 397	561 397	
Final particle images (no.)	23 385	46 770	
Map resolution (Å)	4.1	3.6	
FSC threshold	0.143	0.143	
Map resolution range (Å)	4.0 – 6.0	3.5 – 6.0	
Refinement			
Initial model used (PDB code)	8E00	7MGM	
Model resolution (Å)	4.4	3.9	
FSC threshold	0.5	0.5	
Map sharpening *B* factor (Å^2)	106.5	90.5	
Model composition			
Non-hydrogen atoms	49 596	24 794	
Protein residues	6 110	3 055	
Ligands	8	4	
B factors (Å^2)			
Protein	154.6	94.0	
Ligand	132.4	77.6	
R.m.s. deviations			
Bond lengths (Å)	0.005	0.005	
Bond angles (°)	1.087	1.124	
Validation			
MolProbity score	1.11	0.98	
Clashscore	3.00	2.10	
Poor rotamers (%)	0.25	0.47	
Ramachandran plot			
Favored (%)	98.39	98.21	
Allowed (%)	1.57	1.76	
Disallowed (%)	0.03	0.03	

2.6 Supplementary Tables

Supplementary Table 2.1 S. cerevisiae strains used in this study. DHA and SNAP refer to the HaloTag (Promega) and SNAP-tag (NEB), respectively. TEV indicates a Tev protease cleavage site. PGAL1 denotes the galactose promoter, which was used for inducing strong expression of Lis1 and dynein motor domain constructs. Amino acid spacers are indicated by g (glycine) and gs (glycine-serine).

Strain	Genotype	Source
RPY1	W303a (*MATa; his3-11,15; ura3-1; leu2-3,112; ade2-1; trp1-1*)	(Eshel et al., 1993)
RPY816	W303a; *pep4Δ::HIS5; prb1Δ; GAL1-8HIS-ZZ-Tev-PAC1; dyn1Δ::CgLEU2; ndl1Δ::HPH*	(Huang et al., 2012)
RPY1654	W303a; *pep4Δ::HIS5; prb1Δ; PAC11-13xMYC-TRP1; PGAL1-ZZTev-DYN1(331kDa) E2488Q; pac1Δ:: HygroR*	(DeSantis et al., 2017)
RPY1385	MATa *lys2-801 leu2-Δ1 his3-Δ200 trp1-Δ63 DYN1-3XGFP::TRP1, ura3-52::CFP-TUB1::URA3, SPC110-tdTomato::SpHIS5, ura3Δ::KanMX*	(DeSantis et al., 2017)
RPY1717	*MATa lys2-801; leu2- Δ 1; his3-Δ200; trp1-Δ63; DYN1-3XGFP::TRP1; ura3-52::CFP-TUB1::URA3; SPC110-tdTomato::SpHIS5; ura3Δ::KanMX; pac1Δ::KlURA3*	(DeSantis et al., 2017)
RPY1811	*MATa lys2-801; leu2- Δ 1; his3-Δ200; trp1-Δ63; ura3-52::CFP-TUB1::URA3; SPC110-tdTomato::SpHIS5; ura3Δ::KanMX; dyn1Δ::KlURA3*	(Gillies et al., 2022)
RPY1795	*MATa lys2-801; leu2-Δ1; his3-Δ200; trp1-Δ63; DYN1-3XGFP::TRP1; ura3-52::CFP-TUB1::URA3; SPC110-tdTomato::SpHIS5; ura3Δ::KanMX; Flag-PAC1*	(Gillies et al., 2022)
RPY1814	*MATa lys2-801; leu2-Δ1; his3-Δ200; trp1-Δ63; DYN1-3XGFP::TRP1; ura3-52::CFP-TUB1::URA3; SPC110-tdTomato::SpHIS5; ura3Δ::KanMX; Flag-pac1(W288D)*	This work
RPY1831	*MATa lys2-801; leu2-Δ1; his3-Δ200; trp1-Δ63;DYN1-3XGFP::TRP1; ura3-52::CFP-TUB1::URA3; SPC110-tdTomato::SpHIS5; ura3Δ::KanMX; Flag-pac1(N213A)*	This work
RPY1834	*MATa lys2-801; leu2-Δ1; his3-Δ200; trp1-Δ63;DYN1-3XGFP::TRP1; ura3-52::CFP-TUB1::URA3; SPC110-tdTomato::SpHIS5; ura3Δ::KanMX; Flag-pac1(N213A-W288D)*	This work
RPY1854	*MATa lys2-801; leu2- Δ 1; his3-Δ200; trp1-Δ63; DYN1(D2868K)-3XGFP::TRP1; ura3-52::CFP-TUB1::URA3; SPC110-tdTomato::SpHIS5; ura3Δ::KanMX; pac1Δ::KlURA3*	This work
RPY1861	*MATa lys2-801; leu2-Δ1; his3-Δ200; trp1-Δ63;DYN1 (D2868K)-3XGFP::TRP1; ura3-52::CFP-TUB1::URA3; SPC110-tdTomato::SpHIS5; ura3Δ::KanMX; Flag-pac1(N213A)*	This work
RPY1862	*MATa lys2-801; leu2-Δ1; his3-Δ200; trp1-Δ63; DYN1(D2868K)-3XGFP::TRP1; ura3-52::CFP-TUB1::URA3; SPC110-tdTomato::SpHIS5; ura3Δ::KanMX; Flag-pac1(W288D)*	This work
RPY1863	*MATa lys2-801; leu2-Δ1; his3-Δ200; trp1-Δ63;DYN1(D2868K)-3XGFP::TRP1; ura3-52::CFP-TUB1::URA3; SPC110-tdTomato::SpHIS5; ura3Δ::KanMX; Flag-pac1(N213A-W288D)*	This work
RPY1841	MATa *lys2-801 leu2-Δ1 his3-Δ200 trp1-Δ63 DYN1(F3446A-E3867A)-3XGFP::TRP1, ura3-52::CFP-TUB1::URA3, SPC110-tdTomato::SpHIS5, ura3Δ::KanMX*	This work
RPY1858	MATa *lys2-801 leu2-Δ1 his3-Δ200 trp1-Δ63 DYN1(D2868K-F3446A-E3867A)-3XGFP::TRP1, ura3-52::CFP-TUB1::URA3, SPC110-tdTomato::SpHIS5, ura3Δ::KanMX*	This work

2.7 References

1. Gillies JP, Reimer JM, Karasmanis EP, Lahiri I, Htet ZM, Leschziner AE, Reck-Peterson SL. Structural basis for cytoplasmic dynein-1 regulation by Lis1. *eLife* **11**, e71229 (2022).
2. Elshenawy MM, Kusakci E, Volz S, Baumbach J, Bullock SL, Yildiz A. Lis1 activates dynein motility by modulating its pairing with dynactin. *Nat. Cell Biol.* **22**, 570–578 (2020).
3. Gutierrez, P. A., Ackermann, B. E., Vershinin, M. & McKenney, R. J. Differential effects of the dynein-regulatory factor Lissencephaly-1 on processive dynein-dynactin motility. *J. Biol. Chem.* **292**, 12245–12255 (2017).
4. Kusakci E, Htet ZM, Zhao Y, Gillies JP, Reck-Peterson SL, Yildiz A. Lis1 slows force-induced detachment of cytoplasmic dynein from microtubules. *Nat. Chem. Biol.* **20**, 521–529 (2024).
5. Schmidt, H., Zalyte, R., Urnavicius, L. & Carter, A. P. Structure of human cytoplasmic dynein-2 primed for its power stroke. *Nature* **518**, 435–438 (2015).
6. DeSantis ME, Cianfrocco MA, Htet ZM, Tran PT, Reck-Peterson SL, Leschziner AE. Lis1 Has Two Opposing Modes of Regulating Cytoplasmic Dynein. *Cell* **170**, 1197-1208.e12 (2017).
7. Zhang K, Foster HE, Rondelet A, Lacey SE, Bahi-Buisson N, Bird AW, Carter AP. Cryo-EM Reveals How Human Cytoplasmic Dynein Is Auto-inhibited and Activated. *Cell* **169**, 1303-1314.e18 (2017).
8. Cianfrocco, M. A., DeSantis, M. E., Leschziner, A. E. & Reck-Peterson, S. L. Mechanism and Regulation of Cytoplasmic Dynein. *Annu. Rev. Cell Dev. Biol.* **31**, 83–108 (2015).
9. Heil-Chapdelaine, R. A., Oberle, J. R. & Cooper, J. A. The Cortical Protein Num1p Is Essential for Dynein-Dependent Interactions of Microtubules with the Cortex. *J. Cell Biol.* **151**, 1337–1344 (2000).
10. Sheeman B, Carvalho P, Sagot I, Geiser J, Kho D, Hoyt MA, Pellman D. Determinants of *S. cerevisiae* Dynein Localization and Activation. *Curr. Biol.* **13**, 364–372 (2003).
11. Eshel D, Urrestarazu LA, Vissers S, Jauniaux JC, van Vliet-Reedijk JC, Planta RJ, Gibbons IR. Cytoplasmic dynein is required for normal nuclear segregation in yeast. *Proc. Natl. Acad. Sci.* **90**, 11172–11176 (1993).
12. Li, Y. Y., Yeh, E., Hays, T. & Bloom, K. Disruption of mitotic spindle orientation in a yeast dynein mutant. *Proc. Natl. Acad. Sci.* **90**, 10096–10100 (1993).
13. Muhua, L., Karpova, T. S. & Cooper, J. A. A yeast actin-related protein homologous to that in vertebrate dynactin complex is important for spindle orientation and nuclear migration. *Cell* **78**, 669–679 (1994).
14. Lee, W.-L., Oberle, J. R. & Cooper, J. A. The role of the lissencephaly protein Pac1 during nuclear migration in budding yeast. *J. Cell Biol.* **160**, 355–364 (2003).
15. Lammers, L. G. & Markus, S. M. The dynein cortical anchor Num1 activates dynein motility by relieving Pac1/LIS1-mediated inhibition. *J. Cell Biol.* **211**, 309–322 (2015).
16. Markus, S. M. & Lee, W.-L. Regulated Offloading of Cytoplasmic Dynein from Microtubule Plus Ends to the Cortex. *Dev. Cell* **20**, 639–651 (2011).
17. Moore, J. K., Stuchell-Brereton, M. D. & Cooper, J. A. Function of dynein in budding yeast: Mitotic spindle positioning in a polarized cell. *Cell Motil.* **66**, 546–555 (2009).
18. Roberts, A. J., Goodman, B. S. & Reck-Peterson, S. L. Reconstitution of dynein transport to the microtubule plus end by kinesin. *eLife* **3**, e02641 (2014).
19. Markus SM, Plevock KM, St Germain BJ, Punch JJ, Meaden CW, Lee WL. Quantitative analysis of Pac1/LIS1-mediated dynein targeting: Implications for regulation of dynein activity in budding yeast. *Cytoskeleton* **68**, 157–174 (2011).
20. Carvalho, P., Gupta, M. L., Hoyt, M. A. & Pellman, D. Cell Cycle Control of Kinesin-Mediated Transport of Bik1 (CLIP-170) Regulates Microtubule Stability and Dynein Activation. *Dev. Cell* **6**, 815–829 (2004).
21. Caudron, F., Andrieux, A., Job, D. & Boscheron, C. A new role for kinesin-directed transport of Bik1p (CLIP-170) in *Saccharomyces cerevisiae*. *J. Cell Sci.* **121**, 1506–1513 (2008).
22. Marzo, M. G., Griswold, J. M. & Markus, S. M. Pac1/LIS1 stabilizes an uninhibited conformation of dynein to coordinate its localization and activity. *Nat. Cell Biol.* **22**, 559–569 (2020).
23. Htet ZM, Gillies JP, Baker RW, Leschziner AE, DeSantis ME, Reck-Peterson SL. LIS1 promotes the formation of activated cytoplasmic dynein-1 complexes. *Nat. Cell Biol.* **22**, 518–525 (2020).
24. Reimer, J. M., DeSantis, M. E., Reck-Peterson, S. L. & Leschziner, A. E. Structures of human dynein in complex with the lissencephaly 1 protein, LIS1. *eLife* **12**, e84302 (2023).
25. Urnavicius L, Zhang K, Diamant AG, Motz C, Schlager MA, Yu M, Patel NA, Robinson CV, Carter AP. The structure of the dynactin complex and its interaction with dynein. *Science* **347**, 1441–1446 (2015).

26. Han BG, Watson Z, Kang H, Pulk A, Downing KH, Cate J, Glaeser RM. Long shelf-life streptavidin support-films suitable for electron microscopy of biological macromolecules. *J. Struct. Biol.* **195**, 238–244 (2016).
27. Lahiri I, Xu J, Han BG, Oh J, Wang D, DiMaio F, Leschziner AE. 3.1 Å structure of yeast RNA polymerase II elongation complex stalled at a cyclobutane pyrimidine dimer lesion solved using streptavidin affinity grids. *J. Struct. Biol.* **207**, 270–278 (2019).
28. Wagner T, Merino F, Stabrin M, Moriya T, Antoni C, Apelbaum A, Hagel P, Sitsel O, Raisch T, Prumbaum D, Quentin D, Roderer D, Tacke S, Siebolds B, Schubert E, Shaikh TR, Lill P, Gatsogiannis C, Raunser S. SPHIRE-crYOLO is a fast and accurate fully automated particle picker for cryo-EM. *Commun. Biol.* **2**, 1–13 (2019).
29. Zivanov J, Nakane T, Forsberg BO, Kimanius D, Hagen WJ, Lindahl E, Scheres SH. New tools for automated high-resolution cryo-EM structure determination in RELION-3. *eLife* **7**, e42166 (2018).
30. Punjani, A., Zhang, H. & Fleet, D. J. Non-uniform refinement: adaptive regularization improves single-particle cryo-EM reconstruction. *Nat. Methods* **17**, 1214–1221 (2020).
31. Punjani, A., Rubinstein, J. L., Fleet, D. J. & Brubaker, M. A. cryoSPARC: algorithms for rapid unsupervised cryo-EM structure determination. *Nat. Methods* **14**, 290–296 (2017).
32. Zheng SQ, Palovcak E, Armache JP, Verba KA, Cheng Y, Agard DA. MotionCor2: anisotropic correction of beam-induced motion for improved cryo-electron microscopy. *Nat. Methods* **14**, 331–332 (2017).
33. Rohou, A. & Grigorieff, N. CTFFIND4: Fast and accurate defocus estimation from electron micrographs. *J. Struct. Biol.* **192**, 216–221 (2015).
34. Bepler, T., Kelley, K., Noble, A. J. & Berger, B. Topaz-Denoise: general deep denoising models for cryoEM and cryoET. *Nat. Commun.* **11**, 5208 (2020).
35. Afonine PV, Poon BK, Read RJ, Sobolev OV, Terwilliger TC, Urzhumtsev A, Adams PD. Real-space refinement in PHENIX for cryo-EM and crystallography. *Acta Crystallogr. Sect. Struct. Biol.* **74**, 531–544 (2018).
36. Emsley, P., Lohkamp, B., Scott, W. G. & Cowtan, K. Features and development of Coot. *Acta Crystallogr. D Biol. Crystallogr.* **66**, 486–501 (2010).
37. Song Y, DiMaio F, Wang RY, Kim D, Miles C, Brunette T, Thompson J, Baker D. High-Resolution Comparative Modeling with RosettaCM. *Structure* **21**, 1735–1742 (2013).
38. Redwine WB, DeSantis ME, Hollyer I, Htet ZM, Tran PT, Swanson SK, Florens L, Washburn MP, Reck-Peterson SL. The human cytoplasmic dynein interactome reveals novel activators of motility. *eLife* **6**, e28257 (2017).
39. Longtine MS, McKenzie A 3rd, Demarini DJ, Shah NG, Wach A, Brachat A, Philippsen P, Pringle JR. Additional modules for versatile and economical PCR-based gene deletion and modification in Saccharomyces cerevisiae. *Yeast* **14**, 953–961 (1998).
40. Gietz, R. D. & Schiestl, R. H. High-efficiency yeast transformation using the LiAc/SS carrier DNA/PEG method. *Nat. Protoc.* **2**, 31–34 (2007).
41. Schindelin J, Arganda-Carreras I, Frise E, Kaynig V, Longair M, Pietzsch T, Preibisch S, Rueden C, Saalfeld S, Schmid B, Tinevez JY, White DJ, Hartenstein V, Eliceiri K, Tomancak P, Cardona A. Fiji: an open-source platform for biological-image analysis. *Nat. Methods* **9**, 676–682 (2012).
42. Reck-Peterson SL, Yildiz A, Carter AP, Gennerich A, Zhang N, Vale RD. Single-Molecule Analysis of Dynein Processivity and Stepping Behavior. *Cell* **126**, 335–348 (2006).
43. Huang, J., Roberts, A. J., Leschziner, A. E. & Reck-Peterson, S. L. Lis1 Acts as a "Clutch" between the ATPase and Microtubule-Binding Domains of the Dynein Motor. *Cell* **150**, 975–986 (2012).
44. Schlager, M. A., Hoang, H. T., Urnavicius, L., Bullock, S. L. & Carter, A. P. In vitro reconstitution of a highly processive recombinant human dynein complex. *EMBO J.* **33**, 1855–1868 (2014).
45. Baumbach J, Murthy A, McClintock MA, Dix CI, Zalyte R, Hoang HT, Bullock SL. Lissencephaly-1 is a context-dependent regulator of the human dynein complex. *eLife* **6**, e21768 (2017).

2.8 Acknowledgment

Chapter 2, in full, is a reprint of the material as it appears in *Nature Structural & Molecular Biology*: *Lis1 relieves cytoplasmic dynein-1 autoinhibition by acting as a molecular wedge*. Karasmanis, E.P.; Reimer, J.M.; Kendrick, A.A.; Nguyen, K.H.V.; Rodriguez, J.A.; Truong, J.B.; Lahiri, I.; Reck-Peterson, S.L.; Leschziner, A.E. The dissertation author contributed significantly to this work.

Chapter 3 Cryo-EM visualizes multiple steps of dynein's activation pathway

3.1 Results

Cryo-EM reveals different dynein conformations in the presence of Lis1 and ATP

Previous high-resolution structures of dynein in complex with Lis1 described the interactions between these proteins. However, these structures were solved using mutations or non-hydrolyzable ATP analogs that limited the ability to capture dynein's structural dynamics[1–4]. To characterize the conformational landscape of dynein during Lis1 binding and ATP hydrolysis, we employed a time-resolved freezing approach. We purified wild-type yeast dynein monomer (amino acids 1352-4092) in the absence of any nucleotide and plunge froze grids after the addition of excess ATP (500-fold) at two different time points (0.5 min and 30 min), incubating the samples at 4°C to slow down nucleotide hydrolysis. We also prepared grids with samples that were pre-incubated with Lis1 prior to ATP addition (Fig. 3.1a). After data collection and analysis (Supplementary Fig. 3.1 – 3.4, and Table 3.1 and 3.2), we observed the expected high level of heterogeneity in our datasets. We grouped the reconstructions into three distinct conformations based on the position of dynein's linker, a mechanical element that adopts different conformations in response to the ATP hydrolysis-driven opening and closing of the ring: "straight" – S, yellow outline (Fig. 3.1b), "interm" (intermediate) – I, green outline (Fig. 3.1c), and "bent" – B, blue outline (Fig. 3.1d). We named all our maps with letters corresponding to the different conformational states and numbers starting with the shorter time point (0.5 min) (Supplementary Fig. 3.1 – 3.4, and Table 3.1 and 3.2).

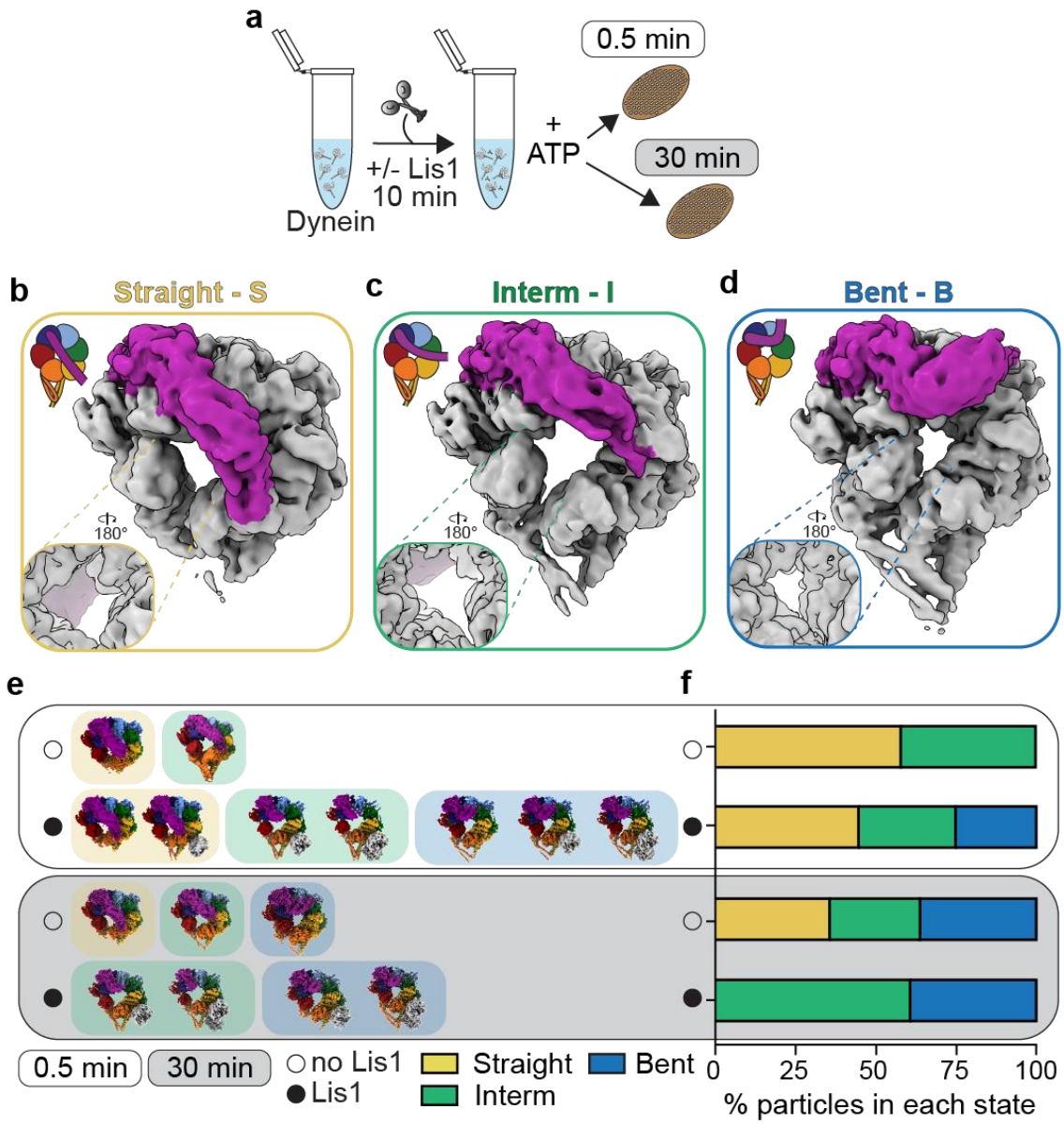

Figure 3.1 Time-resolved cryo-EM captures Lis1's effect on dynein's conformational landscape during ATP hydrolysis.

a, Experimental setup. **b, – d,** The three major groups of conformations identified in the datasets are shown on locally refined cryo-EM volumes filtered to 6 Å: **b,** straight linker (S) – yellow outline, **c,** intermediate (Interm, I) linker – green out- line, and **d,** bent linker (B) – blue outline. The linker region is highlighted in magenta. The extent of ring opening is shown to the left of each panel. **e,** Different conformations were identified in each dataset in the absence (open circle) or presence of Lis1 (black circle) at two different time points (0.5 min – white background and 30 min – gray background). **f,** Relative abundance of particles belonging to different states obtained from particle distributions in cryo-EM datasets in the absence (open circle) or presence of Lis1 (black circle) at two different time points (0.5 min – white background and 30 min – gray background).

To understand how Lis1 binding affects dynein's conformational landscape, we next examined the number of total particles that belong to each conformation (bent – blue, intermediate – green, and straight – yellow) in each dataset collected at the two different timepoints and in the presence or absence of Lis1 (Fig. 3.1e). Although the individual conformations within each sample (dynein or dynein + Lis1) at different time points were the same, their distribution changed. Our analysis showed that more conformations are present in the dynein alone sample when the incubation is extended from 0.5 min to 30 min (Fig. 3.1e-f). However, the addition of Lis1 increases the number of states dynein samples in the shorter time point (0.5 min) (Fig. 3.1e-f). To exclude the possibility that these differences could reflect the different sizes of datasets, we repeated the analysis by combining data belonging to the same experimental condition (+Lis1 or -Lis1) but were collected at different time points (Supplementary Fig. 3.5a-b). Because these datasets were collected using different microscopes, we only processed them together until we obtained initial 3D reconstructed models, without any prior structural information. We then mapped the particles of each model to their corresponding datasets and conformational subgroups (bent, intermediate, and straight linker). This analysis showed a similar increase in the number of conformational states seen in the presence of Lis1 at a shorter time point as the one we observed when each dataset was processed separately (Supplementary Fig. 3.5c). This suggests that Lis1 may be facilitating dynein's transition between different conformations, allowing dynein to sample more states. Next, we will discuss the different dynein conformations we observed in the absence and presence of Lis1, followed by how these conformations might explain the effects of Lis1 on dynein's mechanochemistry.

Dynein's conformational landscape during ATP hydrolysis

To understand how ATP hydrolysis affects dynein structurally, we built models for the different high-resolution dynein conformations identified in our datasets and mapped nucleotides to their binding pockets, as all our structures showed nucleotide densities in the AAA modules (Fig. 3.2a, b, and c, Supplementary Fig. 3.4a – S1 and S4, 3.4b – I4, 3.4c – B2, and, and Supplementary Fig. 3.6a). In each linker state (bent, intermediate, and straight) dynein is bound to ADP in AAA1 and AAA3, although in some states there is also density for Mg^{2+}, indicating a tighter binding state, as Mg^{2+} release weakens ADP binding[5,6]. Although our maps only have partial densities in the stalk region, the ring opening and the stalk's CC1 and CC2 positions in dynein with a straight linker is consistent with a strong microtubule binding state, as indicated by the lack of bulging of CC2 in the stalk region characteristic of the weak microtubule binding state (Fig. 3.2a – Stalk vs. 3.2c – Stalk)[7]. The intermediate linker dynein has partial density that fits a model in which the CC2 has a slight bulge in the stalk and is consistent with a semi-α or semi-bent state that could represent an intermediate microtubule binding state (Fig. 3.2b – Stalk)[8–10]. In agreement with having occupied nucleotide binding pockets, the ring of the straight linker dynein is more closed than in the crystal structure of apo-dynein (PDB: 4AI6, Fig. 3.2d). We see a partial closing of the AAA1 binding pocket, indicative of a post-hydrolysis ADP-bound state (Fig. 3.2e), and ADP and Mg^{2+} in AAA3 in both straight and intermediate dynein as opposed to ADP without Mg^{2+} in the bent linker dynein (Fig. 3.2a) or crystal structure (PDB: 4AI6, Fig. 3.2f)[11].

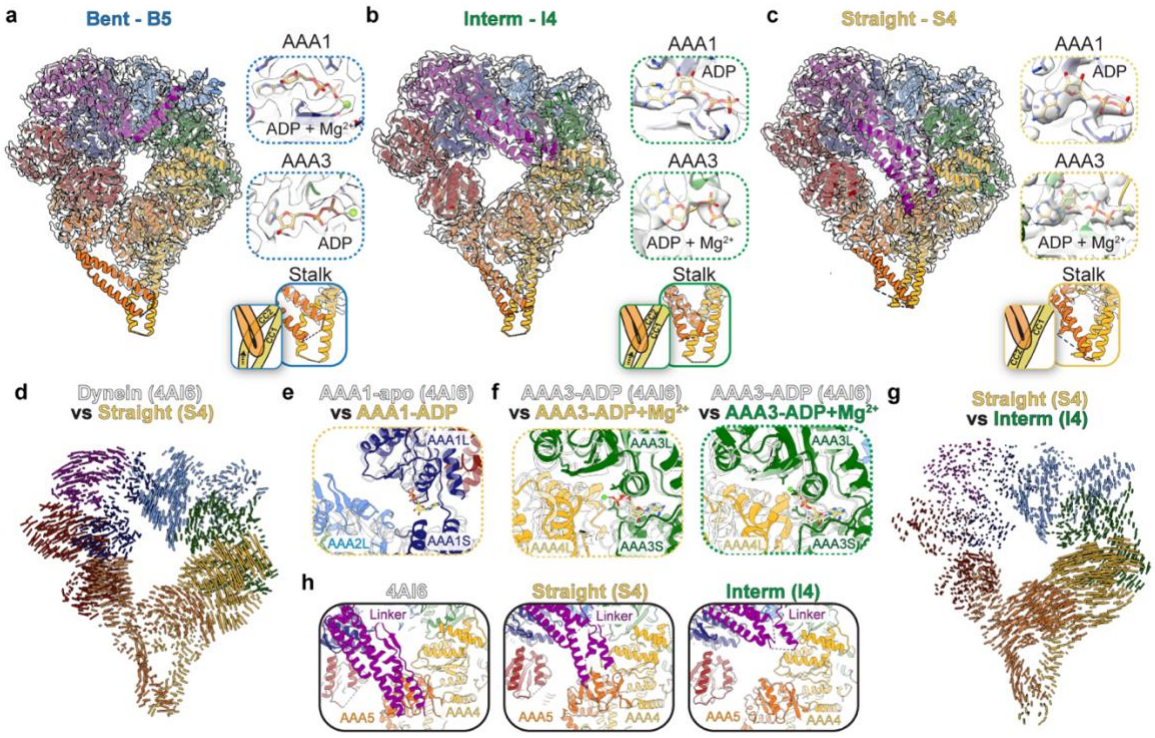

Figure 3.2 Conformational landscape of dynein during ATP hydrolysis

a,-c, Models of dynein for the bent – B5 (**a**), intermediate – I4 (**b**), and straight – S4 (**c**) conformations from the 30 min with ATP dataset fit into their corresponding cryo-EM density maps. Each structural element is colored based on the dynein schematic in Fig. 2.1a. To the right of each fitted model are close ups of the nucleotide-binding pockets for AAA1 and AAA3, and of the predicted stalk conformations. **d,** Map of pairwise alpha-carbon distances between straight linker model (S4) and an X-ray structure of S. cerevisiae dynein in AAA1-apo (PDB: 4AI6), with the models aligned relative to their AAA1 modules. The length of each vector is proportional to the interatomic distance. Residues 1361-1772 of the linker were removed for clarity. **e,** Comparison of AAA1 nucleotide binding pockets for straight linker dynein (S4) bound to ADP with S. cerevisiae in AAA1-apo (PDB: 4AI6). The models were aligned based on residues 1797-1894 in AAA1. **f,** Comparison of AAA3 nucleotide binding pockets for straight linker dynein (S3, left panel – yellow outline) and intermediate linker dynein (I4, right panel – green outline) with S. cerevisiae (PDB: 4AI6). The models were aligned based on residues 2377-2445 in AAA3. **g,** View of linker docking in PDB: 4AI6 (left panel), straight linker conformation (S4, middle panel), and intermediate linker conformation (I4, right panel). **h,** Map of pairwise alpha-carbon distances between the straight linker (S4) and the intermediate linker (I4) models. The length of each vector is proportional to the interatomic distance. The models were aligned relative to their AAA1 modules. Residues 1361-1772 of the linker were removed for clarity.

The intermediate linker dynein states identified in our datasets have similar conformations to the ones identified in a recent analysis of full length human dynein[12]. In our dataset, the comparison of the straight and intermediate linker dynein shows movement in the AAA domains, even though the nucleotide states are the same in these structures (Fig. 3.2g, and 3.2b and 3.2c). While the linker docks at AAA5 in the apo (PDB: 4AI6) and straight linker dynein, the linker docks at AAA4 in the intermediate linker dynein (Fig. 3.2h). These differences in the ring and linker without corresponding changes in the nucleotide state suggest some flexibility in dynein that is independent of ATP hydrolysis and is consistent with previous FRET analysis and recent human dynein structures[12,13].

The effect of Lis1 on dynein's conformational landscape

To understand how Lis1 affects dynein's mechanochemistry, we next analyzed the datasets where dynein had been preincubated with Lis1 before the addition of ATP. These datasets also showed high level of heterogeneity with the bent and intermediate linker dynein states in the 0.5 min and 30 min conditions (Fig. 3.3a and 3.3b, and Supplementary Fig. 3.6b and 3.6c) while the straight linker states where only detected in the 0.5 min condition (Fig. 3.1g and 1h, 3.3c and 3.3d, and Supplementary Fig. 3.6b). In addition, the nucleotide occupancies and stalk conformations in these different dynein states are similar to those seen in the absence of Lis1 (Fig. 3.2a – c and 3.3a – d, Supplementary Fig. 3.4 and 3.6).

Figure 3.3 Lis1 binding to dynein expands dynein's conformational landscape.

a,-d, Models of dynein bound to Lis1 for: the bent – B6 (**a**) and intermediate – I5 (**b**) dynein from the same dataset (dynein with Lis1 incubated for 30 min with ATP), and straight with Lis1 bound – S3 (**c**) and straight with no Lis1 bound – S2 (**d**) dynein from the same dataset (dynein with Lis1 incubated for 0.5 min with ATP), fit into their corresponding cryo-EM density maps. Each structural element is colored based on the dynein schematic in Fig. 2.1a. To the right of each fitted model are views of the nucleotide binding pockets for AAA1 and AAA3 and of the stalk conformations. **e,** Additional cryo-EM maps obtained after heterogeneity analysis of bent (blue box) and intermediate (green box) dynein conformations from the dynein with Lis1 incubated for 0.5 min with ATP dataset after 3D classification show one or two Lis1 bound to dynein. **f,** Comparison of linker (magenta) in straight linker dynein (S3, yellow) bound to Lis1 with linker (white) in straight linker dynein (S2, white) with no Lis1 bound. The models were aligned based on the position of AAA1. **G,** Comparison of models built for intermediate state dynein (I6, green) bound to 2 Lis1 β-propellers (gray) with straight linker dynein (S3, yellow) bound to one Lis1 β-propeller (white). The two Lis1 binding sites are highlighted. The models were aligned based on the position of Lis1 bound to $site_{ring}$. **h,** The dynein/ Lis1 binding sites from g.

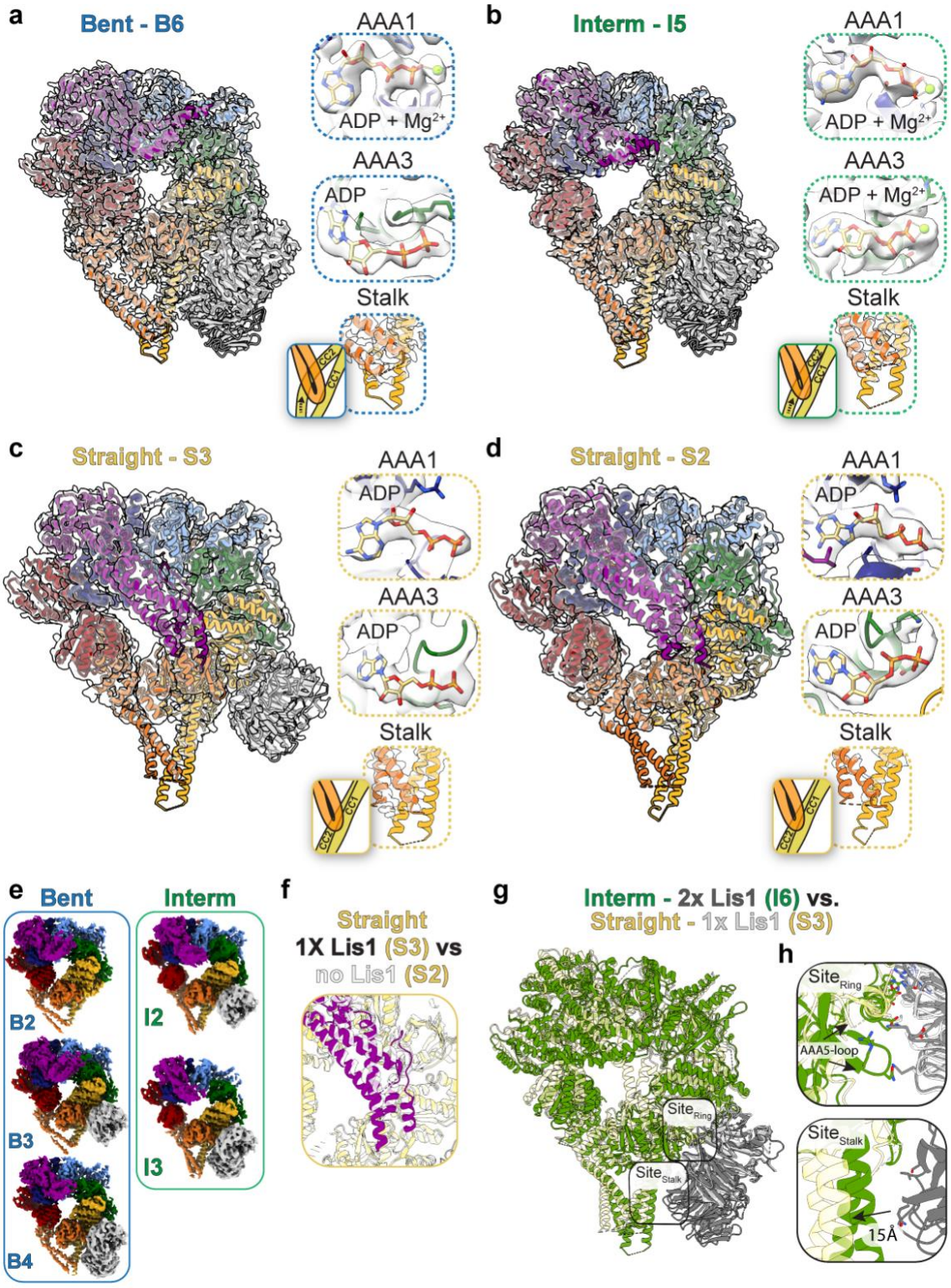
a
Bent - B6
AAA1
ADP + Mg2+
AAA3
ADP
Stalk
CC2
CC1
b
Interm - I5
AAA1
ADP + Mg2+
AAA3
ADP + Mg2+
Stalk
CC2
CC1
c
Straight - S3
AAA1
ADP
AAA3
ADP
Stalk
CC2
CC1
d
Straight - S2
AAA1
ADP
AAA3
ADP
Stalk
CC2
CC1
e
Bent
Interm
B2
B3
B4
I2
I3
f
Straight
1X Lis1 (S3) vs
no Lis1 (S2)
g
Interm - 2x Lis1 (I6) vs.
Straight - 1x Lis1 (S3)
Site Ring
Site Stalk
h
Site Ring
AAA5-loop
Site Stalk
15Å

Because some of our maps showed partial density for the Lis1 β-propellers, we performed 3D classifications without alignment in Relion to further resolve this compositional heterogeneity (Supplementary Fig. 3.2 and 3.3). This analysis separated states where we see no, one, or two Lis1 β-propellers bound to dynein (Fig. 3.3e and Supplementary Fig. 3.2 – 3.4, and 3.6d and e). The nucleotide occupancies in these new maps correspond to the nucleotides observed in pre-3D classification maps (Fig. 3.3a – d, Supplementary Fig. 3.4 and 3.6). In addition, the interaction sites between Lis1 and dynein in our maps are those previously characterized and are largely the same in the bent and intermediate dynein states (Supplementary Fig. 3.7a – c).

Dynein linker position controls binding to a second Lis1

Previous low-resolution data showed that dynein in a strong microtubule binding state binds one Lis1 β-propeller at site$_{ring}$[3]. However, that structure was in a straight linker state, emphasizing the linker position as a critical aspect in Lis1 binding to dynein. Our straight linker map also had one Lis1 β-propeller bound (Fig. 3.3c). Aligning straight linker dynein with or without Lis1 by AAA1 shows that the linker shifts slightly to accommodate for Lis1 binding (Fig. 3.3f). We also saw clear density for the second Lis1 β-propeller in the intermediate state dynein, even though the nucleotide densities in this state are consistent with the ones in the straight linker dynein (Fig. 3.3b and Supplementary Fig. 3.4b and 3.6). Comparison of this state (I6, 3.4 Å resolution) with our straight linker dynein (I3, 4 Å resolution) bound to one Lis1 β-propeller showed that the site$_{ring}$ interactions are conserved while site$_{stalk}$ is shifted away from Lis1 as dynein goes from the intermediate to the straight linker state (~15 Å) and is therefore not accessible for the second Lis1 β-propeller to bind (Fig. 3.3g and h). Binding of Lis1 at the second

site is likely not to happen without the cooperativity from Lis1 bound at site$_{ring}$. This is consistent with previous lower resolution structures suggesting that the straight linker dynein conformation is incompatible with the second Lis1 β-propeller binding[1,3,14].

In our straight linker dynein bound to one Lis1 at site$_{ring}$ the density for the AAA5 loop is missing, while it is present in the intermediate or bent linker structures bound to one or two Lis1 (Fig. 3.3h – top panel and Supplementary Fig. 3.7a). Importantly, mutation of this loop (N3475 and N3476) or the corresponding residues D253 and H254 in Lis1 disrupts dynein's interaction with Lis1 and leads to binucleate phenotypes in yeast, suggesting that this interaction may only take place when dynein transitions from straight to intermediate or bent linker states[1].

Lis1 increases dynein's basal ATP hydrolysis rate

Our analysis showed that dynein sampled more conformations at the shorter time point in the presence of Lis1 (Fig. 3.1g and h, and Supplementary Fig. 3.5c). We hypothesized that Lis1 could accomplish this by increasing dynein's basal ATP hydrolysis rate. Several studies have shown that Lis1 does not affect dynein's microtubule-stimulated ATPase activity[14–16]. However, the contribution of Lis1 to dynein's basal ATPase hydrolysis rate (in the absence of microtubules) has not been fully established[14,15]. To test our hypothesis, we incubated the same dynein monomer (amino acids 1352-4092) as the one used in cryo-EM studies with increasing concentrations of Lis1 and measured dynein's basal ATP hydrolysis rate. We observed a Lis1 concentration-dependent increase in ATP hydrolysis rate (Fig. 3.4). Importantly, binding of Lis1 to dynein is required for this effect as the rate did not increase in the presence of a Lis1 mutant that does not bind to dynein (Lis1^{5A}: R275A, R301A, R378A, W419A, K437A) (Fig. 3.4)[3,14,17].

This observation supports our hypothesis that Lis1 binding allows dynein to sample more conformations by increasing dynein's basal ATP hydrolysis rate.

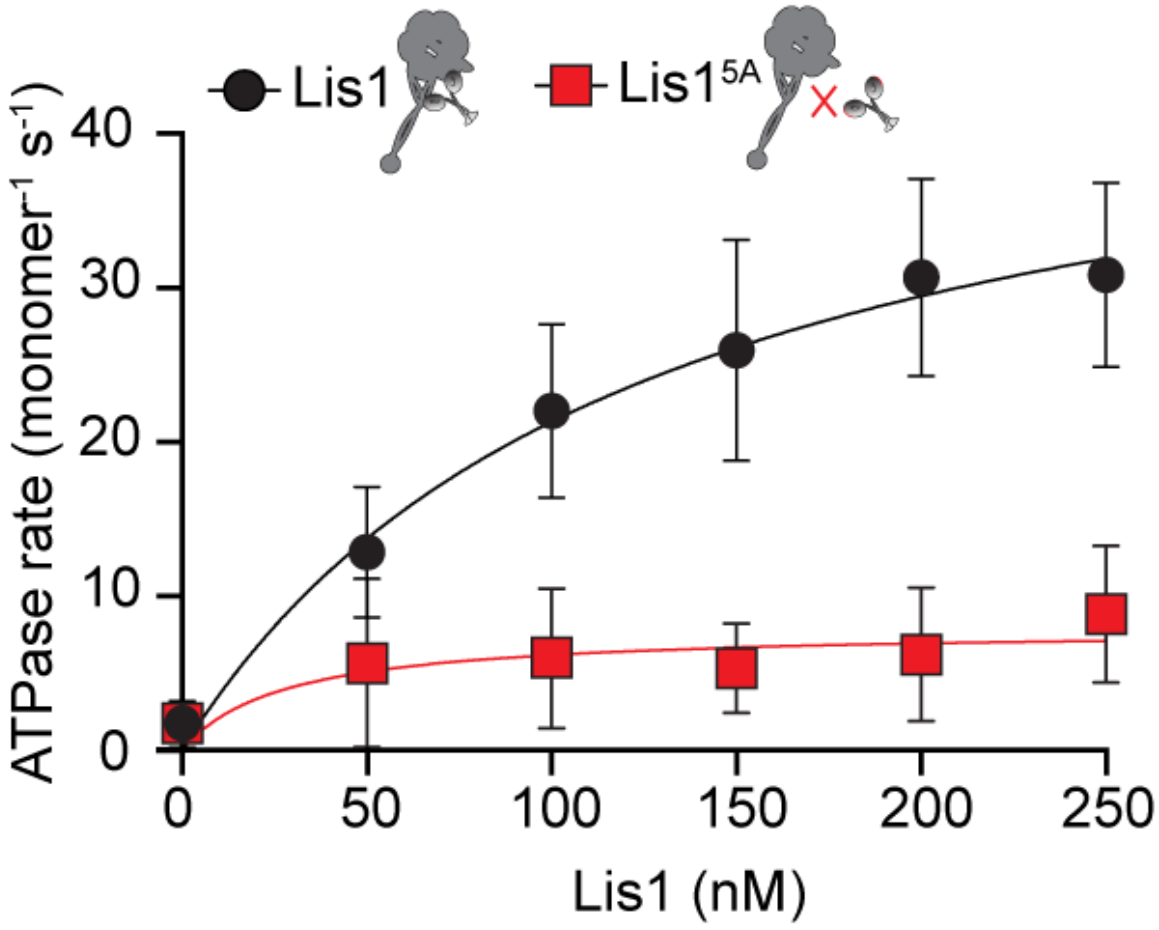

Figure 3.4 Lis1 increases dynein's basal ATPase activity. ATPase activity of dynein in the presence of increasing concentrations of wild-type Lis1 (black dots) or a Lis1 mutant that does not bind to dynein ($Lis1^{5A}$, red squares). Mean values (+/- SD) from three independent experiments are shown. Fitted values (+/- standard error of the fit) k_{basal}= 0.837 +/- 0.08 sec^{-1}, k_{cat}[Lis1]= 25.75 +/- 2.4 sec^{-1}.

Dynein activation is driven by its mechanochemical cycle

To understand how Lis1 is increasing dynein's ATPase rate, we further analyzed the interactions that the linker makes with the dynein motor domain, as these interactions have been

previously shown to be important for dynein's mechanochemistry[14,18,19]. We reasoned that the linker conformation in the different dynein states could explain how Lis1 regulates dynein's mechanochemistry given the changes in linker position associated with ATP hydrolysis and Lis1 binding.

Two models for how swinging of the linker is regulated during ATP hydrolysis have been proposed. In the linker/AAA2 model, loops in AAA2 (pre-sensory I – PS1 and helix 2 – H2) rearrange during ATP hydrolysis in AAA1 leading to an interaction with the linker hinge and subsequent bending and swinging of the linker (Fig. 3.5a). Consistent with this, deleting the H2 region in *Dictyostelium* dynein reduces dynein's basal and microtubule-stimulated ATPase activity[18]. In our straight and intermediate dynein state, when Lis1 is not bound to dynein the linker is contacting the AAA2 H2 loop, but these contact sites are less resolved when Lis1 is bound, suggesting lesser engagement of this region (Fig. 3.5b left and middle panels vs. right panel). This could mean that the need for this interaction is bypassed when Lis1 is bound to dynein due to the Lis1-driven increased flexibility in dynein.

In the linker docking model, ATPase-induced changes in AAA1 propagate to the linker docking interface on the motor domain to induce linker swing (Fig. 3.5a). Because our models lacked density for the linker docking sites when Lis1 was bound to dynein in the intermediate state, we performed heterogeneity analysis of all particles that belong to the intermediate state from the dataset collected in the presence of Lis1 and at the 0.5 min time point (Supplementary Fig. 3.2b and 3.4b – I1). In addition to separating the populations that have one or two Lis1 β-propellers bound, we observed other conformational changes that correspond to linker movement (Supplementary Fig. 3.2a). We then picked particles from the states that showed the most linker density, regardless of whether they had one or two Lis1 β-propellers bound. Although this

analysis did not improve the resolution of our maps, it did allow us to extend the modeling of the linker in the region where it could potentially dock on dynein. For each density map generated in this analysis, the linker comes close to AAA4 or the interface between AAA3 and AAA4 (Fig. 3.5c and Supplementary Fig. 3.2c).

We next compared these linker docking interfaces with intermediate-state dynein observed in the absence of Lis1. The presence of Lis1 led to conformational changes in AAA1 through AAA5 (Fig. 3.5d). The linker is also shifted, with the docking site much closer to the interface between AAA4 and AAA5 when Lis1 is not present (Fig. 3.5e and f). Interestingly, in the Lis1-bound dynein, the linker is close to D2868 (3045 in human dynein), a residue that makes important contacts with the linker of the opposing dynein in the Phi particle (Fig 3.5f – bottom panel and g)[20]. A charge-reversing mutation in this residue disrupts Phi particle formation and almost completely bypasses the need for Lis1 in yeast. Given that Phi traps dynein in a single conformation, and that conformational changes such as opening and closing of the ring and linker swing are required for dynein to go through its mechanochemical cycle, we reasoned that the Phi conformation inhibits dynein's mechanochemistry, in addition to preventing it from binding to microtubules. This leads to the prediction that disrupting Phi particle formation would increase dynein's basal ATPase hydrolysis rate. To test this, we used GST-dynein, as the Phi-disrupting D2868K mutation in this construct does not affect dynein's motile properties or Lis1 binding[21]. The ATPase rate of GST-dynein-D2868K was almost double that of the wild-type construct, suggesting that Phi conformation inhibits dynein's ability to hydrolyze ATP (Fig. 3.5h). Addition of Lis1 continued to increase dynein's ATPase rate implying that there are likely other interactions important to this process (Fig. 3.5i).

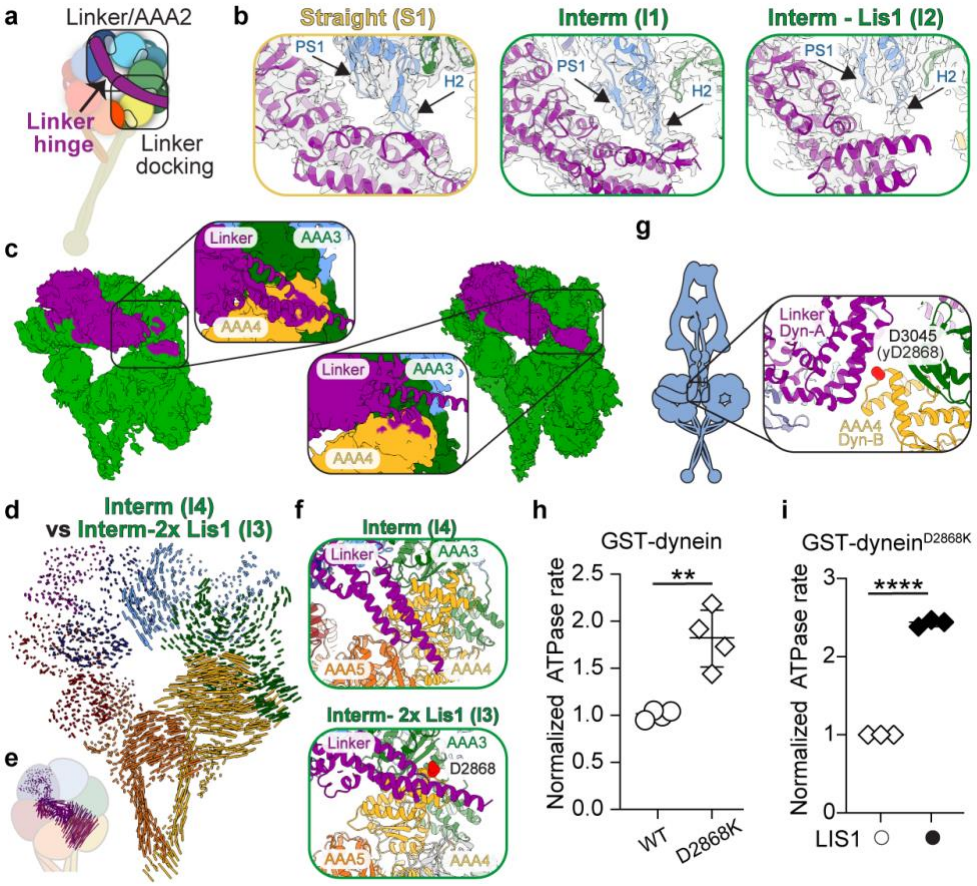

Figure 3.5 Conformational changes and Lis1 binding regulate dynein's basal ATP-hydrolysis rate.

a, Schematic of the two important interaction regions between dynein's linker and motor domain. **B,** The proximity of the P1 sensor (PS1) and H2 insert loops in AAA2 (blue) to the linker (magenta) hinge region in the indicated models. **c,** Density maps and close-ups for subsets of particles selected from cryoDRGN analysis that showed the most extensive linker density. Close-ups show predicted linker (magenta) docking sites on AAA4 (yellow) after fitting an extended linker model in the density maps. **d,** Map of pairwise alpha-carbon distances between the intermediate linker model and the intermediate linker model bound to two Lis1 β-propellers. The models were aligned by their AAA1 modules. Residues 1361-1772 of the linker were removed for clarity. **e,** Residues 1352-1772 of the linker from the map of pairwise alpha-carbon distances between the intermediate linker model and the intermediate linker model bound to two Lis1 β-propellers in d. **f,** View of linker docking in intermediate linker dynein bound to Lis1 β-propellers (top panel) and intermediate linker dynein (bottom panel). Residue D2686 is highlighted in red. **g,** View of the location of residue D3045 (yeast D2868) in human dynein Phi particle (PDB: 5NVU). **h,** Normalized ATPase activity (median ± interquartile range) of GST-dynein and GST-dyneinD2868K. **, p = 0.0022. Data from four independent experiments. **i,** Normalized ATPase activity (median ± interquartile range) of GST-dyneinD2868K in the absence (white circles) or presence (black circles) of Lis1. ****, $p < 0.0001$. Data from three independent experiments.

Lis1 might be facilitating nucleotide release from AAA3

Finally, to better understand Lis1's effects on dynein's mechanochemistry, we turned to all-atom molecular dynamic (MD) simulations. We first asked how the presence of Lis1 influences dynein's linker bending, given the importance of linker position in the mechanochemical cycle (Fig. 3.5a)[18,19]. To do this, we first defined the linker rotation angle between residues S1942 (AAA1), L1664 (linker), and K1424 (extended part of the linker) in our highest resolution dynein models obtained in this work: bent-1x Lis1 (Fig. 3.3e – B7), interm-1x Lis1 (Fig. 3.5d – I6), interm-2x Lis1 (Fig. 3.5d – I7), and interm dynein (Fig. 3.2b – I4), and determined from heterogeneity analysis, in which we modeled the same number of residues for the linker region (Methods and Fig. 3.6a). For each state, we launched multiple Gaussian Accelerated MD simulations (Methods), which can enhance the conformational sampling of molecular machines, and measured population density for the different linker angles. Our analysis shows that the linker rotation is more constrained when Lis1 is bound to dynein in the intermediate state (Fig. 3.6b). Likely, this is caused by the steric hindrance from Lis1 binding to dynein.

We next evaluated if the residue D2868, a key residue in maintaining Phi particle formation could be making contacts with the linker when Lis1 is bound to dynein. We found that D2868 forms a salt bridge with K1424 (linker), which could stabilize the intermediate linker position when Lis1 is bound to dynein in this state (Fig. 3.6c). This salt bridge is relatively stable in the simulation with the intermediate dynein bound to one Lis1 β-propeller (Fig. 3.6c – top

panel), whereas a disengaged configuration is preferred in the intermediate dynein bound to two β-propellers (Fig. 3.6c – bottom panel).

Lastly, we asked whether the presence of Lis1 could be affecting the nucleotide binding pockets in AAA1 and AAA3 in our simulations. The analysis of the contact area between AAA1 and AAA2 revealed that the bent linker enables a tighter interface than that in the intermediate linker state, presumably allowing this site to become more hydrolysis competent (Fig. 2.6d). This is consistent with closing of the AAA1 interface in the bent conformation seen for *Dictyostelium* dynein in the pre-power stroke state primed for ATP hydrolysis[7]. We next investigated the AAA3 and AAA4 contact area and showed that Lis1 binding loosens the AAA3 and AAA4 interface, potentially favoring ADP release from the AAA3 binding pocket (Fig. 2.6e). Interestingly, binding of the second Lis1 β-propeller further loosens the interface, as illustrated by comparing the population distributions of interm-2x Lis1 vs. interm-1x Lis1 systems (Fig. 2.6e, dotted vs. solid green lines). This analysis suggests that Lis1 might be increasing dynein's basal ATP hydrolysis rate by facilitating nucleotide release from AAA3.

Figure 3.6 Molecular dynamics support changes in dynein conformations due to Lis1 binding.

a, The linker rotation angles defined by the Cα atoms of residues located in AAA2 (S1942, corner) and linker – corner (L1664 – S1924, edge 1) and linker – corner (L1664 – K1424, edge 2) for the four systems used in the molecular dynamic simulations: bent linker with one Lis1 β-propellers bound (B7, solid blue line), intermediate linker with one Lis1 β-propeller bound (I6, solid green line), intermediate linker with two Lis1 β- propellers bound (I7, dotted green line), and intermediate linker (I4, large dot green line). **b,** Population density for the linker rotation angles for the four simulation systems. **c,** Predicted salt bridge between D2868 in AAA3 and K1424 in the linker for intermediate linker with one Lis1 β- propeller bound (I6 – top panel) and intermediate linker with two Lis1 β- propellers bound (I7 – bottom panel). **d,** Distribution of contact area surface between AAA1 and AAA2 (insert – red arrow points to the interface) in the simulations. **e,** Distribution of contact area surface between AAA3 and AAA4 domains (insert – red arrow points to the interface) in the simulations. **f,** Model of dynein activation and the proposed placement of the identified structures in the model. 1 – dynein in the Phi particle, 2 – initial step of Chi particle formation, 3 – Chi particle, 4 – increase in dynein's basal ATP hydrolysis rate, 5 – full dynein complex assembles with dynactin and an activating adaptor, and binds to microtubules, 6 – Lis1 dissociates from active dynein complex.

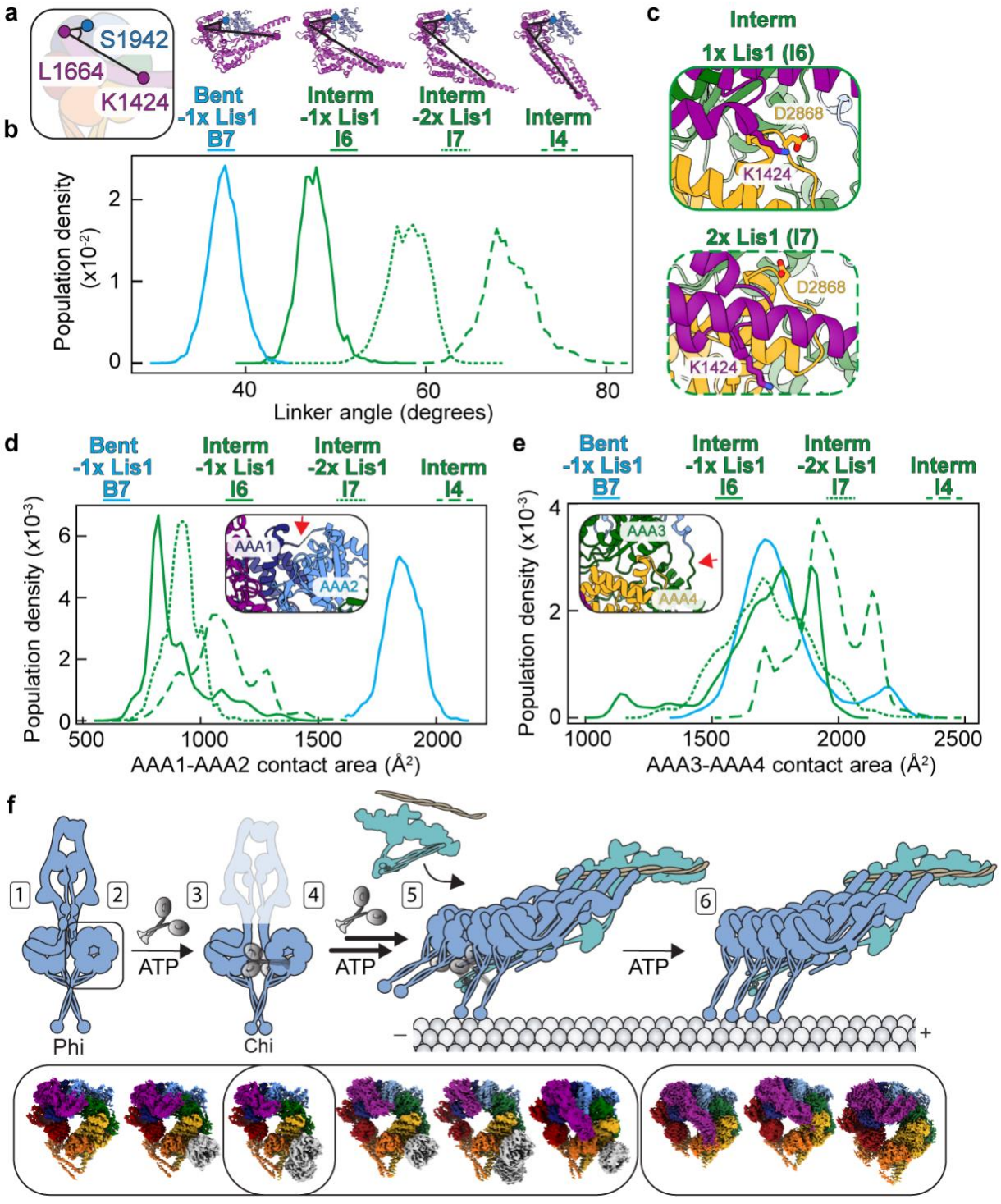
a
S1942
L1664
K1424
Bent
-1x Lis1
B7
Interm
-1x Lis1
I6
Interm
-2x Lis1
I7
Interm
I4
b
Population density
(x10-2)
Linker angle (degrees)
c
Interm
1x Lis1 (I6)
D2868
K1424
2x Lis1 (I7)
D2868
K1424
d
Population density (x10-3)
AAA1
AAA2
AAA1-AAA2 contact area (Å2)
e
Population density (x10-3)
AAA3
AAA4
AAA3-AAA4 contact area (Å2)
f
1
2
3
4
5
6
ATP
ATP
ATP
Phi
Chi
–
+

3.2 Discussion

Our work showed how heterogeneity mining in cryo-EM data, combined with time-resolved approaches, could identify a conformational landscape for dynein during its mechanochemical cycle and how this landscape is altered by Lis1 binding. The conformations identified in our study are in line with a recent similar analysis of full-length human dynein[12]. However, our work goes further, defining the contributions of Lis1 to dynein's mechanochemistry. Previous attempts at capturing different steps of dynein's mechanochemical cycle using X-ray crystallography were not fully comprehensive. Combining heterogeneity mining with time-resolved cryo-EM provides a unique advantage to visualize how ATP hydrolysis drives changes in dynein's conformational landscape over time.

We identified multiple conformations of dynein during ATP hydrolysis and determined the nucleotide state of each AAA module. Our different dynein and dynein/ Lis1 structures can be mapped onto the dynein activation pathway, starting with the bent linker dynein without Lis1. This conformation is consistent with individual dynein protomers in Phi (Fig. 3.6f (1)) and conformations that dynein samples while in the assembled complex moving along microtubules (Fig. 3.6f (6)). The bent linker dynein with one Lis1 β-propeller bound at $site_{ring}$ likely represents an early step in Chi particle formation (Fig. 3.6f (2)), followed by binding of the second Lis1 β-propeller at $site_{stalk}$ and full assembly of Chi (Fig. 3.6f (3)). We also identified a small population of particles in our datasets that corresponded to Chi dynein, containing two dyneins and two Lis1 dimers (published previously in[2]). Thus, our analysis is consistent with the idea that Lis1 binding to dynein and formation of Chi is an early step in dynein activation.

We propose a model in which Lis1 binding to dynein initially disrupts the autoinhibited Phi conformation by forming the Chi particle (Fig. 3.6f (3))[2]. Once bound, Lis1 allows dynein to

go through its mechanochemical cycle, which is seen as an increase in dynein's basal ATP hydrolysis rate (Fig. 3.6f (4), thicker arrow). This likely both disrupts Chi and allows dynein to adopt intermediate conformations (Fig. 3.6f (4)) compatible with complex assembly with dynactin and an activating adaptor (Fig. 3.6f (5)). Interestingly, we did not observe intermediate linker dynein by itself in any of our datasets collected in the presence of Lis1, even though we could solve structures of straight and bent linker dynein with and without Lis1 bound from those same datasets (Fig. 3.1g and Extended Data Fig. 3.4a and b). In addition, at the 30 min timepoint and in the presence of Lis1, the intermediate state dynein was the dominant one (Fig. 3.1h and Extended Data Fig. 3.5c). Although we cannot rule out that sample preparation somehow led to these distributions, this could mean that binding of Lis1 to dynein is particularly favorable in the intermediate state. Once the initial complex assembles and the first dynein dimer (Fig. 3.6f (5, Dyn-B)) binds to microtubules Lis1 bound to the second dynein dimer (Fig. 3.6f (5, Dyn-A)) may dissociate to allow for dynein's movement on microtubules, during which dynein samples multiple conformations (Fig. 3.6f (6)). It is also possible that Lis1 remains bound to active dynein given a recent study showing colocalization of moving dynein and Lis1 in neuronal cells[22]. The dynein conformations we observed in the absence of Lis1 likely represent the different steps of dynein's ATP hydrolysis-driven movement on microtubules (Fig. 3.6f (6)). Further structural work with full-length dynein, dynactin, an activating adaptor, and Lis1 in the presence of ATP will be required to fully map how dynein is activated.

We showed direct evidence that Lis1 stimulates dynein's basal ATP hydrolysis rate and suggest that this basal activity is inhibited when dynein is in the Phi conformation. In accordance with this, the D2868K mutation in dynein that prevents Phi formation increases dynein's basal ATPase rate. However, Lis1 stimulates dynein's ATPase activity further after the Phi particle is

disrupted. This suggests a two-step regulation mechanism. In the first step, Lis1 binds to dynein to open the Phi particle, which results in a higher rate of ATP hydrolysis as the conformational constraints imposed by Phi are released. Once Phi has been disrupted, Lis1 further increases dynein's ATPase rate by acting on the released motor, possibly by facilitating the release of ADP from AAA3. This could be driven by the decreased communication between the linker and dynein's motor domains, as suggested by our MD simulations. There, Lis1 binding to dynein in the intermediate state appeared to be influencing the ability of the linker to communicate with AAA4 (D2868) and the H2 loops in AAA2 (Fig. 3.5b). Further structural and mechanistic work will be required to fully decipher this mechanism.

3.3 Methods

Yeast strains construction

The *S. cerevisiae* strains used in this study are listed in Supplementary Table 3.1. The endogenous genomic copy of *PAC1* (encoding Lis1) or *DYN1* (encoding dynein) were deleted using PCR-based methods as previously described[23]. Point mutation to generate the D2868K dynein was introduced using QuikChange site-directed mutagenesis (Agilent) with the primers: 5'-CTTTAGGTCTTTTATTGAAGACAGAACAAGAACTG-3' and 5'-CAGTTCTTGTTCTGTCTTCAATAAAAGACCTAAAG-3' and verified by DNA sequencing. The mutated fragment was re-inserted into the kl*URA3* strains using the lithium acetate method[24] to reintroduce the mutated *DYN1* gene. Positive clones (kl*URA3*) were selected in the presence of 5-Fluorootic acid, screened by colony PCR, and verified by DNA sequencing.

Protein expression and purification

Protein purification steps were done at 4°C unless otherwise indicated. *S. cerevisiae* dynein constructs were purified from *S. cerevisiae* using a ZZ tag as previously described[25]. Briefly, liquid nitrogen-frozen yeast cell pellets were lysed by grinding in a chilled coffee grinder and resuspended in Dynein-lysis buffer supplemented with 0.5 mM Pefabloc, 0.05% Triton, and cOmplete EDTA-free protease inhibitor cocktail tablet (Roche). The lysate was clarified by centrifuging at 264,900 × *g* for 1 hr. The clarified supernatant was incubated with IgG Sepharose beads (GE Healthcare Life Sciences) for 1 hr. The beads were transferred to a gravity flow column, washed with Dynein-lysis buffer supplemented with 250 mM potassium chloride, 0.5 mM Pefabloc and 0.1% Triton, and with TEV buffer (10 mM Tris–HCl [pH 8.0], 150 mM potassium chloride, 10% glycerol, and 1 mM DTT). Dynein was cleaved from IgG beads via incubation with 0.15 mg/mL TEV protease (purified in house) overnight at 4°C. Cleaved dynein was concentrated using 100K MWCO concentrator (EMD Millipore), filtered by centrifuging with Ultrafree-MC VV filter (EMD Millipore) in a tabletop centrifuge and used fresh for cryo-EM sample preparation or snap-frozen in liquid nitrogen.

Yeast Lis1 was purified from *S. cerevisiae* using 8xHis and ZZ tags as previously described[15]. In brief, liquid-nitrogen frozen pellets were ground in a pre-chilled coffee grinder, resuspended in buffer A (50 mM potassium phosphate [pH 8.0], 150 mM potassium acetate, 150 mM sodium chloride, 2 mM magnesium acetate, 5 mM β-mercaptoethanol, 10% glycerol, 0.2% Triton, 0.5 mM Pefabloc) supplemented with 10 mM imidazole (pH 8.0) and cOmplete EDTA-free protease inhibitor cocktail tablet, and spun at 118,300 x g for 1h. The clarified supernatant was incubated with Ni-NTA agarose (QIAGEN) for 1 hr. The Ni beads were transferred to a gravity column, washed with buffer A + 20 mM imidazole (pH 8.0), and eluted with buffer A + 250 mM imidazole (pH 8.0). The eluted protein was incubated with IgG Sepharose beads for 1

hr. IgG beads were transferred to a gravity flow column, washed with buffer A + 20 mM imidazole (pH 8.0) and with modified TEV buffer (50 mM Tris–HCl [pH 8.0], 150 mM potassium acetate, 2 mM magnesium acetate, 1 mM EGTA, 10% glycerol, 1 mM DTT). Lis1 was cleaved from the IgG beads by the addition of 0.15 mg/mL TEV protease (purified in house) for 1 hr at 16°C. Cleaved proteins were filtered by centrifuging with Ultrafree-MC VV filter (EMD Millipore) in a tabletop centrifuge and flash frozen in liquid nitrogen.

Electron microscopy sample preparation

To remove any residual nucleotide, purified fresh dynein (not frozen) was incubated with apyrase for 30 mins (apyrase, 0.1 U/ml, NEB) prior to gel filtration on a Superose 6 Increase column pre-equilibrated in buffer containing 50 mM Tris, pH 8, 150 mM KCl, 2 mM EDTA, and 1 mM DTT. Eluted protein was concentrated to about 5 μM and diluted 1:1 with Lis1 or TEV buffer and incubated on ice for 10 mins prior to ATP addition (final concentrations: 2.5 μM dynein, 2.5 μM Lis1, and 1.25 mM ATP). Samples containing ATP were incubated for a total of 0.5 min or 30 min on ice (including blotting time and plunging) and quickly applied to plasma cleaned (Solarus, Gatan) UltrAuFoil Holey Gold R 1.2/1.3 μM3 grids (Quantifoil). A vitrobot (FEI) was used to blot away excess sample and plunge freeze the grids in liquid ethane. The Vitrobot chamber was maintained at 100% humidity and 4°C during the process. Grids were stored in liquid nitrogen until ready to be imaged. The 0.5 min grids were made and analyzed first. Based on observed conformational landscape in this condition, the 30 min time point was chosen for the longer time condition.

Electron microscopy image collection

The 0.5 min time point grids were imaged using Talos Arctica operated at 200 kV and equipped with K2 Summit direct electron detector (Gatan). Automated data collection was performed using Leginon. A total of 1849 movies over 3 sessions for the dynein + ATP – 0.5 min dataset and 12370 movies over 4 sessions for the dynein + Lis1 + ATP – 0.5 min dataset at 36,000 magnification (1.16 Å/pixel). The dose was ~6.3 $Å^{-2}s^{-}1$ with a total exposure time of 11 s divided into 200 ms-frames for a total of 40 frames. The defocus range was set to 0.8 – 2.4 μm.

The 30 min time point grids were imaged using an FEI Titan Krios (200 kV) equipped with a Flacon 4i detector and energy filter (<10 eV slit size) (Thermo Fisher). Total of 7182 movies for the dynein + ATP – 30 min dataset and 6670 movies for the dynein + Lis1 + ATP – 30 min dataset were collected using automated data acquisition (Thermo Fisher EPU) at 130,000 magnification (0.889 Å/pixel). The dose was ~5 $Å^{-2}s^{-}1$ with a total exposure time of 10 s divided into 200 ms-frames for a total of 40 frames. The defocus range was set to 0.75 – 2.8 μm.

Electron microscopy data processing

All movies were aligned in CryoSPRC live[26] using MotionCor2[27] of the dose-weighted frames. CTF was estimated in dose-weighted images using CTFFIND4[28]. Images with CTF fits worse than 5 Å were excluded from further processing. Particles were initially selected using blob finder in CryoSPRC and these peaks were used for Topaz[29] model training and final particle picking using Topaz. Particles were extracted and binned to 4.64 Å/pixel for the 0.5 min dataset and to 3.556 Å/pixel for the 30 min dataset. Multiple rounds of 2D classification with a varying number of online-EM interactions (30-40) and batch size per class between 200-400 dependent on the number of particles in each classification were carried out first in cryoSPARC to remove bad particles. Reconstructions were performed to generate initial models for each dataset with

particles from all good 2D classes. Good particles and models were selected for multiple rounds of 3D refinement and local refinements until no further improvement was observed and models appeared to contain well-defined secondary structures. Further analysis of heterogeneity was performed using 3D classification without alignment in Relion-3 to find subsets of particles that classified into models with well-defined secondary structures. These particles were then transferred to cryoSPARC for another round of Ab-initio reconstructions and 3D refinement.

CryoDRGN classification

To identify conformational and compositional variability, volumes from the non-uniform refinement in cryoSPARC were further subjected to cryoDRGN[30,31]. First, the particles were binned from 352 pixels to 128 pixels (3.19 or 2.45 Å/pixel final pixel size) and used for training an 8-dimensional latent variable model with 3 hidden layers and 128 nodes in the encoder and decoder networks. The latent space was visualized with the analyze function on epoch 50 and clusters were extracted using k-means analysis. The particles from the cluster that yielded the best 3D refinement were moved forward for one more round of training, with binning to 256 pixels (1.595 or 1.22 Å/pixel final pixel size) and training with 3 hidden layers and 1024 nodes in the networks. cryoDRGN landscape analysis was performed on the latent space and the structures representing the center of each cluster were manually inspected. Finally, good particles selected in cryoDRGN were extracted and transferred cryoSPARC for another round of Ab-initio reconstructions and 3D refinement.

Model building and refinement

Local refinement, CTF, and de-focus optimizations were used to improve the overall resolution of each map. The individual domains (AAA, AAA2, AAA3, AAA4, linker, and different stalk helices) from yeast dynein models PDB: 7MGM and 5VH9 were docked and rigidly fit into the different cryo-EM maps using UCSF Chimera X to build uniform models[32]. Subsequent rigid body and refinement were carried out using Phenix real space refine[33]. For all models the discrepancies between the model and map were fixed manually in COOT and then refined using a combination of Phenix real space refine and Rosetta Relax (v.13)[34,35]. For the 0.5 min dataset collected in the absence of Lis1 one model was built for the highest resolution density map (S1), given that the additional straight and intermediate state maps were derived from particles in S1 and were at a much lower resolution.

ATPase assays

ATPase assays were performed using EnzChek phosphate kit (Thermo Fisher) as previously described[25]. The proteins for the final reaction mixtures contained 20 nM dynein monomer or 20 nM dynein GST-dimer and Lis1 0-250 nM, 2 mM Mg-ATP, 200 mM MESG (2-amino-6-mercapto-7methyl purine ribose), 1 U/ml purine nucleoside phosphorylate, and assay buffer (30 mM HEPES pH 7.4, 50 mM KOAc, 2 mM MgOAc, 1 mM EGTA, 1 mM DTT). The final reaction signal was read at 360 nm every 10 sec for 10 min on a Biotek Citation 5 plate reader.

Molecular dynamics simulations

Four simulation systems were built based on the highest-resolution cryo-EM models obtained at 30-min time point (bent linker with 1x Lis1 bound – B7, intermediate linker with 2x

Lis1 bound – I7, intermediate linker with 1x Lis1 bound – I6, and intermediate linker with no Lis1 bound – I4). The linker region for each model was extended to start at residue 1354. For the intermediate linker dynein with 1x Lis1 bound – I6 and 2x Lis1 bound – I7, the linker position was determined from maps obtained from cryoDRGN heterogeneity analysis (Fig. 3.5c and Supplementary Fig. 3.2c; left panel for I6 and right panel for I7). Each model was solvated in a water box containing 150 mM NaCl. All the MD simulations were performed using the GPU-accelerated version of Amber18 with the ff14SB force field[36,37]. Energy minimization was conducted with the protein atoms' positions constrained by harmonic potentials with a spring constant of 10 kcal/(mol Å^2). With the same positional constraints, a following 40-ns equilibration simulation was performed at 300 K, gradually reducing the spring constant from 10 to 0.01 kcal/(mol Å^2). Langevin dynamics with a friction coefficient of 1 ps^{-1} was applied to maintain a constant temperature. Particle Mesh Ewald was used for full-system periodic electrostatics while a 9 Å cutoff was applied to Lennard-Jones interactions[38]. Bonds involving hydrogen atoms were constrained using the SHAKE algorithm[39]. Next, Gaussian Accelerated Molecular Dynamics (GaMD) was employed to enhance the sampling of protein conformational dynamics[40]. For each system, 20 independent runs were launched, each comprising a 40-ns conventional MD stage, a 20-ns GaMD equilibration stage, and a 100-ns GaMD production stage. The conventional MD stage was used to gather statistics for calculating initial GaMD acceleration parameters. During the GaMD stages, both total potential energy boost and dihedral energy boost were applied to the system, each with an upper limit of 4 kcal/mol for the standard deviation (for accurate reweighting). For each system, the accumulated GaMD trajectories analyzed totaled 2μs. The probability density distributions shown in Fig. 3.6 were obtained using the reweighting approach[41].

Statistical Analysis

Data was analyzed with Microsoft Excel and statistical tests were generated using GraphPad Prism 9. The exact value of n, evaluation of statistical significance, P values, and specific statistical analysis are described in the corresponding figures and figure legends.

Data availability

Cryo-EM maps and atomic coordinates have been deposited in the Electron Microscopy Data Bank under accession codes: S1 – EMD-46919, S2 – EMD-46897, S3 – EMD-46938, S4 – EMD-46953, I1 – EMD-47019, I2 – EMD-46958, I3 – EMD-46941, I4 – EMD-46954, I5 – EMD-46974, I6 – EMD-46972, I7 – EMD-46975, B1 – EMD-46935, B2 – EMD-46940, B3 – EMD-46942, B4 – EMD-46919, B5 – EMD-46959, B6 – EMD-47033, B7 – EMD-47026, B8 – EMD-47032 and in the Protein Data Bank under accession codes: S1 – 9DIU, S2 – 9DI3, S3 – 9DJU, S4 – 9DKD, I1 – 9DMW, I2 – 9DKH, I3 – 9DJZ, I4 – 9DKE, I5 – 9DLD, I6 – 9DKX, I7 – 9DLE, B1 – 9DKM, B2 – 9DJY, B3 – 9DK0, B4 – 9DJ7, B5 – 9DKJ, B6 – 9DNB, B7 – 9DN5, B8 – 9DN7. Unprocessed micrographs are deposited to EMPIAR. Source data for all graphs are provided with the manuscript.

3.4 Supplementary Figures

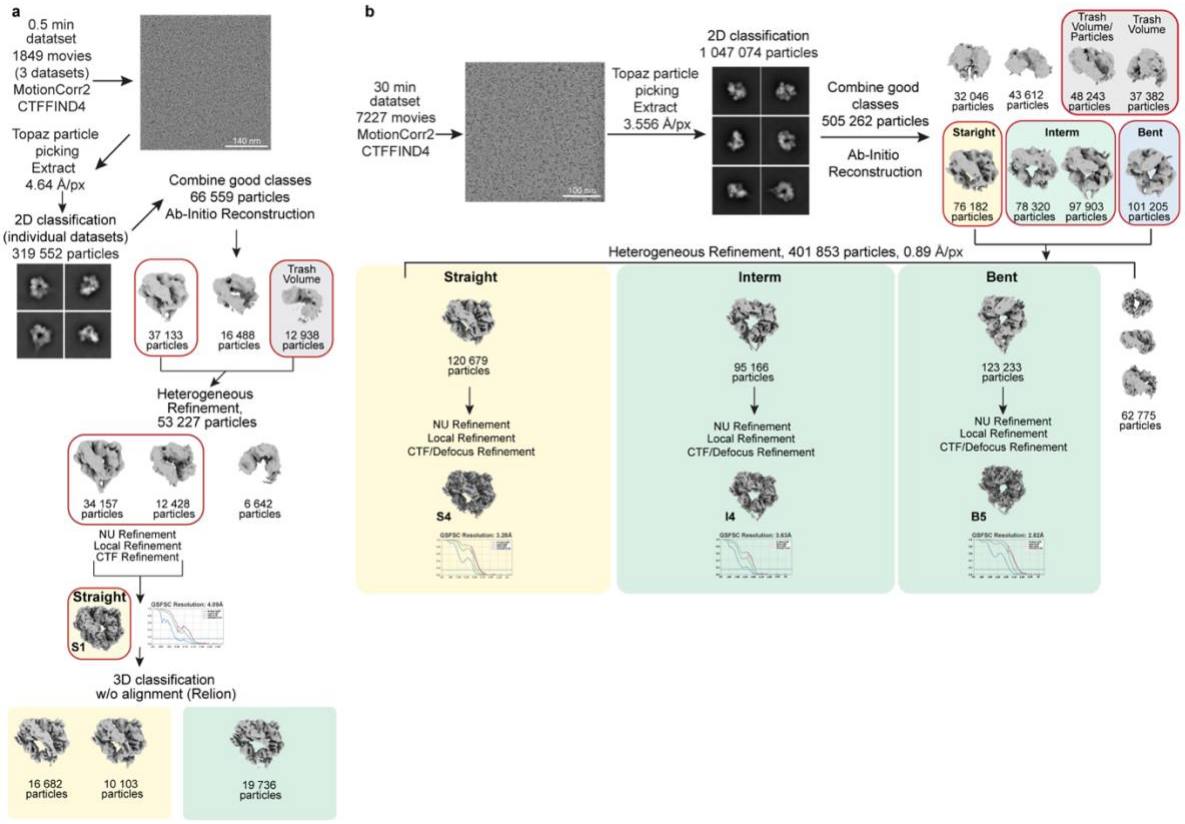

Supplementary Figure 3.1 Cryo-EM data processing workflow for the dynein + Lis1 datasets.

a. Dose-weighted movies from 3 datasets were aligned with MotionCor2 and CTF was estimated using CCTFFIND4. Particle extraction (binned by 4) was performed in cryoSPARC with a Topaz-trained model. Good particles from 2D classification jobs were used for ab-inito model generation in cryoSPARC. The models in red boxes were carried into the next steps. Fourier shell correlation (FSC) plots are shown next to the final maps. **b.** Dose-weighted movies from a dataset were aligned with MotionCor2 and CTF was estimated using CCTFFIND4. Particle extraction (binned by 4) was performed in cryoSPARC with a Topaz-trained model. Good particles from 2D classification jobs were used for ab-inito model generation in cryoSPARC. The models in red boxes were carried into the next steps. Fourier shell correlation (FSC) plots are shown next to the final maps.

Supplementary Figure 3.2 Cryo-EM data processing workflow for the dynein + Lis1 + ATP 0.5 min dataset.

a. Dose-weighted movies from 4 datasets were aligned with MotionCor2 and CTF was estimated using CCTFFIND4 Particle extraction (binned by 4) was performed in cryoSPARC with a Topaz-trained model. Good particles from 2D classification jobs were used for ab-inito model generation in cryoSPARC. The models in red boxes were carried into the next steps. Fourier shell correlation (FSC) plots are shown next to the final maps. **b.** The heterogeneity analysis (cryoDRGN) workflow with particles belonging to the intermediate linker dynein (I1) conformation. A UMAP visualization after analysis is shown and particles that show binding of two Lis1 β-propellers are grouped into the highlighted population (2x Lis1). **c.** The two maps used to determine the linker position for the intermediate linker dynein with 1x Lis1 bound (left) and 2x Lis1 bound (right).

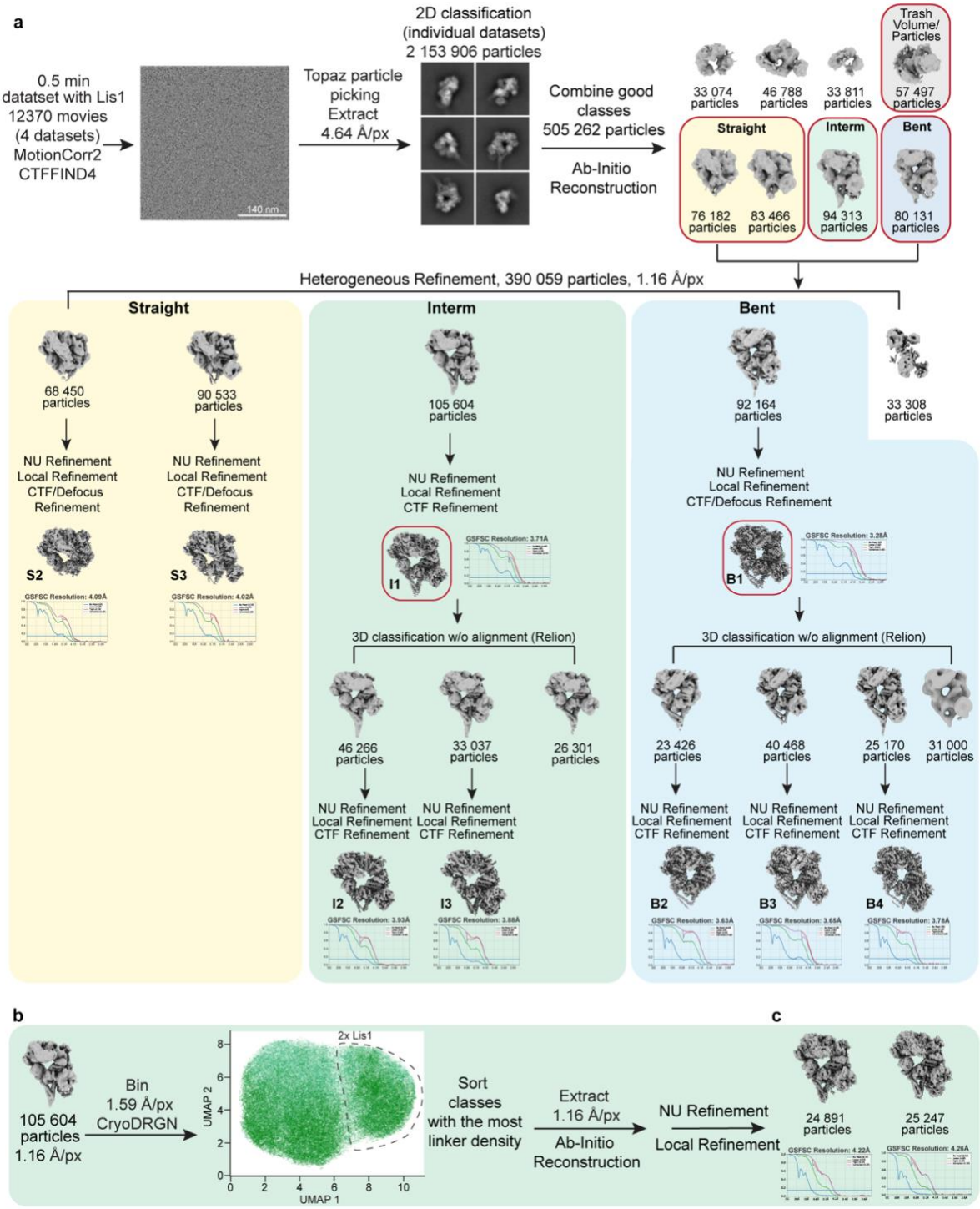
a
0.5 min datatset with Lis1
12370 movies
(4 datasets)
MotionCorr2
CTFFIND4
140 nm
Topaz particle picking
Extract
4.64 Å/px
2D classification
(individual datasets)
2 153 906 particles
Combine good classes
505 262 particles
Ab-Initio Reconstruction
33 074 particles
46 788 particles
33 811 particles
Trash Volume/ Particles
57 497 particles
Straight
Interm
Bent
76 182 particles
83 466 particles
94 313 particles
80 131 particles
Heterogeneous Refinement, 390 059 particles, 1.16 Å/px
Straight
68 450 particles
90 533 particles
NU Refinement
Local Refinement
CTF/Defocus Refinement
S2
S3
GSFSC Resolution: 4.09Å
GSFSC Resolution: 4.02Å
Interm
105 604 particles
NU Refinement
Local Refinement
CTF Refinement
I1
GSFSC Resolution: 3.71Å
3D classification w/o alignment (Relion)
46 266 particles
33 037 particles
26 301 particles
NU Refinement
Local Refinement
CTF Refinement
I2
I3
GSFSC Resolution: 3.93Å
GSFSC Resolution: 3.88Å
Bent
92 164 particles
33 308 particles
NU Refinement
Local Refinement
CTF/Defocus Refinement
B1
GSFSC Resolution: 3.28Å
3D classification w/o alignment (Relion)
23 426 particles
40 468 particles
25 170 particles
31 000 particles
NU Refinement
Local Refinement
CTF Refinement
B2
B3
B4
GSFSC Resolution: 3.63Å
GSFSC Resolution: 3.66Å
GSFSC Resolution: 3.78Å
b
105 604 particles 1.16 Å/px
Bin 1.59 Å/px CryoDRGN
2x Lis1
UMAP 2
UMAP 1
Sort classes with the most linker density
Extract 1.16 Å/px
Ab-Initio Reconstruction
NU Refinement
Local Refinement
c
24 891 particles
25 247 particles
GSFSC Resolution: 4.22Å
GSFSC Resolution: 4.26Å

Supplementary Figure 3.3 Cryo-EM data processing workflow for the dynein + Lis1 + ATP 30 min dataset.

Dose-weighted movies from a dataset were aligned with MotionCor2 and CTF was estimated using CCTFFIND4. Particle extraction (binned by 4) was performed in cryoSPARC with a Topaz-trained model. Good particles from 2D classification jobs were used for ab-inito model generation in cryoSPARC. The models in red boxes were carried into the next steps. Fourier shell correlation (FSC) plots are shown next to the final maps.

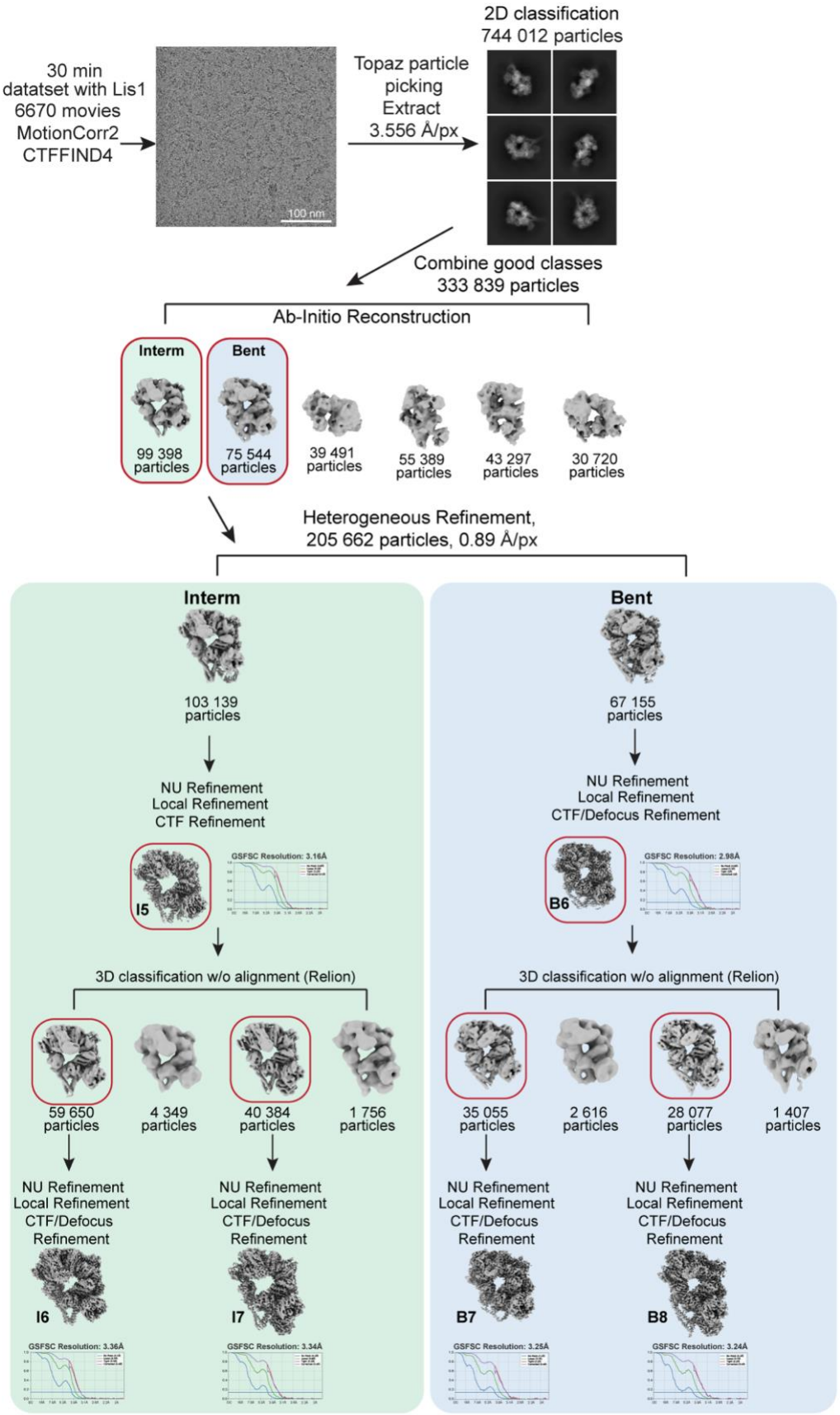
30 min
datatset with Lis1
6670 movies
MotionCorr2
CTFFIND4
100 nm
Topaz particle
picking
Extract
3.556 Å/px
2D classification
744 012 particles
Combine good classes
333 839 particles
Ab-Initio Reconstruction
Interm
Bent
99 398
particles
75 544
particles
39 491
particles
55 389
particles
43 297
particles
30 720
particles
Heterogeneous Refinement,
205 662 particles, 0.89 Å/px
Interm
103 139
particles
NU Refinement
Local Refinement
CTF Refinement
I5
GSFSC Resolution: 3.16Å
3D classification w/o alignment (Relion)
59 650
particles
4 349
particles
40 384
particles
1 756
particles
NU Refinement
Local Refinement
CTF/Defocus
Refinement
I6
GSFSC Resolution: 3.36Å
NU Refinement
Local Refinement
CTF/Defocus
Refinement
I7
GSFSC Resolution: 3.34Å
Bent
67 155
particles
NU Refinement
Local Refinement
CTF/Defocus Refinement
B6
GSFSC Resolution: 2.98Å
3D classification w/o alignment (Relion)
35 055
particles
2 616
particles
28 077
particles
1 407
particles
NU Refinement
Local Refinement
CTF/Defocus
Refinement
B7
GSFSC Resolution: 3.25Å
NU Refinement
Local Refinement
CTF/Defocus
Refinement
B8
GSFSC Resolution: 3.24Å

Supplementary Figure 3.4 Local resolution and nucleotide occupancies at AAA+ subunits.

Local resolution and views of the nucleotide-binding pockets for the indicated AAA+ subunits for **a.** straight (S), **b.** intermediate (I), and **c.** bent (B) linker dynein. Conformations belonging to each category are named with the first letter of that category and are shown in order starting with states identified in the shorter time point (0.5 min, white background) followed by the longer time point (30 min, gray background).

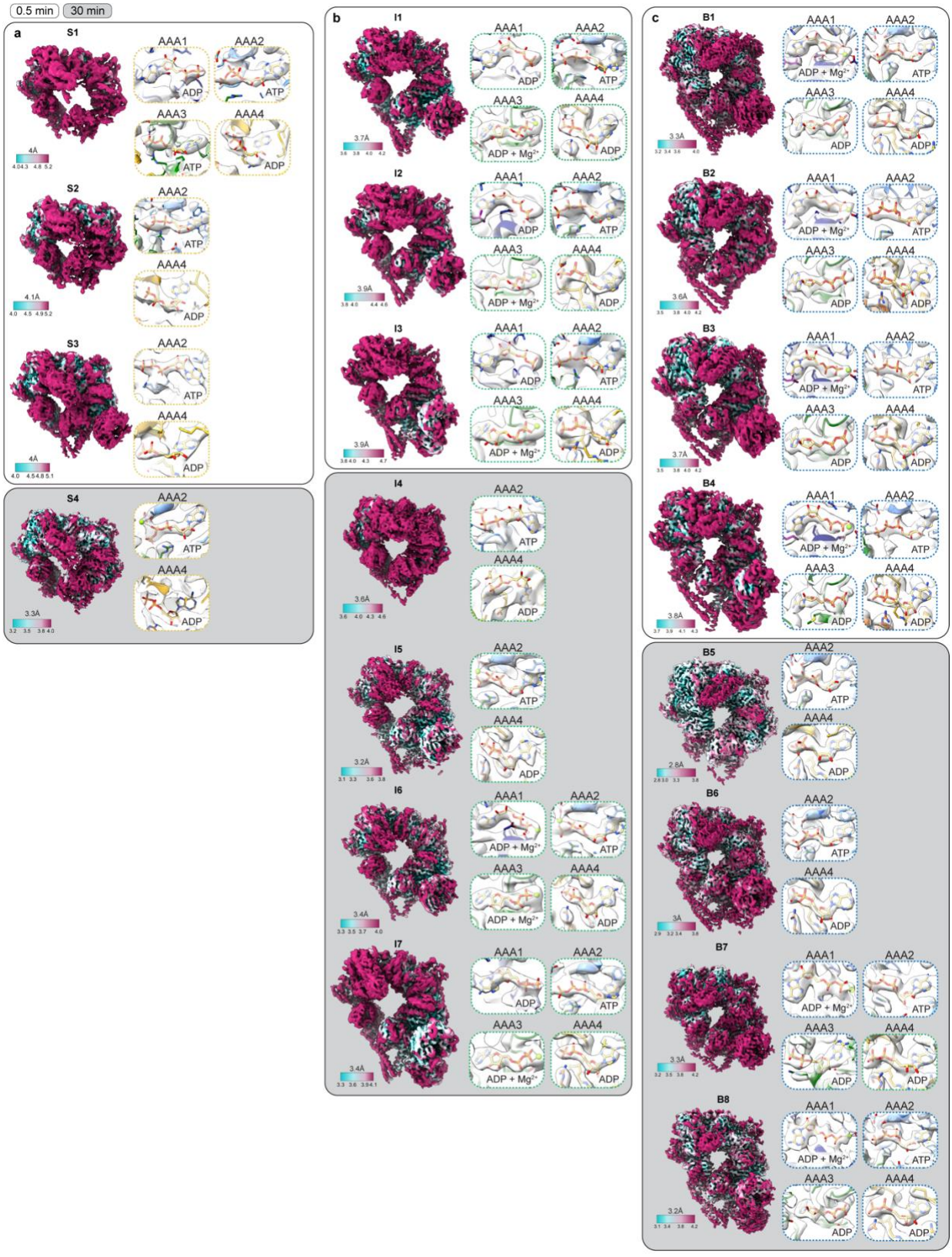
0.5 min
30 min
a
S1
AAA1
AAA2
ADP
ATP
AAA3
AAA4
ATP
ADP
4Å
S2
AAA2
ATP
AAA4
ADP
4.1Å
S3
AAA2
ATP
AAA4
ADP
4Å
S4
AAA2
ATP
AAA4
ADP
3.3Å
b
I1
AAA1
AAA2
ADP
ATP
AAA3
AAA4
ADP + Mg2+
ADP
3.7Å
I2
AAA1
AAA2
ADP
ATP
AAA3
AAA4
ADP + Mg2+
ADP
3.9Å
I3
AAA1
AAA2
ADP
ATP
AAA3
AAA4
ADP + Mg2+
ADP
3.9Å
I4
AAA2
ATP
AAA4
ADP
3.6Å
I5
AAA2
ATP
AAA4
ADP
3.2Å
I6
AAA1
AAA2
ADP + Mg2+
ATP
AAA3
AAA4
ADP + Mg2+
ADP
3.4Å
I7
AAA1
AAA2
ADP
ATP
AAA3
AAA4
ADP + Mg2+
ADP
3.4Å
c
B1
AAA1
AAA2
ADP + Mg2+
ATP
AAA3
AAA4
ADP
ADP
3.3Å
B2
AAA1
AAA2
ADP + Mg2+
ATP
AAA3
AAA4
ADP
ADP
3.6Å
B3
AAA1
AAA2
ADP + Mg2+
ATP
AAA3
AAA4
ADP
ADP
3.7Å
B4
AAA1
AAA2
ADP + Mg2+
ATP
AAA3
AAA4
ADP
ADP
3.8Å
B5
AAA2
ATP
AAA4
ADP
2.8Å
B6
AAA2
ATP
AAA4
ADP
3Å
B7
AAA1
AAA2
ADP + Mg2+
ATP
AAA3
AAA4
ADP
ADP
3.3Å
B8
AAA1
AAA2
ADP + Mg2+
ATP
AAA3
AAA4
ADP
ADP
3.2Å

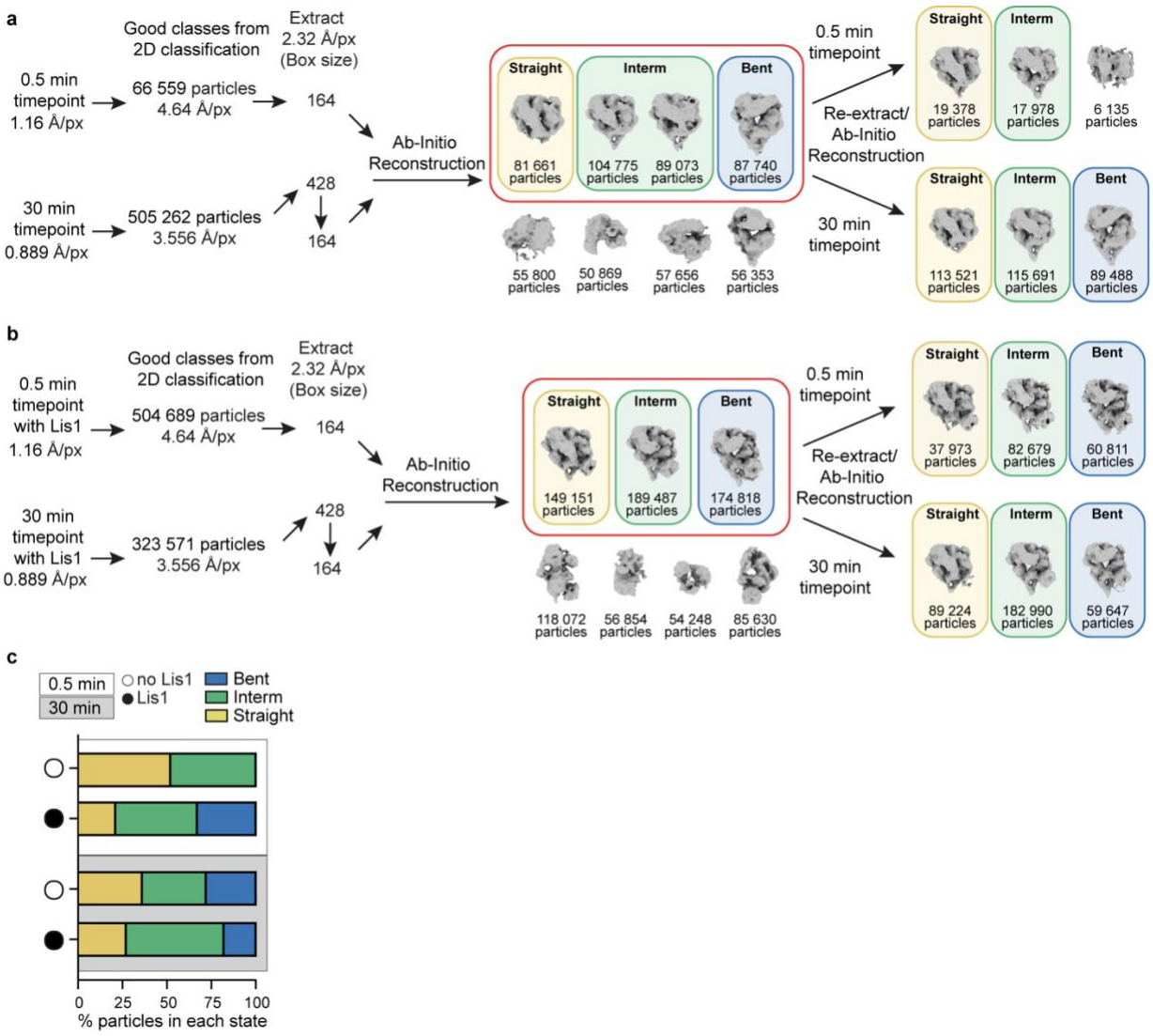

Supplementary Figure 3.5 Cryo-EM data processing of the combined datasets.

a. and **b**. Cryo-EM data processing workflow for the combined datasets. **c.** Relative abundance of particles belonging to different states obtained from particle distributions in cryo-EM datasets in the absence (open circle) or presence (black circle) of Lis1 at two different time points (0.5 min – white background and 30 min – gray background).

Supplementary Figure 3.6 Summary of the identified structures and their properties.

Summary of the cryo-EM volumes determined in this work, with their properties, for the indicated datasets. Stalk represents the identified stalk conformations48. S – straight linker conformation, yellow background; I – intermediate linker conformation, green background; and B – bent linker conformation, blue background.

a Dynein + ATP (0.5 min and 30 min)

● ATP
◔ ADP + Mg^{2+}
○ ADP

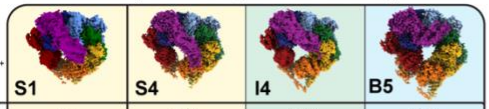

	S1	S4	I4	B5
resol. (Å)	4.1	3.3	3.6	2.8
Lis1	n/a	n/a	n/a	n/a
ring	open	open	interm	closed
linker	straight	straight	interm	bent
AAA1	○	○	○	◔
AAA2	●	●	●	●
AAA3	○	◔	◔	◔
AAA4	○	○	○	○
Stalk	α	α	semi-α	β
Sample	Dynein	Dynein	Dynein	Dynein
Time point	0.5 min	30 min	30 min	30 min

b Dynein + Lis1 + ATP (0.5 min)

● ATP
◔ ADP + Mg^{2+}
○ ADP

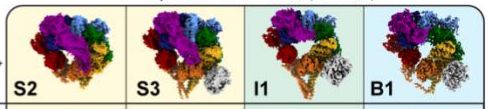

	S2	S3	I1	B1
resol. (Å)	4.0	4.0	3.7	3.3
Lis1	0	1	1-2	1-2
ring	open	open	interm	closed
linker	straight	straight	interm	bent
AAA1	○	○	○	◔
AAA2	●	●	●	●
AAA3	○	○	◔	○
AAA4	○	○	○	○
Stalk	α	α	semi-α	β
Sample	Dynein/Lis1	Dynein/Lis1	Dynein/Lis1	Dynein/Lis1
Time point	0.5 min	0.5 min	0.5 min	0.5 min

c Dynein + Lis1 + ATP (30 min)

● ATP
◔ ADP + Mg^{2+}
○ ADP

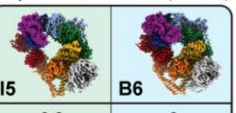

	I5	B6
resol. (Å)	3.2	3
Lis1	1-2	1-2
ring	interm	closed
linker	interm	bent
AAA1	◔	◔
AAA2	●	●
AAA3	◔	○
AAA4	○	○
Stalk	semi-α	low
Sample	Dynein/Lis1	Dynein/Lis1
Time point	30 min	30 min

d Dynein + Lis1 + ATP (0.5 min)
After 3D classification

● ATP
◔ ADP + Mg^{2+}
○ ADP

	I2	I3	B2	B3	B4
resol. (Å)	3.9	3.9	3.6	3.6	3.8
Lis1	1	0	0	1	2
ring	interm	interm	closed	closed	closed
linker	interm	interm	bent	bent	bent
AAA1	○	○	◔	◔	◔
AAA2	●	●	●	●	●
AAA3	◔	◔	○	○	○
AAA4	○	○	○	○	○
Stalk	semi-α	semi-α	β	β	β
Sample	Dynein/Lis1	Dynein/Lis1	Dynein/Lis1	Dynein/Lis1	Dynein/Lis1
Time point	0.5 min	0.5 min	0.5 min	0.5 min	0.5 min

e Dynein + Lis1 + ATP (30 min)
After 3D classification

● ATP
◔ ADP + Mg^{2+}
○ ADP

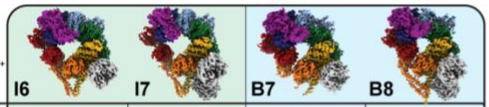

	I6	I7	B7	B8
resol. (Å)	3.4	3.4	3.3	3.2
Lis1	1	1	1	2
ring	interm	interm	closed	closed
linker	interm	interm	bent	bent
AAA1	◔	○	◔	◔
AAA2	●	●	●	●
AAA3	◔	◔	○	○
AAA4	○	○	○	○
Stalk	semi-α	semi-α	β	β
Sample	Dynein/Lis1	Dynein/Lis1	Dynein/Lis1	Dynein/Lis1
Time point	30 min	30 min	30 min	30 min

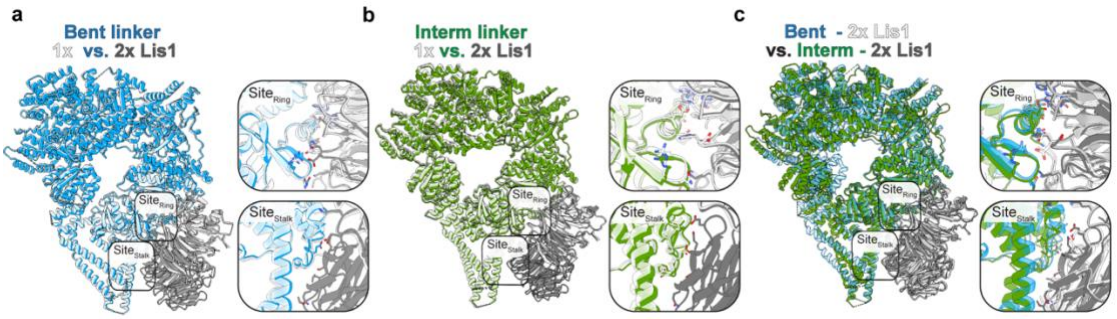

Supplementary Figure 3.7 Specifics of Lis1 interaction with dynein.

a. Comparison of models build for bent linker dynein bound to 2 Lis1 β-propellers (B8, blue, Lis1 – gray) with bent linker dynein bound to 1 Lis1 β- propellers (B7, white, Lis1 – white). The two Lis1 binding sites are highlighted and shown to the right. **b.** Comparison of models build for intermediate linker dynein bound to 2 Lis1 β-propellers (I7, green, Lis1 – gray) with intermediate linker dynein bound to 1 Lis1 β-propellers (I6, white, Lis1 – white). The two Lis1 binding sites are highlighted and shown to the right. **c.** Comparison of models build for bent linker dynein bound to 2 Lis1 β-propellers (B8, blue, Lis1 – white) with intermediate linker dynein bound to 2 Lis1 β-propellers (I7, green, Lis1 – white). The two Lis1 binding sites are highlighted and shown to the right.

3.5 Tables

Table 3.1 Cryo-EM data information and model validation statistics for the 0.5 min datasets. CryoEM data collection parameters, reconstruction information, and model refinement statistics.

Name	**S1-J1962**	**S2-J1579**	**S3-J1705**	**I1-J1689**	**I2-J1690**	**I3-J1691**	**B1-J1807**	**B2-J1760**	**B3-J1761**	**B4-J1762**
State	Straight	Straight	Straight /Lis1	Interm. /Lis1	Interm. /1xLis1	Interm. /2xLis1	Bent	Bent	Bent /1xLis1	Bent /2xLis1
Condition (Lis1)	n/a	Lis1	Lis1	Lis1	Lis1	Lis1	Lis1	Lis1	Lis1	Lis1
Time point (min)	0.5	0.5	0.5	0.5	0.5	0.5	0.5	0.5	0.5	0.5
EMD-	46919	46897	46938	47019	46958	46941	46935	46940	46942	46919
PDB-	9DIU	9DI3	9DJU	9DMW	9DKH	9DJZ	9DKM	9DJY	9DK0	9DJ7
Data collection and processing										
Magnification	36 000									
Voltage (kV)	200									
Electron exposure (e–/Å^2)	Dataset #1 – 54 Dataset #2 – 54 Dataset #3 – 55	Dataset #1 – 53 Dataset #2 – 54 Dataset #3 – 54 Dataset #4 – 51								
Defocus range (μm)	0.8 – 2.4									
Pixel size (Å)	1.16									
Symmetry imposed	C1									
Images (no.)	1 849	12 370								
Initial particles (no.)	319 552	1 047 074								
Final particles (no.)	46 585	68 450	68 486	105 604	46 266	33 037	92 164	23 426	40 468	25 170
Map resolution (Å) (FSC 0.143)	4	4.1	4	3.7	3.9	3.9	3.3	3.6	3.7	3.8
Refinement										
Initial model used (PDB code)	7MGM	7MGM	7MGM	7MGM	7MGM	7MGM	7MGM	7MGM	7MGM	7MGM
Model resolution (Å) (FSC 0.5)	4.5	4.3	4.4	4	4.2	4.2	3.4	3.9	3.9	4
Map sharpening *B* factor (Å^2)	86.5	106	109.8	97.4	85.1	67.4	83.9	63	72.6	60.8
Model composition										
Non-hydrogen atoms	17 847	17 694	20 676	21 212	21 004	23 913	21 339	18 424	21 050	23 851
Protein residues	2302	2 282	2 643	2 729	2691	3047	2 748	2 341	2 690	3026
Ligands	ADP:3, ATP:1	ADP:3, ATP:1	ADP:3, ATP:1	MG:1, ADP:3, ATP:1	MG:1, ADP:3, ATP:1	MG:1, ADP:3, ATP:1	MG:1, ADP:3, ATP:1	MG:1, ADP:3, ATP:1	MG:1, ADP:3, ATP:1	MG:1, ADP:3, ATP:1
***B* factors (Å^2)**										
Protein	166.53	124.09	140.15	69.90	107.18	141.67	54.14	98.06	71.21	94.99
Ligand	162.06	92.88	70.03	43.58	69.38	118.25	25.38	80.48	46.11	76.40

Table 3.2 Cryo-EM data information and model validation statistics for the 0.5 min datasets. CryoEM data collection parameters, reconstruction information, and model refinement statistics. (Continued)

R.m.s. deviations										
Bond lengths (Å)	0.003	0.004	0.003	0.003	0.003	0.003	0.003	0.003	0.003	0.003
Bond angles (°)	0.715	0.680	0.740	0.701	0.647	0.616	0.562	0.585	0.602	0.613
Validation										
MolProbity score	1.51	1.75	1.68	1.40	1.52	1.55	1.37	1.30	1.44	1.51
Clashscore	7.75	9.34	8.46	5.16	6.31	7.23	4.93	4.81	5.96	6.48
Poor rotamers (%)	0.3	0.2	0.5	0.1	0	0.1	0.1	0.1	0.1	0.2
Ramachandran plot										
Favored (%)	97.60	96.19	96.55	97.35	97.04	97.18	97.45	97.75	97.41	97.15
Allowed (%)	2.4	3.81	3.45	2.65	2.96	2.82	2.55	2.25	2.59	2.85
Disallowed (%)	0	0	0	0	0	0	0	0	0	0

Table 3.3 Cryo-EM data information and model validation statistics for the 30 min datasets. CryoEM data collection parameters, reconstruction information, and model refinement statistics.

Name	**S4-J2127**	**I4-J2126**	**B5-J2128**	**I5-J2192**	**I6-J2513**	**I7-J2520**	**B6-J2190**	**B7-J2527**	**B8-J2534**
State	Straight	Interm	Bent	Interm /Lis1	Interm /1xLis1	Interm /2xLis1	Bent /Lis1	Bent /1xLis1	Bent /2xLis1
Condition (Lis1)	n/a	n/a	n/a	Lis1	Lis1	Lis1	Lis1	Lis1	Lis1
Time point (min)	30	30	30	30	30	30	30	30	30
EMD-	46953	46954	46959	46974	46972	46975	47033	47026	47032
PDB-	9DKD	9DKE	9DKJ	9DLD	9DKX	9DLE	9DNB	9DN5	9DN7
Data collection and processing									
Magnification	150 000								
Voltage (kV)	200								
Electron exposure (e–/Å^2)	54			54					
Defocus range (μm)	0.75 – 2.8								
Pixel size (Å)	0.889								
Symmetry imposed	C1								
Images (no.)	7 227			6 670					
Initial particles (no.)	1 047 074			744 012					
Final particles (no.)	119 768	94 448	122 388	106 139	59 650	40 384	67 155	35 055	28 077
Map resolution (Å) (FSC 0.143)	3.3	3.6	2.8	3.2	3.4	3.4	3	3.3	3.25
Refinement									
Initial model used (PDB code)	7MGM	7MGM	7MGM	7MGM	7MGM	7MGM	7MGM	7MGM	7MGM
Model resolution (Å) (FSC 0.5)	3.6	4.2	3.0	3.4	3.7	3.7	3.3	3.7	3.5
Map sharpening *B* factor (Å^2)	82.3	74.3	71.2	77.2	70.1	56.5	57.1	55.1	51.8
Model composition									
Non-hydrogen atoms	17 901	17 457	18 075	22 996	20 808	22 893	22 963	21000	23772
Protein residues	2 313	2 291	2 291	3 017	2646	2985	3020	2679	3021
Ligands	MG:1, ADP:3, ATP:1	MG:1, ADP:3, ATP:1	MG:2, ADP:3, ATP:1	MG:3, ADP:3, ATP:1	MG:3, ADP:3, ATP:1	MG:2, ADP:3, ATP:1	MG:1, ADP:3, ATP:1	MG:1, ADP:3, ATP:1	MG:1, ADP:3, ATP:1
***B* factors (Å^2)**									
Protein	67.01	123.03	66.14	96.14	106.31	108.74	69.30	99.61	84.55
Ligand	30.25	86.62	39.03	55.26	69.26	71.52	32.12	69.54	62.99

Table 3.4 Cryo-EM data information and model validation statistics for the 30 min datasets. CryoEM data collection parameters, reconstruction information, and model refinement statistics. (Continued)

R.m.s. deviations									
Bond lengths (Å)	0.003	0.003	0.003	0.003	0.003	0.003	0.002	0.003	0.003
Bond angles (°)	0.655	0.715	0.628	0.597	0.621	0.600	0.521	0.623	0.579
Validation									
MolProbity score	1.50	1.43	1.19	1.48	1.46	1.49	1.37	1.35	1.52
Clashscore	7.00	6.2	4.06	6.19	5.41	5.76	6.71	6.43	6.17
Poor rotamers (%)	0.1	0.1	0.1	0.1	0.1	0.2	0	0	0
Ramachandran plot									
Favored (%)	97.44	97.58	98.01	97.27	97.05	97.01	98.25	98.49	96.91
Allowed (%)	2.56	2.42	1.99	2.73	2.95	2.99	1.75	1.51	3.09
Disallowed (%)	0	0	0	0	0	0	0	0	0

3.6 Supplementary Tables

Supplementary Table 3.1 S. cerevisiae strains used in this study. DHA and SNAP refer to the HaloTag (Promega) and SNAP-tag (NEB), respectively. TEV indicates a Tev protease cleavage site. PGAL1 denotes the galactose promoter, which was used for inducing strong expression of Lis1 and dynein motor domain constructs. Amino acid spacers are indicated by gs (glycine-serine).

Strain	Genotype	Source
RPY1	W303a (*MATa; his3-11,15; ura3-1; leu2-3,112; ade2-1; trp1-1*)	(Eshel et al., 1993)
RPY753	W303a; *pep4Δ::HIS5; prb1Δ; P_{GAL1}-ZZ-Tev-GFP-3HA-GST-DYN1$_{331kDa}$-gs-DHA; pac1Δ::URA3; ndl1Δ::CgLEU2*	(Huang et al., 2012)
RPY816	W303a; *pep4Δ::HIS5; prb1Δ; P_{GAL1}-8HIS-ZZ-Tev-PAC1; dyn1Δ::CgLEU2; ndl1Δ:: Hy-groR*	(Huang et al., 2012)
RPY1302	W303a; *pep4Δ::HIS5; prb1Δ; PAC11-13xMYC-TRP1, P_{GAL1}-ZZ-Tev-DYN1$_{331kDa}$; pac1Δ:: HygroR*	(Toropova et al., 2014)
RPY1547	W303a; *pep4Δ::HIS5; prb1Δ; P_{GAL1}-8HIS-ZZ-Tev-PAC1$_{R275A,R301A,R378A,W419A,K437A}$; dyn1Δ::CgLEU2; ndl1Δ:: HygroR*	(Toropova et al., 2014)
RPY1882	W303a; *pep4Δ::HIS5; prb1Δ; P_{GAL1}-ZZ-Tev-GFP-3HA-GST-DYN1$_{331kDa}$-gs-DHA; pac1Δ::URA3; ndl1Δ::CgLEU2*	This work

3.7 References

1. Gillies JP, Reimer JM, Karasmanis EP, Lahiri I, Htet ZM, Leschziner AE, Reck-Peterson SL. Structural basis for cytoplasmic dynein-1 regulation by Lis1. *eLife* **11**, e71229 (2022).
2. Karasmanis EP, Reimer JM, Kendrick AA, Nguyen KHV, Rodriguez JA, Truong JB, Lahiri I, Reck-Peterson SL, Leschziner AE. Lis1 relieves cytoplasmic dynein-1 autoinhibition by acting as a molecular wedge. *Nat. Struct. Mol. Biol.* **30**, 1357–1364 (2023).
3. DeSantis ME, Cianfrocco MA, Htet ZM, Tran PT, Reck-Peterson SL, Leschziner AE. Lis1 Has Two Opposing Modes of Regulating Cytoplasmic Dynein. *Cell* **170**, 1197-1208.e12 (2017).
4. Reimer, J. M., DeSantis, M. E., Reck-Peterson, S. L. & Leschziner, A. E. Structures of human dynein in complex with the lissencephaly 1 protein, LIS1. *eLife* **12**, e84302 (2023).
5. Coureux, P., Sweeney, H. L. & Houdusse, A. Three myosin V structures delineate essential features of chemo-mechanical transduction. *EMBO J.* **23**, 4527–4537 (2004).
6. Rosenfeld, S. S., Houdusse, A. & Sweeney, H. L. Magnesium Regulates ADP Dissociation from Myosin V *. *J. Biol. Chem.* **280**, 6072–6079 (2005).
7. Schmidt, H., Zalyte, R., Urnavicius, L. & Carter, A. P. Structure of human cytoplasmic dynein-2 primed for its power stroke. *Nature* **518**, 435–438 (2015).
8. Rao, L., Berger, F., Nicholas, M. P. & Gennerich, A. Molecular mechanism of cytoplasmic dynein tension sensing. *Nat. Commun.* **10**, 3332 (2019).
9. Nishida N, Komori Y, Takarada O, Watanabe A, Tamura S, Kubo S, Shimada I, Kikkawa M. Structural basis for two-way communication between dynein and microtubules. *Nat. Commun.* **11**, 1038 (2020).
10. Golcuk, M., Yilmaz, S. Z., Yildiz, A. & Gur, M. The mechanism and energetics of the dynein priming stroke. *Structure* **32**, 603-610.e4 (2024).
11. Bhabha G, Cheng HC, Zhang N, Moeller A, Liao M, Speir JA, Cheng Y, Vale RD. Allosteric Communication in the Dynein Motor Domain. *Cell* **159**, 857–868 (2014).
12. Chai P, Yang J, Geohring IC, Markus SM, Wang Y, Zhang K. The mechanochemical cycle of reactive full-length human dynein 1. *Nat Struct Mol Biol* (2025).
13. Kon, T., Mogami, T., Ohkura, R., Nishiura, M. & Sutoh, K. ATP hydrolysis cycle–dependent tail motions in cytoplasmic dynein. *Nat. Struct. Mol. Biol.* **12**, 513–519 (2005).
14. Toropova K, Zou S, Roberts AJ, Redwine WB, Goodman BS, Reck-Peterson SL, Leschziner AE. Lis1 regulates dynein by sterically blocking its mechanochemical cycle. *eLife* **3**, e03372 (2014).
15. Huang, J., Roberts, A. J., Leschziner, A. E. & Reck-Peterson, S. L. Lis1 Acts as a "Clutch" between the ATPase and Microtubule-Binding Domains of the Dynein Motor. *Cell* **150**, 975–986 (2012).
16. Yamada M, Toba S, Yoshida Y, Haratani K, Mori D, Yano Y, Mimori-Kiyosue Y, Nakamura T, Itoh K, Fushiki S, Setou M, Wynshaw-Boris A, Torisawa T, Toyoshima YY, Hirotsune S. LIS1 and NDEL1 coordinate the plus-end-directed transport of cytoplasmic dynein. *EMBO J.* **27**, 2471–2483 (2008).
17. Htet ZM, Gillies JP, Baker RW, Leschziner AE, DeSantis ME, Reck-Peterson SL. LIS1 promotes the formation of activated cytoplasmic dynein-1 complexes. *Nat. Cell Biol.* **22**, 518–525 (2020).
18. Kon T, Oyama T, Shimo-Kon R, Imamula K, Shima T, Sutoh K, Kurisu G. The 2.8 Å crystal structure of the dynein motor domain. *Nature* **484**, 345–350 (2012).
19. Roberts AJ, Numata N, Walker ML, Kato YS, Malkova B, Kon T, Ohkura R, Arisaka F, Knight PJ, Sutoh K, Burgess SA. AAA+ Ring and Linker Swing Mechanism in the Dynein Motor. *Cell* **136**, 485–495 (2009).
20. Zhang K, Foster HE, Rondelet A, Lacey SE, Bahi-Buisson N, Bird AW, Carter AP. Cryo-EM Reveals How Human Cytoplasmic Dynein Is Auto-inhibited and Activated. *Cell* **169**, 1303-1314.e18 (2017).
21. Marzo, M. G., Griswold, J. M. & Markus, S. M. Pac1/LIS1 stabilizes an uninhibited conformation of dynein to coordinate its localization and activity. *Nat. Cell Biol.* **22**, 559–569 (2020).
22. Fellows, A. D., Bruntraeger, M., Burgold, T., Bassett, A. R. & Carter, A. P. Dynein and dynactin move long-range but are delivered separately to the axon tip. *J. Cell Biol.* **223**, e202309084 (2024).
23. Longtine MS, McKenzie A 3rd, Demarini DJ, Shah NG, Wach A, Brachat A, Philippsen P, Pringle JR. Additional modules for versatile and economical PCR-based gene deletion and modification in Saccharomyces cerevisiae. *Yeast* **14**, 953–961 (1998).
24. Gietz, R. D. & Schiestl, R. H. High-efficiency yeast transformation using the LiAc/SS carrier DNA/PEG method. *Nat. Protoc.* **2**, 31–34 (2007).
25. Reck-Peterson SL, Yildiz A, Carter AP, Gennerich A, Zhang N, Vale RD. Single-Molecule Analysis of Dynein Processivity and Stepping Behavior. *Cell* **126**, 335–348 (2006).

26. Punjani, A., Rubinstein, J. L., Fleet, D. J. & Brubaker, M. A. cryoSPARC: algorithms for rapid unsupervised cryo-EM structure determination. *Nat. Methods* **14**, 290–296 (2017).
27. Zheng SQ, Palovcak E, Armache JP, Verba KA, Cheng Y, Agard DA. MotionCor2: anisotropic correction of beam-induced motion for improved cryo-electron microscopy. *Nat. Methods* **14**, 331–332 (2017).
28. Rohou, A. & Grigorieff, N. CTFFIND4: Fast and accurate defocus estimation from electron micrographs. *J. Struct. Biol.* **192**, 216–221 (2015).
29. Bepler, T., Kelley, K., Noble, A. J. & Berger, B. Topaz-Denoise: general deep denoising models for cryoEM and cryoET. *Nat. Commun.* **11**, 5208 (2020).
30. Kinman, L. F., Powell, B. M., Zhong, E. D., Berger, B. & Davis, J. H. Uncovering structural ensembles from single-particle cryo-EM data using cryoDRGN. *Nat. Protoc.* **18**, 319–339 (2023).
31. Zhong, E. D., Bepler, T., Berger, B. & Davis, J. H. CryoDRGN: reconstruction of heterogeneous cryo-EM structures using neural networks. *Nat. Methods* **18**, 176–185 (2021).
32. Pettersen EF, Goddard TD, Huang CC, Meng EC, Couch GS, Croll TI, Morris JH, Ferrin TE. UCSF ChimeraX: Structure visualization for researchers, educators, and developers. *Protein Sci.* **30**, 70–82 (2021).
33. Afonine PV, Poon BK, Read RJ, Sobolev OV, Terwilliger TC, Urzhumtsev A, Adams PD. Real-space refinement in PHENIX for cryo-EM and crystallography. *Acta Crystallogr. Sect. Struct. Biol.* **74**, 531–544 (2018).
34. Emsley, P., Lohkamp, B., Scott, W. G. & Cowtan, K. Features and development of Coot. *Acta Crystallogr. D Biol. Crystallogr.* **66**, 486–501 (2010).
35. Song Y, DiMaio F, Wang RY, Kim D, Miles C, Brunette T, Thompson J, Baker D. High-Resolution Comparative Modeling with RosettaCM. *Structure* **21**, 1735–1742 (2013).
36. Salomon-Ferrer, R., Case, D. A. & Walker, R. C. An overview of the Amber biomolecular simulation package. *WIREs Comput. Mol. Sci.* **3**, 198–210 (2013).
37. Maier JA, Martinez C, Kasavajhala K, Wickstrom L, Hauser KE, Simmerling C. ff14SB: Improving the Accuracy of Protein Side Chain and Backbone Parameters from ff99SB. *J. Chem. Theory Comput.* **11**, 3696–3713 (2015).
38. Darden, T., York, D. & Pedersen, L. Particle mesh Ewald: An N·log(N) method for Ewald sums in large systems. *J. Chem. Phys.* **98**, 10089–10092 (1993).
39. Miyamoto, S. & Kollman, P. A. Settle: An analytical version of the SHAKE and RATTLE algorithm for rigid water models. *J. Comput. Chem.* **13**, 952–962 (1992).
40. Miao, Y., Feher, V. A. & McCammon, J. A. Gaussian Accelerated Molecular Dynamics: Unconstrained Enhanced Sampling and Free Energy Calculation. *J. Chem. Theory Comput.* **11**, 3584–3595 (2015).
41. Ma, W., You, S., Regnier, M. & McCammon, J. A. Integrating comparative modeling and accelerated simulations reveals conformational and energetic basis of actomyosin force generation. *Proc. Natl. Acad. Sci.* **120**, e2215836120 (2023).

3.8 Acknowledgement

Chapter 3, in full, is a reprint of the material as it appears in *Nature Structural & Molecular Biology*: *Multiple steps of dynein activation by Lis1 visualized by cryo-EM.* Kendrick, A.A.; Nguyen, K.H.V.; Ma, W.; Karasmanis, E.P.; Amaro, R.E.; Reck-Peterson, S.L.; Leschziner, A.E. The dissertation author contributed significantly to the design, data collection, and analysis in this work.

Chapter 4 Cryo-EM captures early intermediate steps in dynein activation by LIS1

4.1 Results

Cryo-EM reveals the conformational landscape of full-length human dynein activation by LIS1

To visualize the conformational landscape of dynein activation by LIS1, we incubated full-length human dynein with ATP and LIS1 at room temperature for 5 minutes (Fig. 4.1a). This sample was vitrified and used to collect cryo-EM data. As expected, data processing revealed significant heterogeneity (Supplementary Fig. 4.1-4.3). We identified three major species: individual dynein motors (Open), Phi, and a third state similar to Phi but with two LIS1 β-propellers bound to dynein, which we termed Pre-Chi (Fig. 4.1b). Two-dimensional (2D) class averages for this state also resembled Chi but lacked the second set of LIS1 β-propellers found in Chi[1]. Based on these and other observations discussed later in the text, we propose that this state represents a novel intermediate state in the dynein activation pathway.

To fully understand dynein's activation pathway, we began by analyzing particles corresponding to Open. We observed significant conformational and compositional heterogeneity in the Open species and used several approaches to sort out the coexisting subclasses (Supplementary Fig. 4.2)[2–4]. We obtained six different Open subclasses, which we categorized based on the linker conformation (bent, intermediate, or straight) and the presence or absence of LIS1 (Fig. 4.1c).

For Phi, we obtained a 2.7 Å structure of the motor domain and a 4.4 Å structure of the tail (Supplementary Fig. 4.1, 4.3 and 4.4). The higher resolution of the tail in our map compared to the previously published Phi tail structures[5] allowed us to model additional sections of the dynein heavy and accessory chains (IC, ROBL(LC), and LIC).

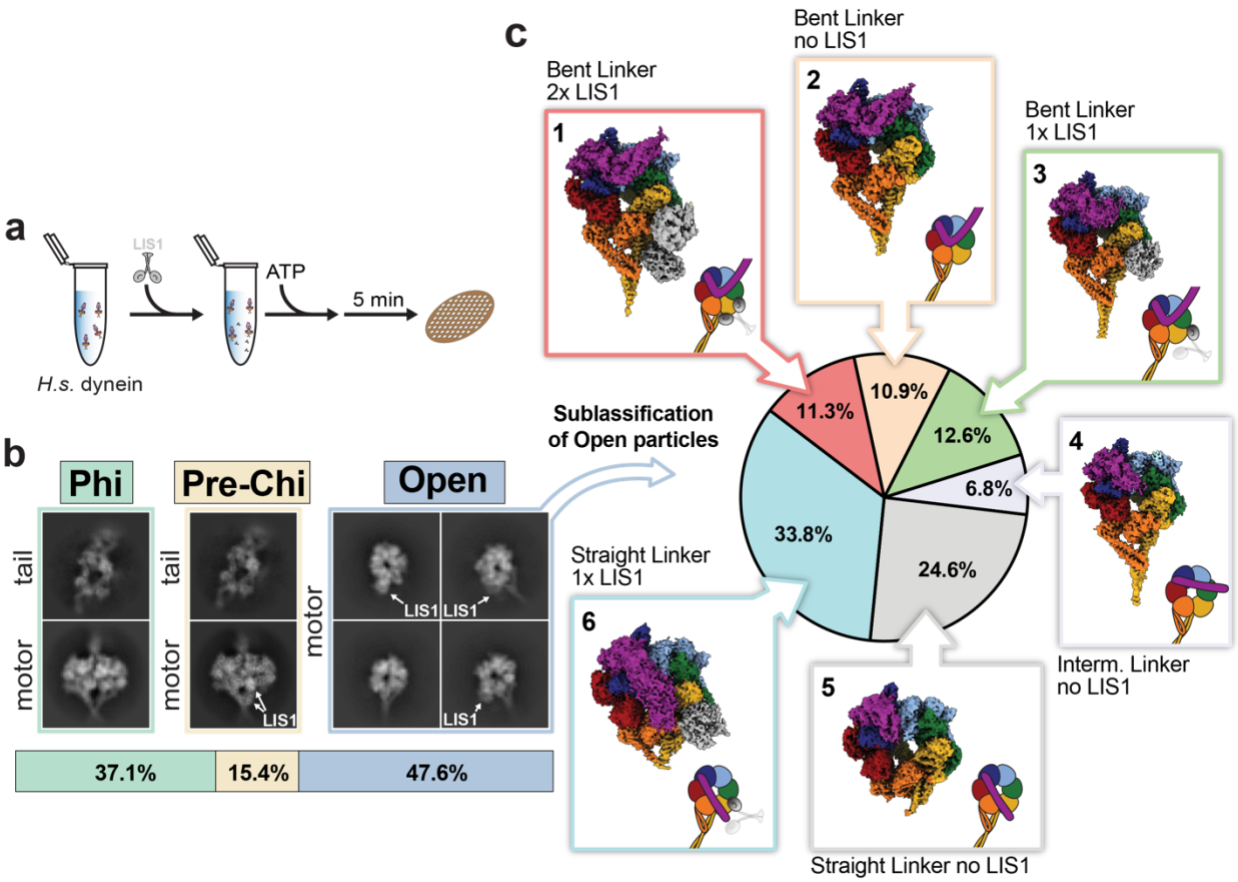

Figure 4.1 Conformational landscape of dynein activation by LIS1 in the presence of ATP. **a**, Schematic representation of the cryo-EM sample preparation pipeline. **b,** Distribution of particles corresponding to the three main species identified in the cryo-EM dataset: Phi, Pre-Chi, and Open. Representative 2D class averages are shown. In the case of Phi and Pre-Chi, representative 2D class averages of the dynein tails, which were processed separately, are shown above those for the motor domains. LIS1 is indicated whenever present in the averages. **c**, Further processing identified six subclasses in the Open species. The particle distribution is indicated with the corresponding cryo-EM maps next to the section in the pie chart.

Pre-Chi may be an early step in dynein's activation pathway

We next turned to the Pre-Chi species. Its 2D classes showed Phi-like features and had only one set of LIS1 β-propellers bound (Fig. 4.1b and Supplementary Fig. 4.5) instead of the two seen in Chi. Thus, we named this species "Pre-Chi" although we cannot rule out the possibility that this species follows Chi in the dynein activation pathway. We obtained a 3.1 Å structure of the Pre-Chi motor domains (Fig. 4.2a-d and Supplementary Fig. 4.1). The nucleotide

state of Pre-Chi is the same as that of Phi (Fig. 4.2e-f and Supplementary Fig. 4.6). Separately, we obtained a 6.2 Å reconstruction of the tail portion of Pre-Chi (Fig. 4.2a-b and Supplementary Fig. 4.3). At the current resolution, we could not observe any differences between the tails of Phi and Pre-Chi (Fig. 4.3a-b). Finally, we analyzed the interface between dynein monomers in Pre-Chi to understand how LIS1 disrupts Phi. The LIS1-induced opening of one side in Pre-Chi disrupts three of the four interfaces involved in Phi stabilization (Linker:Linker, Linker:AAA4, AAA5:AAA5, Fig. 4.3c-g)[5,6]. The Linker:Linker interface is only disrupted on the side where LIS1 is bound (Fig. 4.3d). The AAA5:AAA5 and Linker:AAA4 interfaces are both weakened, with three of the four salt bridges in Phi being disrupted on the LIS1-bound side in the former (Fig. 4.3e) and two of three salt bridges disrupted on both faces in the latter (Fig. 4.3f-g).

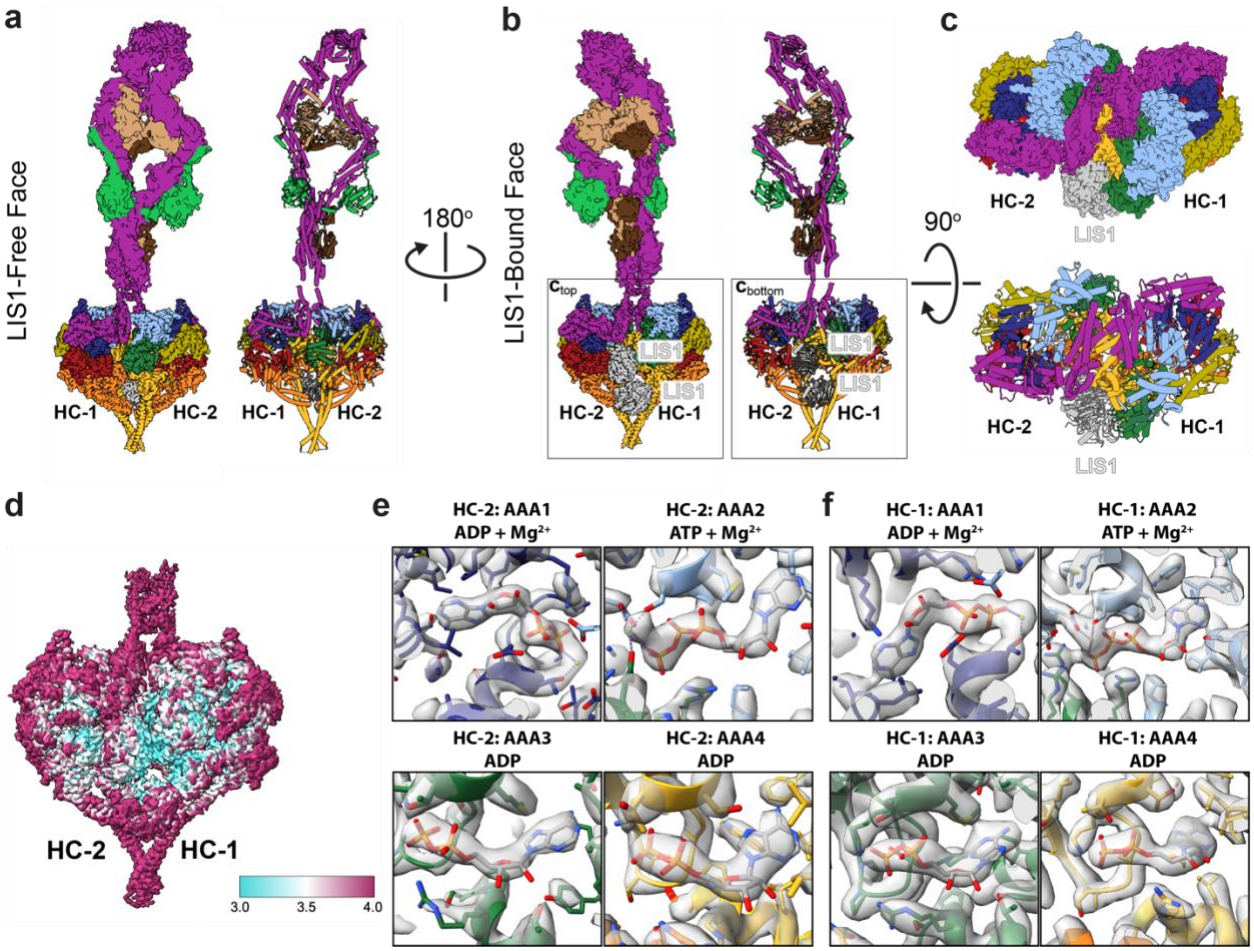

Figure 4.2 Structure of the Pre-Chi dynein-LIS1 complex. a,-c, Cryo-EM maps and models of the motor and tail domains of the Pre-Chi dynein-LIS1 complex are shown in three orientations: (**a**) LIS1-free face, (**b**) LIS1-bound face, and (**c**) a "top view" where the Pre-Chi motors are shown enlarged and from the perspective of the tail. LIS1 is highlighted in the LIS1-bound (**b**) and top (**c**) views. **d,** Local resolution map of Pre-Chi. **e, and f,** Nucleotide states of AAA1-AAA4 in Motor 2 (Heavy Chain 2, HC-2) (e) and Motor 1 (Heavy Chain 1, HC-1) (f).

Phi dynein has pseudo-two-fold symmetry; the motor domains have true two-fold symmetry, but that symmetry is broken in the tails[5]. We wondered whether the asymmetric nature of the tails biases the binding of LIS1 to one face of the Phi motors by making that side more prone to breathing. Our Pre-Chi structure suggested that LIS1 binds preferentially to the side of Phi where the bulk of the accessory chains of the dynein tail are found (Fig. 4.2b). To see

if we could find a population of Pre-Chi with LIS1 bound to the other face, we revisited the tail processing for Pre-Chi and Phi (Supplementary Fig. 4.3). We subclassified the Pre-Chi particles and viewed all the volumes (Supplementary Fig. 4.7). As a point of reference, we looked for density in the volumes that correspond to the IC-LC tower of accessory chains, a feature that is only observable on one face of Phi dynein. Whenever density for the IC-LC tower is present in our Pre-Chi volumes, it is located on the same face as LIS1. We did not observe any volumes with LIS1 bound to the other face (Supplementary Fig. 4.7b-e).

Figure 4.3 Phi-stabilizing contacts are disrupted in Pre-Chi. a, Superposition of Pre-Chi (rainbow) and Phi (grey) models. HC-1 was used as the reference to align the models. Although the Pre-Chi model is shown from the LIS1-bound face, LIS1 was omitted for clarity. **b,** Map of interatomic vectors connecting equivalent α carbons in Phi and Pre-Chi. The length of each vector is proportional to the distance between the atoms in Phi and Pre-Chi. **c,** The four main interfaces between the motors in Phi are highlighted in the context of the boxed model in panel (**a**)**:** Linker:Linker, Linker:AAA4, AAA5:AAA5, and Stalk:Stalk. **d,-g,** Close-ups of the three interfaces highlighted in (**c**) that are disrupted by the formation of Pre-Chi: Linker:Linker (**d**), AAA5:AAA5 (**e**), and Linker:AAA4 (**f-g**). The top panel corresponds to the Phi model and the bottom panel corresponds to the Pre-Chi model. Key residues, motor chains, LIS1 ring, and the domain(s) of the motor being displayed are highlighted on each panel. Interactions are shown with dotted lines, with their distances (in Å) indicated. There was no significant change in the Stalk:Stalk interface. There are differences in the Linker:AAA4 interface between the LIS1-bound face (**f**), and the LIS1-free face (**g**).

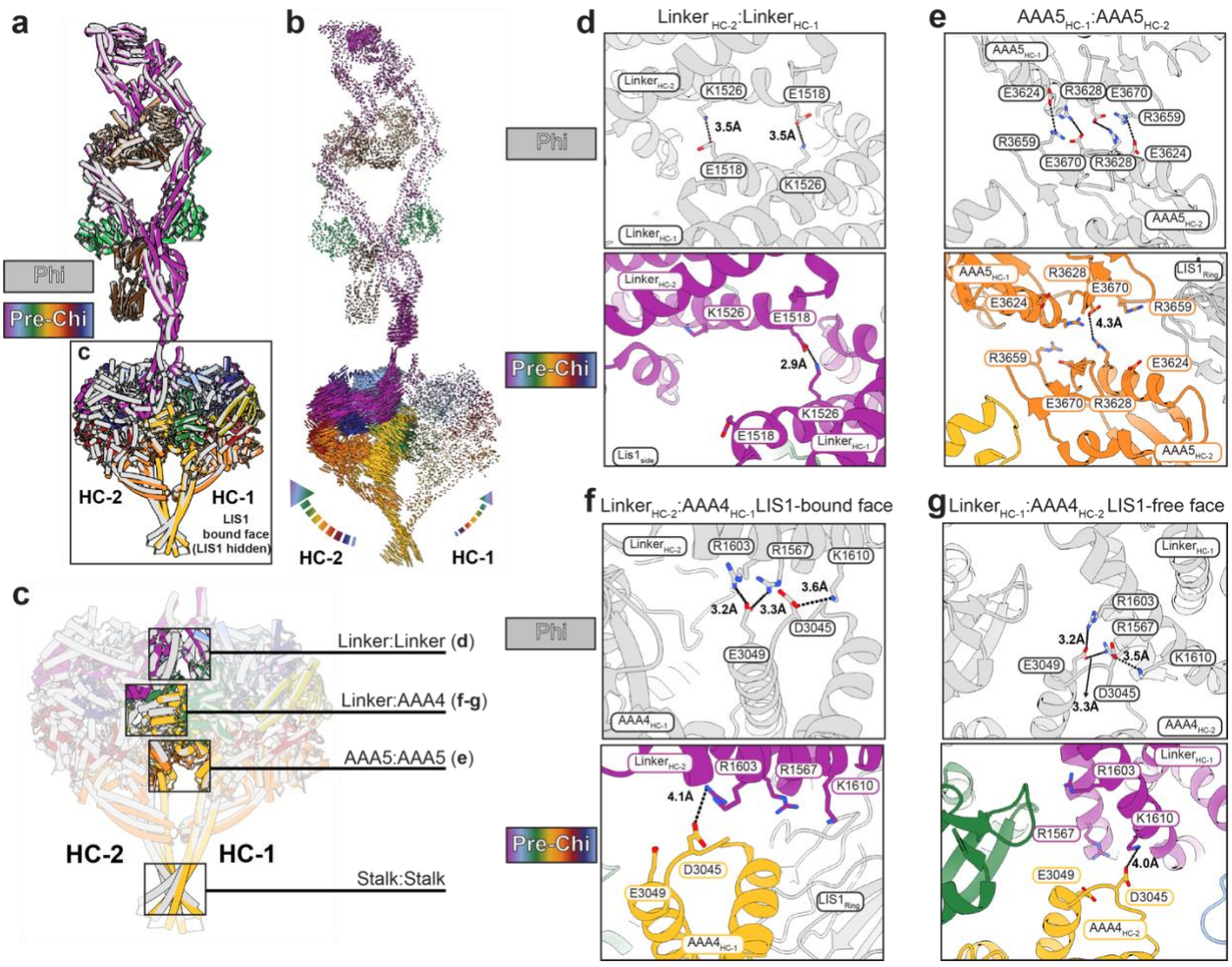
a
b
c
d
e
f
g
Phi
Pre-Chi
HC-2
HC-1
LIS1 bound face (LIS1 hidden)
Linker:Linker (d)
Linker:AAA4 (f-g)
AAA5:AAA5 (e)
Stalk:Stalk
Linker HC-2 :Linker HC-1
AAA5 HC-1 :AAA5 HC-2
Linker HC-1 :AAA4 HC-2 LIS1-bound face
Linker HC-1 :AAA4 HC-2 LIS1-free face
K1526
E1518
3.5Å
2.9Å
E3624
R3628
E3670
R3659
4.3Å
R1603
R1567
K1610
D3045
E3049
3.6Å
3.2Å
3.3Å
4.1Å
3.5Å
4.0Å

Structural comparison between Pre-Chi and Chi

We previously built a model of human Chi based on our structure of yeast Chi to investigate the functional impact of Chi-disrupting mutations on the assembly of the human DDA complex[1]. We compared that model of Chi to Pre-Chi by superimposing one of their heavy chains (Fig. 4.4a). This alignment showed an increased separation between the motor domains in Chi relative to Pre-Chi, driven by the additional LIS1 dimer wedged between the motor domains in Chi (Fig. 4.4b).

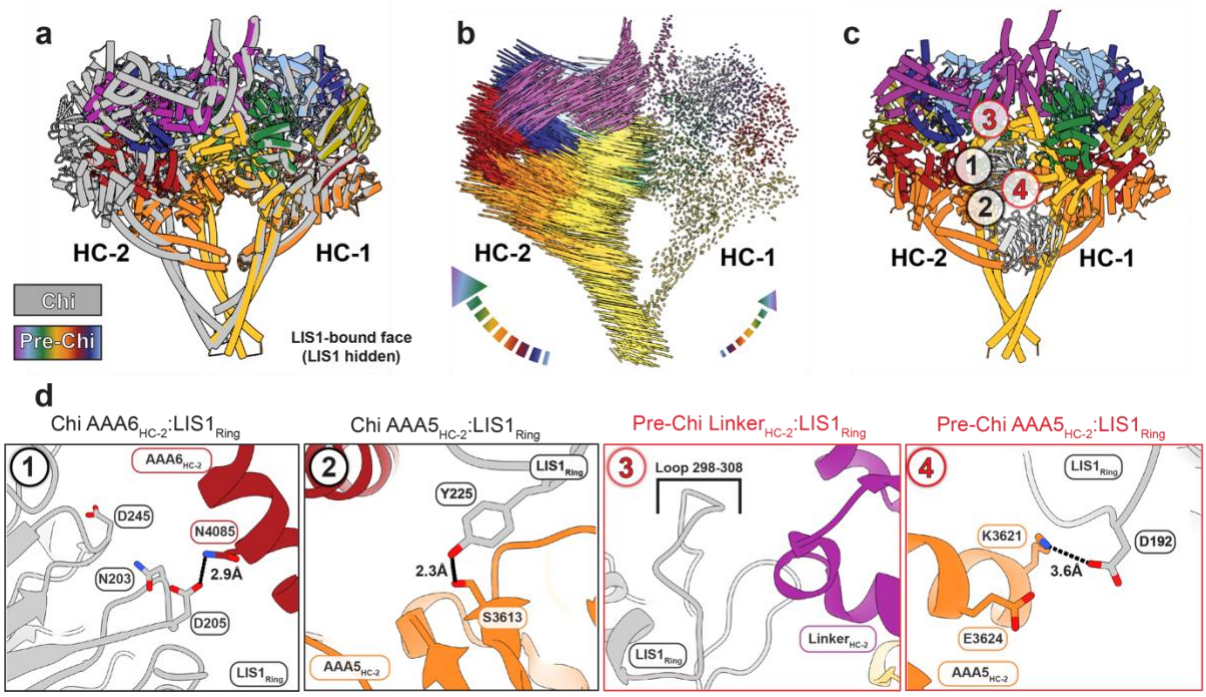

Figure 4.4 Comparison of Pre-Chi with Chi. a, Superposition between Chi and Pre-Chi. The model of human Chi from our previous work (dark gray) and human Pre-Chi motor (rainbow) were superimposed and aligned using HC-1. **b,** Interatomic vectors connecting equivalent alpha carbons in Pre-Chi and Chi for the superposition shown in a. **c,** Pre-Chi model viewed from the LIS1-bound face with interfaces present in both Chi and Pre-Chi (#1-2 in black circles) and Pre-Chi-specific interfaces (#3-4 in red circles) highlighted. **d,** Close ups of the interfaces highlighted in (c). Residues involved in the interfaces and the names of the domains interacting with $LIS1_{ring}$ are highlighted in each panel. Interactions are shown with dotted lines, with their distances (in Å) indicated.

In Chi, the LIS1 bound to the ring of one motor domain ($site_{ring}$) interacts, in trans, with the AAA5 and AAA6 modules of the other dynein motor. Based on the yeast Chi model, we predicted that human LIS1 interacts with AAA5 through Y225 and with AAA6 through N203, D205, and D245[1]. In agreement with those predictions, we showed that mutations in these LIS1 residues significantly impaired the formation of activated human DDA complexes[1]. The structure of human Pre-Chi presented here supports our previous modeling (Fig. 4.4c-d, black circles #1-2).

In addition to the interactions that, based on our models, are common to both Pre-Chi and Chi, we identified two novel Pre-Chi-specific interfaces (Fig. 4.4c, red circles #3-4). The first interface involves a trans interaction between the β-propeller of LIS1 bound to $site_{ring}$ in one motor domain (HC-1) and the linker domain of the other motor domain (HC-2) (Fig. 4.4c-d, red circle #3-4). This interaction is mediated by a loop on LIS1 (residues 298-308) that has not been modeled in any structure of human dynein-LIS1 to date[7]. Because this loop is not fully resolved in our map, we could not build individual side chains for residues 300-306, some of which are likely to interact with the linker of HC-2. Interestingly, one of the residues in this region, E300, has been reported to be a missense mutation in lissencephaly patients[8].

The second Pre-Chi interface involves another interaction in trans between LIS1 bound to $site_{ring}$ in HC-1 and AAA5 of HC-2 (Fig. 4.4c-d, red circle #4). Notably, the residue involved in this interaction (K3621) is very close to a residue involved in stabilizing the autoinhibited Phi conformation (E3624).

The Pre-Chi-specific interface is required for efficient human dynein complex assembly

To assess the functional consequences of disrupting the dynein linker-LIS1 contacts we identified specifically in Pre-Chi, we turned to in vitro motility assays. In these assays, we measure both the motility and the efficiency of the assembly of active human DDA complexes at the single molecule level. In vitro, LIS1 enhances the formation of DDA complexes containing two dynein dimers, which move faster than complexes containing a single dynein dimer[9,10]. Our structure showed that dynein's linker contacts LIS1 via a loop (residues 298-308, Fig. 4.4d red #3). To test the functional role of this contact in Pre-Chi, we deleted this loop in LIS1 (LIS1$^{\Delta 298-308}$) and examined the effect of wild type LIS1 or LIS1$^{\Delta 298-308}$ on the motility of dynein, dynactin complexes containing the activating adaptor BICD2 (DDB) using single-molecule motility assays. As we have previously shown, pre-incubation of DDB with 300 nM wild-type human LIS1 increased the velocity and run frequencies (number of processive runs/ μm of microtubule length) (Fig. 4.5a-c)[1,10]. In contrast, there was no significant difference in dynein velocity or the run frequencies between DDB complexes alone or those pre-incubated with 300 nM LIS1$^{\Delta 298-308}$. These data suggest that the dynein linker–LIS1 contact we identified in our Pre-Chi structure is required for LIS1's role in the efficient formation of active DDB complexes, likely by relieving dynein autoinhibition in the Phi conformation.

Figure 4.5 The Pre-Chi-specific contact between LIS1 and dynein's linker is required for LIS1's effect on dynein motility. a, Representative kymographs from single-molecule motility assays with purified TMR–dynein–dynactin–BICD2 in the absence (white circle) or presence (black circle) of human LIS1 wild type or LIS1$^{\Delta 298\text{-}308}$. Scale bars, 10 μm (*x*) and 100 s (*y*). **b,** Single-molecule velocity (mean ± standard deviation of the means of each replicate) of TMR–dynein–dynactin–BICD2 complexes in the absence (white circles) or presence (black circles) of human LIS1 or LIS1$^{\Delta 298\text{-}308}$. Superplots show all individual data points for each of the four technical replicates. n values for each replicate are: no LIS1, $n = 70, 70, 50, 91$; LIS1, $n = 90, 85, 58, 117$; LIS1$^{\Delta 298\text{-}308}$, $n = 116, 125, 89, 124$. Larger shapes denote the mean of each of the four technical replicates. No LIS1 and LIS1 $^{**}P = 0.0018$, No LIS1 and LIS1$^{\Delta 298\text{-}306}$ ns $P = 0.9955$, LIS1 and LIS1$^{\Delta 298\text{-}308}$ $^{**}P = 0.0012$. Statistics were generated on the means of the four replicates using a One-Way ANOVA with Tukey's multiple comparison test. **c,** Superplots show Run frequencies (processive events /μm of microtubule length; mean ± standard deviation of the means of each replicate) of TMR–dynein–dynactin–BICD2 complexes in the absence (white circle) or presence (black circle) of unlabeled wild type human LIS1 or LIS1$^{\Delta 298\text{-}308}$. Data points are represented as triangles, circles, squares, and diamonds corresponding to single measurements within each technical replicate (no LIS1, $n = 14, 12, 11, 8$; LIS1, $n = 12, 7, 7, 7$; LIS1$^{\Delta 298\text{-}306}$, $n = 11, 5, 8, 9$). No LIS1 and LIS1 $^{*}P = 0.012$. Statistical analysis was done using a One-Way ANOVA with Tukey's multiple comparison test. **d**, Role of LIS1 in the activation of dynein. This schematic is an updated version of the pathway introduced in Figure 1b that incorporates the Pre-Chi intermediate identified in this study.

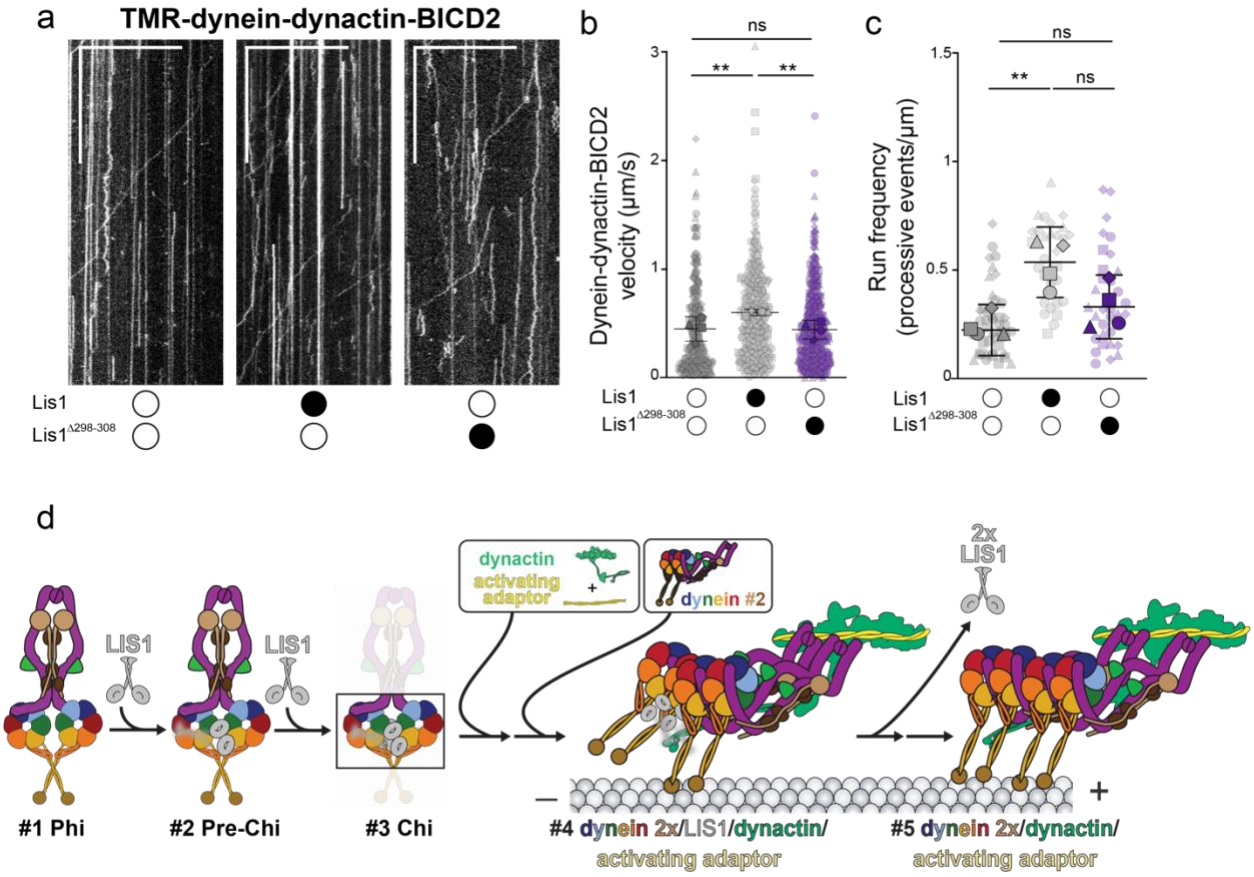
a
TMR-dynein-dynactin-BICD2
Lis1
Lis1Δ298-308
b
ns
**
**
Dynein-dynactin-BICD2 velocity (μm/s)
3
2
1
0
Lis1
Lis1Δ298-308
c
ns
**
ns
Run frequency (processive events/μm)
1.5
1
0.5
0
Lis1
Lis1Δ298-308
d
LIS1
LIS1
dynactin
activating adaptor
dynein #2
2x LIS1
#1 Phi
#2 Pre-Chi
#3 Chi
#4 dynein 2x/LIS1/dynactin/ activating adaptor
#5 dynein 2x/dynactin/ activating adaptor
–
+

4.2 Discussion

LIS1 binding to dynein is asymmetric in Pre-Chi

An interesting feature we observed in Pre-Chi was the asymmetric binding of LIS1 to the dynein tail (Fig. 4.2b). We confirmed that whenever we observed density for the IC-LC tower of the accessory chains in the Pre-Chi maps, LIS1 was bound to that same face. We hypothesize that the asymmetric nature of the Phi tail induces preferential breathing of the side where the bulk of the accessory chains are found, which in turn leads to the binding of LIS1 to that face. Given this, we speculate that this face might also be more labile during tail rearrangements downstream in the dynein-LIS1 activation pathway (Supplementary Fig. 4.7). Although several studies have shown that Nde1 and Ndel1, and their fungal homologs, co-localize with dynein and LIS1, and may be involved in recruiting LIS1 to dynein[11–14], our structural analysis shows that the asymmetric interaction of LIS1 with Phi dynein is driven by the properties of the Phi conformation itself and does not require additional factors.

Two LIS1 dimers are likely required throughout the activation and assembly process

While we did not observe Chi in the cryo-EM data we collected for this study, Chi-specific interfaces are maintained in Pre-Chi (Fig. 4.4). The sample from which we previously solved Chi was designed to be monomeric (i.e. motor domains lacking the tail) and was trapped in a specific nucleotide state[1,15]. In that sample, only a small percentage of particles corresponded to the Chi conformation. We also observed a small percentage of Chi-like 2D class averages when we incubated monomeric dynein with ATP[16]. These observations from our previous studies suggest that Chi is a short-lived species in monomeric samples and could be an even shorter-lived species in a sample containing full-length dynein in the presence of ATP.

Several observations support the existence of Chi as an intermediate that follows Pre-Chi. First, the two LIS1 dimers wedged between the dynein motors in Chi disrupt more Phi-stabilizing interactions than Pre-Chi. Importantly, the second LIS1 dimer seen in Chi increases the distance between dynein's linkers; this would contribute to the destabilization of the tail that is required for the conformational changes need to convert its pseudo-twofold symmetry to the parallel arrangement in the active DDA complex. Finally, DDA complexes have been shown, structurally, to contain two LIS1 dimers bound to a single dynein dimer[17], a stoichiometry consistent with Chi. These observations suggest that a stoichiometry of two LIS1 per dynein dimer may be present throughout the activation and assembly process.

Model for dynein activation by LIS1

Determining how LIS1 facilitates the relief of dynein autoinhibition and the assembly of a fully activated DDA complex has been a major challenge in the field. Here, we used a heterogeneity mining approach to answer how the autoinhibition of full-length human dynein is relieved by LIS1 in the presence of ATP. We identified Pre-Chi as an intermediate state in the LIS1-meditated dynein activation pathway and propose that this species represents an early step in the relief of dynein autoinhibition. A single set of LIS1 β-propellers are wedged on one side between the dynein motor domains; this partially disrupts three of the four interfaces responsible for maintaining dynein autoinhibition (Fig. 4.5d, #1-2).

In this model, Pre-Chi is followed by Chi, where a second set of LIS1 β-propellers becomes wedged between the dynein motor domains, fully disrupting three of the four interfaces responsible for maintaining dynein autoinhibition (Fig. 4.5d, #3)[1]. This disruption likely initiates structural changes propagating throughout the complex, including the tail. While the specific role

of the tail during this transition remains unclear, we hypothesize that either at the Chi stage, or at state(s) closely following Chi, the dynein complex undergoes a significant conformational shift. This shift would involve transitions from the twisted pseudo-twofold symmetry of the autoinhibited state to the parallel symmetry associated with the translational symmetry of the dynactin complex to which dynein must bind. Following the release of dynein autoinhibition, LIS1 facilitates the coordination of dynein and dynactin to assemble the Dynein-Dynactin-JIP3-LIS1 (DDA-LIS1) complex (Fig. 4.5d, #4)[17]. We hypothesize that LIS1-mediated coordination, either within this complex or in earlier intermediates, enhances the recruitment of activating adaptors, thereby supporting the assembly of motile dynein complexes. Once the DDA complex forms on microtubules, LIS1 disengages from the complex, allowing the active transport complex to move at full velocity (Fig. 4.5d, #5).

Although the structures of Pre-Chi and Chi dynein provide a pathway for LIS1 to relieve the Phi conformation, the new LIS1-mediated interactions that form these intermediates must in turn be disrupted for dynein to be assembled into an active DDA complex. A possible mechanism is suggested by the observation that yeast LIS1 increases dynein's ATP hydrolysis rate in the absence of microtubules[16], which would increase the conformational flexibility of dynein, lowering the activation energy for the conformational changes required for full activation. Thus, after binding of LIS1 has led to the formation of Pre-Chi and Chi, an increase in the rate of ATP hydrolysis of dynein would facilitate the rearrangements that lead to formation of the fully active DDA complex. Future analysis using all components of the DDA complex and LIS1, in the presence of ATP, could capture a broader range of intermediate states and provide a deeper understanding of how LIS1 facilitates the activation and assembly of dynein.

4.3 Methods

Cloning, plasmid construction, and mutagenesis

The plasmids for full-length human cytoplasmic-dynein 1 (Addgene plasmid # 111903) and human LIS1 (Addgene plasmid #132539) were gifts from Andrew Carter (LMB-MRC). Human LIS1$^{\Delta 298\text{-}308}$ was generated through Genescript Express Mutagenesis & Site-Directed DNA Mutagenesis service.

Protein expression and purification

For baculovirus generation, each construct was individually transformed into DH10EMBacY chemically competent cells (Geneva Biotech), and bacmid DNA from these constructs was extracted using a blue/white colony screen. Colony PCR was used to confirm each dynein chain prior to transfection into SF9 cells. The recombinant baculovirus for each construct was individually produced in 2mL of SF9 cells at 0.5x10^6 cells/mL by transfection of the bacmid DNA using FuGene HD (Promega) according to the manufacturer's protocol (V0). After three days of incubation, V0s were harvested, and 1mL of V0 was used to infect a 50mL culture of SF9 at 1x10^6 cells/mL (V1). After three days of incubation, V1 viruses were harvested and stored at 4°C in the dark until required. Protein expression was induced by adding 6mL of V1 to 600mL of SF9 cells at 1x10^6 cells/mL and incubating the cells at 27°C on a shaker for three days at 90rpm. After the third day, cells were harvested by centrifugation (3500 rpm for 5 minutes at 4°C), and the pellet was resuspended in ice-cold 1x PBS and pelleted again. The supernatant was discarded, and the pellet was flash-frozen in liquid nitrogen and stored at -80°C.

Purification of full-length human cytoplasmic-dynein 1, human LIS1, and human LIS1$^{\Delta 298\text{-}308}$ was carried out as previously described[5,7,18,19]. Specifically, 4x600mL of frozen insect cell pellet were used to purify full-length human cytoplasmic-dynein 1, and 2x600mL of frozen insect cell pellet were used to purify human LIS1 and LIS1$^{\Delta 298\text{-}308}$. For LIS1 and LIS1$^{\Delta 298\text{-}308}$, both had a final concentration of ~1mg/mL and were flash-frozen in liquid nitrogen and stored at -80°C until use. For dynein, the protein was concentrated to ~ 0.1 mg/mL and used fresh to prepare cryo-EM grids the same day.

Electron microscopy sample preparation

Purified full-length dynein and LIS1 were combined at a 1:1 molar ratio with final concentrations of 0.3 uM. ATP was added to this sample to a final concentration of 1mM. The sample was incubated at room temperature for 5 minutes. For plunge freezing, we used a custom manual plunge freezer (UCSD Cryo-EM Facility) located in a humidified (>95% relative humidity) cold room maintained at 4°C [20]. In the cold room, the sample was applied to an UltraAuFoil 1.2/1.3, 300 grid (Quantifoil) that had been plasma-cleaned using a Gatan Solarus II plasma cleaner (10s, 15 Watts, 75% Ar/25% O2 atmosphere). The grid was manually blotted for ~4 to 5s using Whatman No.1 filter paper and immediately vitrified in a 50:50 ethane:propane liquid mixture cooled by liquid nitrogen.

Electron microscopy image collection and data processing

Data was collected at the UCSD Cryo-EM Facility on a Titan Krios G4 (Thermo Fischer Scientific) operating at 300 keV with a Falcon 4 direct electron detector and a Selectris X energy filter (<10 eV slit size). Automated data collection was performed using EPU, and images were

collected at a nominal magnification of 130,000x (0.935 Å/pixel size) with a total exposure dose of ~55 electrons/ Å^2. The defocus range was set to 0.5 – 2.5 µm.

On-the-fly motion correction and CTF estimation were done through cryoSPARC Live[2]. A total of 12,792 movies were collected initially, but we pruned that down to 11,686 movies by setting the parameters of CTF Fit to a range of 1-5 Å and Defocus Avg to a range of 0.61-3.25 µm in the Overview setting of cryoSPARC Live. Particles were initially selected using a blob picker in cryoSPARC Live, 2D classified, and the resulting averages were used as templates for Topaz training[21]. Particles were extracted after Topaz training with a box size of 352 pixels and binned to 7.48 Å/pixel, yielding 1,937,842 particles. These particles were subjected to two rounds of 2D classification, which yielded a final set of 690,084 particles. After 2D classification, the particles were used for ab-initio reconstruction of six classes, yielding four different Open classes, one Phi class, and one Pre-Chi class. All six classes with particles and maps were used for Heterogenous Refinement, where we obtained one Phi class, one Pre-Chi class, and two types of Open classes (Partial Open Bent/LIS1 and Open Straight/LIS1).

The particles corresponding to the Phi and Pre-Chi classes were re-extracted, unbinned to 0.935 Å/pixel. These particles and the corresponding maps were used to perform non-uniform refinement followed by local refinement and CTF/Defocus refinement to obtain final maps of the Phi and Pre-Chi motor domains. The particles from Phi and Pre-Chi from heterogeneous refinement were taken and combined to process the tails of Phi and Pre-Chi. The box size was expanded to 640 pixels and binned to 2.34 Å/pixel, yielding 195,092 particles. These particles were used to obtain reconstructions of the tails, followed by homogenous refinement. The map and particles were then taken into cryoDRGN, down-sampled to 128 pixels (2.34 Å/pixel), and used for low-resolution cryDRGN training[3]. Particles and maps that corresponded to Phi and Pre-

Chi was separated through K-means clustering. The clusters corresponding to Phi had 127,751 particles, and those for Pre-Chi had 45,549 particles. The particles were brought back into cryoSRPAC, the box size was expanded to 1200 pixels and binned to 9.35 Å/pixel, and these particles were used for a round of 2D classification followed by reconstruction and refinement. This yielded a low-resolution full-length dynein particle, which was used to recenter the particles to the center of the tail, with the box size decreased to 416 pixels and binned to 3.24 Å/pixel. These particles were used for another round of 2D classification and reconstruction. Finally, the particles were unbinned (0.935 Å/pixels), and a non-uniform refinement was used to generate the final map.

For the Partial Open Bent/LIS1, the particles and map from the heterogeneous refinement were taken and unbinned to 0.935 Å/pixel and used for refinement to generate a consensus map for cryoDRGN training. This map and particles were taken into cryoDRGN, down sampled to 128 pixels, and binned to 2.57 Å/pixel. After cryoDRGN low resolution training, the particles that had the best and unique clusters were separated and taken back into cryoSPARC for another round of ab-initio reconstructions and refinement.

For the Open Straight/LIS1, the particles and map from the heterogenous refinement were taken and unbinned to 0.935 Å/ Å/pixel and used for refinement to generate a consensus map for RELION 3D classification without alignment[22]. The best classes from here were taken back into cryoSPARC for another round of ab initio reconstructions and 3D refinement.

Model building and refinement

CryoSPARC's sharpening tools were used to enhance the quality of all maps used for model building. For the motor domain maps, the initial PDB models are listed in Table 4.1.

These models were docked into the corresponding motor domain densities using ChimeraX and adjusted as needed[23]. These models were subjected to rounds of real-space refinement in Phenix and manual corrections in Coot[24,25].

LIS1 was placed by rigid body docking of the previously determined human dynein monomer bound to 2xLIS1 structure (PDB: 8DYU)[7]. The β-sheets of the LIS1 β-propeller fit well into the map, and a short α-helix (residues 288–297), the only α-helix within the β-propeller, docked precisely in both the $Site_{ring}$ and $Site_{stalk}$ configurations. The orientation of this helix and the positioning of the binding interface were consistent with previous structures.

For the tail domains of the Phi and Pre-Chi species, the heavy chain was initially modeled based on PDB: 8PTK[17]. Newly resolved densities in these species required further modeling, which was accomplished using AlphaFold2 to predict the newly resolved areas of the accessory chains, including the intermediate chain (IC), light intermediate chain (LIC), and light chain (LC)[26,27]. The predicted models were docked into the density maps with ChimeraX and refined through additional rounds of Phenix real-space refinement and manual adjustments in Coot.

Single-molecule motility assays and TIRF microscopy imaging

Single-molecule motility assays were performed in flow chambers constructed using glass coverslips. To reduce non-specific binding, coverslips were washed in 1 M hydrochloric acid (HCl), heated to 55 ºC, for at least 4 hours. Cleaned coverslips were mounted on a slide with double-sided tape creating ~10 µL volume chambers. Motility chambers were coated (5 min at room temperature) sequentially with 1 mg/mL Biotin-BSA (SIGMA), 0.5 mg/mL streptavidin (Thermo Scientific) diluted in dynein lysis buffer (DLB; 30 mM HEPES pH 7.4, 50 mM potassium acetate, 2 mM magnesium acetate, 1 mM EGTA, 10% glycerol, 1 mM DTT).

Microtubules were polymerized from tubulin prepared from bovine brain, as previously described[53] and contained ~10% biotin-tubulin (Cytoskeleton) for attachment to the biotin-BSA-streptavidin coated chambers and ~10% Alexa Fluor 488 (Thermo Fisher Scientific) tubulin for visualization. Imaging was done in dynein-lysis buffer supplemented with 20 μM taxol, 1 mg mL^{-1} casein, 5 mM Mg-ATP, 71.5 mM β-mercaptoethanol, and an oxygen scavenger system containing 0.4% glucose, 45 μg mL^{-1} glucose catalase (Sigma-Aldrich), and 1.15 mg mL^{-1} glucose oxidase (Sigma-Aldrich). Measurement of motility was done by imaging 0.125 nM labeled TMR-dynein, 0.9 nM unlabeled dynactin, 5 nM BICD2 complexes alone with LIS1 buffer (10 mM Tris pH 8.0, 2 mM MgOAc, 150 mM KOAc, 1 mM EGTA, 1mM DTT, 10% glycerol), 300 nM LIS1 or $LIS1^{\Delta 298\text{-}308}$. The dynein, dynactin, and BICD2 complexes were incubated on ice for 10 min to allow the dynein-dynactin-activator adaptor complex to form. Subsequently, LIS1 or buffer was added to the active dynein complexes and the mixture was incubated on ice for an additional 10 min prior to TIRF imaging. Three movies per condition were recorded every 0.3 s for 3 min.

Imaging was performed with an inverted microscope (Nikon, Ti-E Eclipse) equipped with a 100×1.49 N.A. oil immersion objective (Nikon, Plano Apo). The *xy* position of the stage was controlled by a ProScan linear motor stage controller (Prior). The microscope was equipped with an MLC400B laser launch (Agilent) with 405 nm (30 mW), 488 nm (90 mW), 561 nm (90 mW), and 640 nm (170 mW) laser lines. The excitation and emission paths were filtered using appropriate single bandpass filter cubes (Chroma). The emitted signals were detected with an electron multiplying CCD camera (Andor Technology, iXon Ultra 888). Illumination and image acquisition were controlled by NIS Elements Advanced Research software (Nikon).

TIRF motility data analysis

TIRF motility data analysis was done on kymographs generated in Fiji, as previously described[28,29]. Kymographs were generated for each microtubule in the three movies recorded for each condition. Velocities were calculated from molecules that moved processively (continuously moving along a microtubule track) for more than five frames. Non-motile or diffusive events were counted separately and were not included in the velocity analysis. Processive events were defined as events that move unidirectionally and do not exhibit directional changes greater than 600 nm. Diffusive events were defined as events that exhibit at least one bidirectional movement greater than 600 nm in each direction. Static events were defined as events that do not exhibit movement (less than 600 nm in each direction). Single-molecule movements that change apparent behavior (for example, shifting velocity mid run or from non-motile to processive) were counted as multiple velocity events. Run frequency (processive events/ μm) were calculated by counting the number of processive events for each microtubule in individual movies and dividing this number by the microtubule length.

Statistical analysis

Brightness and contrast were adjusted in Fiji for videos and kymographs. All statistical tests were generated using GraphPad Prism 10. The exact value of *n*, evaluation of statistical significance, *P* values, and specific statistical analysis are described in the corresponding figures and figure legends. All TIRF experiments were analyzed from four independent replicates, and individual analysis of each replicate showed similar results. For velocity analysis, frequency distributions were first calculated for each replicate, and data were fit to a Gaussian distribution

to calculate mean values. Statistical analysis was performed on the means of each biological replicate using a one-way ANOVA with Tukey's multiple comparison test.

Data availability

Cryo-EM maps have been deposited in the Electron Microscopy Data Bank under accession codes: Pre-Chi motor – EMD-47342, Pre-Chi tail – EMD-47430, Phi motor – EMD-47373, Phi tail – EMD-47443, Bent/2xLIS1 – EMD-47370, Bent – EMD-47360, Bent/1xLIS1 – EMD-47372, Interm. – EMD-47371, Straight/1xLIS1 – EMD-47429, Straight – EMD-47377.

Atomic coordinates have been deposited in the Protein Data Bank under accession codes: Pre-Chi motor – 9DZY, Pre-Chi tail – 9E23, Phi motor – 9E0X, Phi tail – 9E28, Bent/2xLIS1 – 9E0T, Bent – 9E0K, Bent/1xLIS1 – 9E0W, Interm. – 9E0U, Straight/1xLIS1 – 9E22, Straight – 9E0Y.

Unprocessed micrographs are deposited to EMPIAR under the following accession numbers: EMPIAR-12715. All other data will be made available upon request. Source data are provided with this manuscript.

4.4 Supplementary Figures

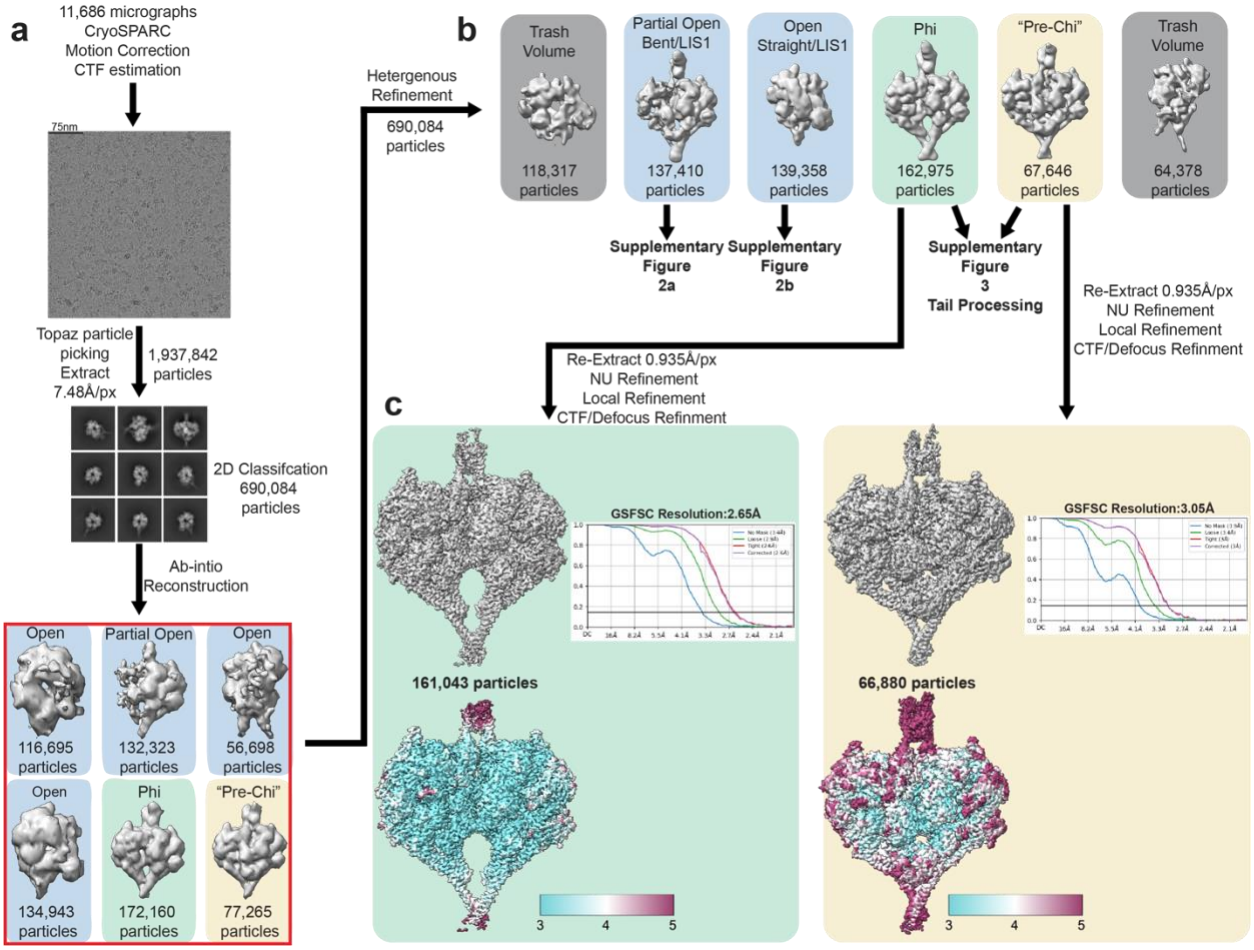

Supplementary Figure 4.1 Cryo-EM data processing workflow for human full-length dynein + LIS1 dataset. a. Dose-weighted movies were aligned, and CTF was estimated in cryoSPARC live. Particle extraction (binned by 8) was performed in cryoSPARC using a Topaz-trained model. Good particles from 2D classification jobs were used to generate six classes of ab-initio reconstructions in cryoSPARC. Ab-initio classes generated were color-coded according to the three main classes: Phi (light green), Pre-Chi (light yellow), and Open (light blue). All six maps and particles from the ab-initio classes were picked and carried on into heterogeneous refinement. **b.** Six volumes from the heterogeneous refinement job. "Trash" volumes are highlighted in dark grey. Open classes were further separated and refined as shown in Extended Data Fig 2. Phi and Pre-Chi were unbinned and further refined to their final maps. The Fourier Shell Correlation (FSC) plots are shown next to the respective final maps.

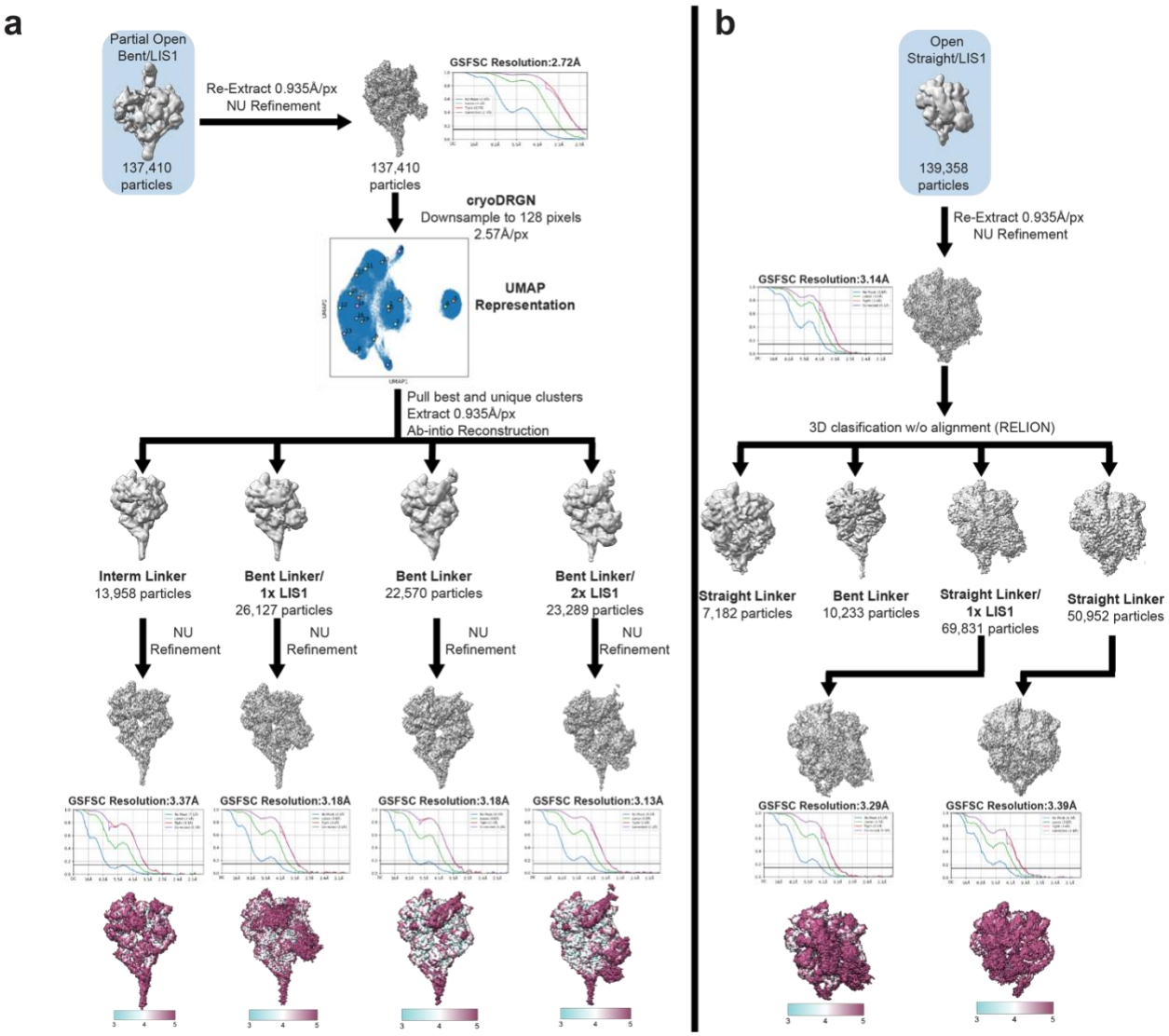

Supplementary Figure 4.2 Data processing workflow for Open species. a. Heterogeneous processing of Open species class with the linker in the bent conformation. The "Partial Open Bent/LIS1" class is the same one shown in Extended Data Fig 1b. This class was unbinned and refined to obtain a map for cryoDRGN training. Particles were downsampled and subjected to a round of low-resolution cryoDRGN training. From the training, we pulled the best and most unique clusters from the training and returned the individual subclass particles into cryoSPARC. Each subclass is defined by their linker conformation and the presence or absence of LIS1. These subclasses were further refined to their final map. The Fourier Shell Correlation (FSC) plots are shown next to the respective final maps. **b**. Heterogeneous processing of the Open species class with the linker in the straight conformation. The "Open Straight/LIS1" class is the same one shown in Extended Data Fig 1b. This class was unbinned and refined to get a refined map for RELION 3D classification without alignment. The best subclasses were taken back into cryoSPARC to further refine their final map. The Fourier Shell Correlation (FSC) plots are shown next to the respective final maps.

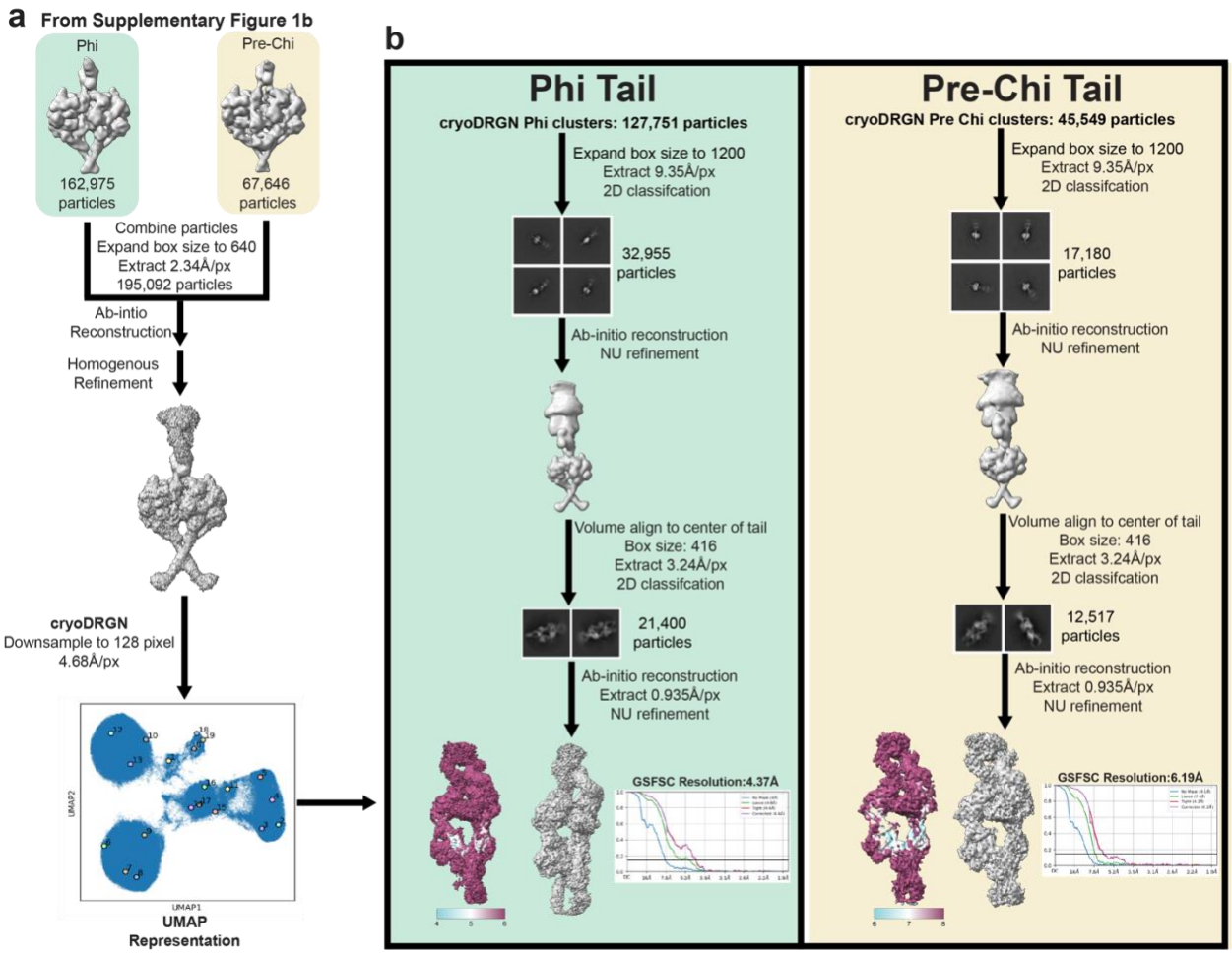

Supplementary Figure 4.3 Data processing of the tail domain of Phi and Pre-Chi. a. CryoDRGN analysis of combined Phi and Pre-Chi classes. The Phi and Pre-Chi classes are those shown in Extended Figure 1b. Particles from both classes were combined, and the box size was expanded further to include part of dynein's tail. A general refined consensus map was subjected to cryoDRGN low-resolution training, and Phi and Pre-Chi clusters were separated. **b**. Phi (green panel) and Pre-Chi (yellow panel) tail workflows. Both workflows use the same process, which is discussed in the methods section. The Fourier Shell Correlation (FSC) plots are shown next to the respective final maps.

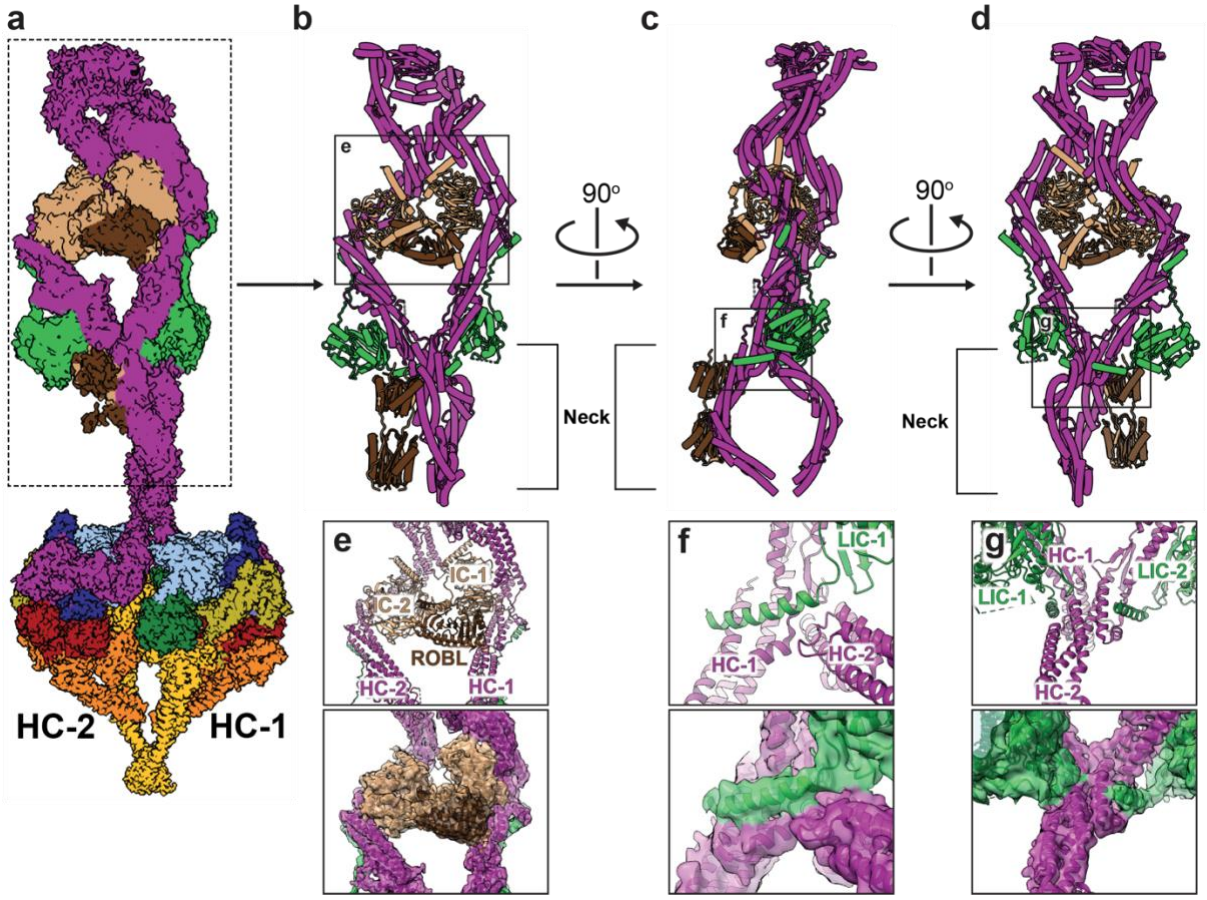

Supplementary Figure 4.4 Accessory chain interactions in Phi dynein. a. Front view of the cryo-EM map of the motor and tail regions of Phi dynein. The heavy chain (HC) associated with each dynein monomer is highlighted for orientation. **b-d**. The model for the Phi dynein tail is shown in three orientations: (**b**) front view, (**c**) side view, and (**d**) back view. The neck region, which is the focus of panels (e) – (f) is highlighted. The black boxes indicate regions where our map revealed new interactions between accessory chains, and between them and dynein's heavy chain, with labels indicating the corresponding panels below (**e-g**). **e-g**. Close-up views of the three new interactions identified in our map, with the top panel displaying the model and the bottom panel showing the corresponding cryo-EM map, highlighting connecting densities. The numbering of the accessory chains reflects the heavy chain with which they are associated. **e**. Both intermediate chains (IC-1 and IC-2) interact with the light chain ROBL. **f**. Both light intermediate chains (LIC-1 and LIC-2) interact with their respective heavy chains (HC-1 and HC-2). **g**. LIC-1 interacts with both HC-1 and HC-2.

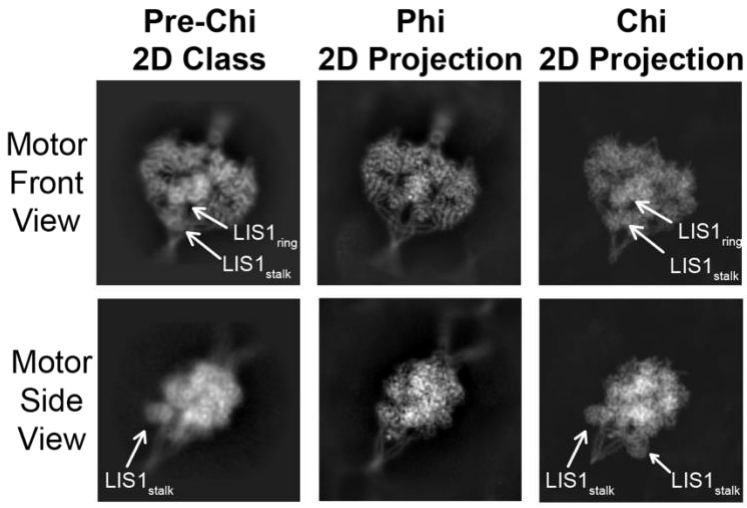

Supplementary Figure 4.5 Comparison of 2D class averages for Pre-Chi with previously known dynein models. Projection matching between experimental class averages of Pre-Chi with projections from models of Phi and Chi.

ATP
ATP + Mg^{2+}
ADP + Mg^{2+}
ADP

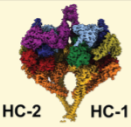

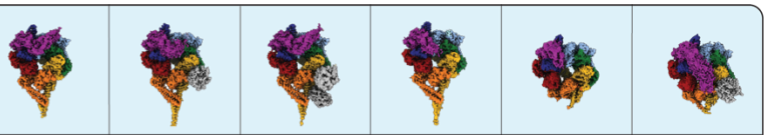

Class	Phi motor		Bent	Bent+1xLIS1	Bent+2xLIS1	Interm.	Straight	Straight+2xLIS1
resol. (Å)	2.7		3.2	3.2	3.1	3.4	3.4	3.3
LIS1	0		0	1	2	0	0	1
Linker	HC-1 Bent	HC-2 Bent	Bent	Bent	Bent	Intermediate	Straight	Straight
Stalk	β	β	β	β	β	β	α	α
AAA1	○	○	○	○	○	○	○	○
AAA2	●	●	●	●	●	●	●	●
AAA3	○	○	○	○	○	○	●	●
AAA4	○	○	○	○	○	○	○	○

Supplementary Figure 4.6 Conformations and nucleotide states of the Phi and Open motor domains. The table summarizes the conformations and nucleotide states of the Phi (yellow background) and Open (blue background) motor domains presented in this work. "LIS1" indicates how many LIS1 β-propellers are bound to the dynein motor. "Linker" refers to the overall conformation (bent, intermediate, straight) of that domain. "Stalk" refers to the register between the two helices in the coiled-coil [4]. The nucleotide states of AAA1-AAA4 are based on our interpretation of the densities in our maps.

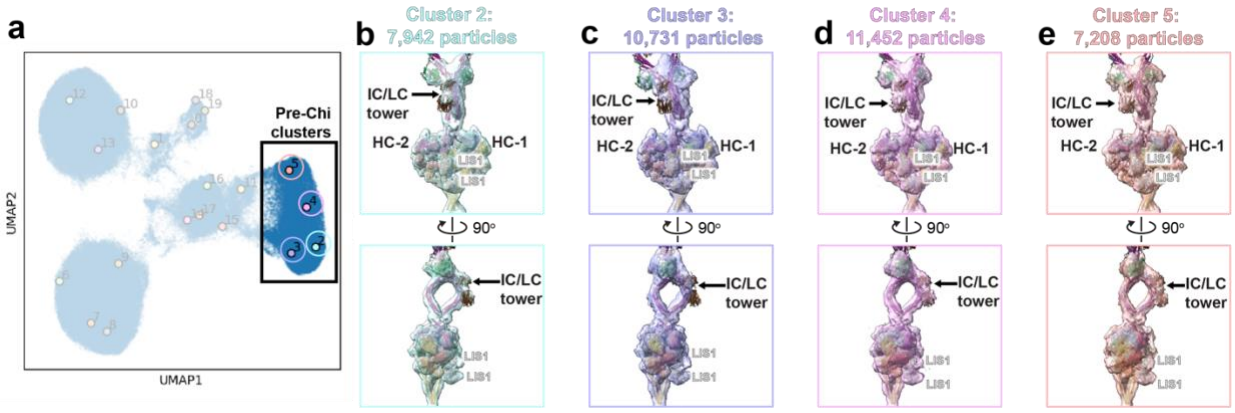

Supplementary Figure 4.7 LIS1 binds preferentially to one face on the Pre-Chi structure. a. cryoDRGN UMAP representation. This analysis focuses on the Pre-Chi k means clusters 2-5 (highlighted by the box) from Extended Data Fig 3. **b-e.** Volumes from clusters 2-5 shown in two views: front view of the IC/LC tower face (top row) and side view (bottom row). The IC-LC tower (labeled) is used as a reference to determine which side of Phi LIS1 is bound to.

4.5 Tables

Table 4.1 Cryo-EM data information and model validation statistics.

Description										
Sample	Full-length Human Cytoplasmic Dynein-1 + Human LIS1 in the presence of 1mM ATP									
Class Name	Pre-Chi Motor	Pre-Chi Tail	Phi Motor	Phi Tail	Bent /2xLIS1	Bent	Bent. /1xLIS1	Interm.	Straight /1xLIS1	Straight
EMD-	47342	47430	47373	47443	47370	47360	47372	47371	47429	47377
PDB-	9DZY	9E23	9E0X	9E28	9E0T	9E0K	9E0W	9E0U	9E22	9E0Y
Data collection and processing										
Facility	UC San Diego Cryo-EM facility									
Microscope	Titan Krios G4									
Voltage(kV)	300									
Camera	Falcon 4									
Magnification	130,000									
Electron exposure (e/Å^2)	55									
Defocus range (μm)	0.6-3.3									
Pixel size (Å)	0.935									
Symmetry imposed	C1									
Images (no.)	11,686									
Initial particles (no.)	1,937,842									
Final particles (no.)	66880	12517	161043	21400	23289	22570	26127	13958	69831	50952
Map resolution (Å) (FSC 0.143)	3.1	6.2	2.7	4.4	3.1	3.2	3.2	3.4	3.3	3.4
Refinement										
Initial model used (PDB code)	5NUG, 8DYU	8PTK	5NUG	8PTK	8DYU	8DYU	8DYU	8DYU	8PQV, 8DYU	8PQV
Model resolution (Å) (FSC 0.5)	3.3	7.5	2.9	6.5	3.5	3.6	3.6	3.8	3.8	4.3

Table: 4.1 Cryo-EM data information and model validation statistics. (Contiuned)

Map sharpening *B* factor (Å^2)	50.3	342	67.4	47.3	35.8	29.1	37	17	47.5	37.5
Model composition										
Non-hydrogen atoms	51122	21249	46234	21249	27918	22930	24531	22051	24612	22201
Protein residues	6466	4734	5840	4734	3518	2892	3095	2783	3245	2753
Ligands	MG:4, ADP:6, ATP:2	-	MG:4, ADP:6, ATP:2	-	MG:2, ADP:3, ATP:1	MG:2, ADP:3, ATP:1	MG:2, ADP:3, ATP:1	MG:2, ADP:3, ATP:1	MG:1, ADP:2, ATP:2	ADP:2, ATP:2
***B* factors (Å^2)**										
Protein	123.0	564.5	71.5	445.1	164.1	104.9	114.0	130.8	154.9	207.5
Ligand	94.38	-	37.7	-	115.4	72.7	66.1	84.1	85.3	141.7
R.m.s. deviations										
Bond lengths (Å)	0.004	0.002	0.003	0.002	0.003	0.003	0.003	0.004	0.003	0.004
Bond angles (°)	0.651	0.484	0.640	0.481	0.644	0.644	0.611	0.673	0.627	0.764
Validation										
MolProbity score	1.57	1.93	1.37	1.68	1.57	1.56	1.58	1.53	1.45	1.74
Clash score	6.05	8.75	4.60	4.24	6.46	5.81	6.21	5.65	5.09	7.49
Rotamer outliers (%)	0	0	0.04	0	0.03	0.04	0.04	0	0	0.04
Ramachandran plot										
Outliers (%)	0.02	0.13	0.03	0.11	0	0	0	0	0	0
Allowed (%)	3.58	7.14	2.71	7.48	3.39	3.60	3.62	3.45	3.06	4.77
Favored (%)	96.41	92.73	97.25	92.41	96.61	96.40	96.38	96.55	96.91	95.23

4.6 References

1. Karasmanis EP, Reimer JM, Kendrick AA, Nguyen KHV, Rodriguez JA, Truong JB, Lahiri I, Reck-Peterson SL, Leschziner AE. Lis1 relieves cytoplasmic dynein-1 autoinhibition by acting as a molecular wedge. *Nat. Struct. Mol. Biol.* **30**, 1357–1364 (2023).
2. Punjani, A., Rubinstein, J. L., Fleet, D. J. & Brubaker, M. A. cryoSPARC: algorithms for rapid unsupervised cryo-EM structure determination. *Nat. Methods* **14**, 290–296 (2017).
3. Zhong, E. D., Bepler, T., Berger, B. & Davis, J. H. CryoDRGN: reconstruction of heterogeneous cryo-EM structures using neural networks. *Nat. Methods* **18**, 176–185 (2021).
4. Kinman, L. F., Powell, B. M., Zhong, E. D., Berger, B. & Davis, J. H. Uncovering structural ensembles from single-particle cryo-EM data using cryoDRGN. *Nat. Protoc.* **18**, 319–339 (2023).
5. Zhang K, Foster HE, Rondelet A, Lacey SE, Bahi-Buisson N, Bird AW, Carter AP. Cryo-EM Reveals How Human Cytoplasmic Dynein Is Auto-inhibited and Activated. *Cell* **169**, 1303-1314.e18 (2017).
6. Marzo, M. G., Griswold, J. M. & Markus, S. M. Pac1/LIS1 stabilizes an uninhibited conformation of dynein to coordinate its localization and activity. *Nat. Cell Biol.* **22**, 559–569 (2020).
7. Reimer, J. M., DeSantis, M. E., Reck-Peterson, S. L. & Leschziner, A. E. Structures of human dynein in complex with the lissencephaly 1 protein, LIS1. *eLife* **12**, e84302 (2023).
8. Simoes C, Graña M, Rodriguez S, Baltar Yanes F, Tapié A, Dell'Oca N, Naya H, Raggio V, Spangenberg L. Novel frameshift mutation in LIS1 gene is a probable cause of lissencephaly: a case report. *BMC Pediatr.* **22**, 545 (2022).
9. Elshenawy MM, Kusakci E, Volz S, Baumbach J, Bullock SL, Yildiz A. Lis1 activates dynein motility by modulating its pairing with dynactin. *Nat. Cell Biol.* **22**, 570–578 (2020).
10. Htet ZM, Gillies JP, Baker RW, Leschziner AE, DeSantis ME, Reck-Peterson SL. LIS1 promotes the formation of activated cytoplasmic dynein-1 complexes. *Nat. Cell Biol.* **22**, 518–525 (2020).
11. Wang, S. & Zheng, Y. Identification of a novel dynein binding domain in nudel essential for spindle pole organization in Xenopus egg extract. *J. Biol. Chem.* **286**, 587–593 (2011).
12. Zhao, Y., Oten, S. & Yildiz, A. Nde1 promotes Lis1-mediated activation of dynein. *Nat. Commun.* **14**, 7221 (2023).
13. Moon HM, Youn YH, Pemble H, Yingling J, Wittmann T, Wynshaw-Boris A. LIS1 controls mitosis and mitotic spindle organization via the LIS1–NDEL1–dynein complex. *Hum. Mol. Genet.* **23**, 449–466 (2014).
14. Zyłkiewicz E, Kijańska M, Choi WC, Derewenda U, Derewenda ZS, Stukenberg PT. The N-terminal coiled-coil of Ndel1 is a regulated scaffold that recruits LIS1 to dynein. *J. Cell Biol.* **192**, 433–445 (2011).
15. Gillies JP, Reimer JM, Karasmanis EP, Lahiri I, Htet ZM, Leschziner AE, Reck-Peterson SL. Structural basis for cytoplasmic dynein-1 regulation by Lis1. *eLife* **11**, e71229 (2022).
16. Kendrick AA, Nguyen KHV, Ma W, Karasmanis EP, Amaro RE, Reck-Peterson SL, Leschziner AE. Multiple steps of dynein activation by Lis1 visualized by cryo-EM. *Nat Struct Mol Biol* (2025).
17. Singh K, Lau CK, Manigrasso G, Gama JB, Gassmann R, Carter AP. Molecular mechanism of dynein-dynactin complex assembly by LIS1. *Science* **383**, eadk8544 (2024).
18. Baumbach J, Murthy A, McClintock MA, Dix CI, Zalyte R, Hoang HT, Bullock SL. Lissencephaly-1 is a context-dependent regulator of the human dynein complex. *eLife* **6**, e21768 (2017).
19. Schlager, M. A., Hoang, H. T., Urnavicius, L., Bullock, S. L. & Carter, A. P. In vitro reconstitution of a highly processive recombinant human dynein complex. *EMBO J.* **33**, 1855–1868 (2014).
20. Nguyen, H. P. M., McGuire, K. L., Cook, B. D. & Mark A. Herzik, J. Manual Blot-and-Plunge Freezing of Biological Specimens for Single-Particle Cryogenic Electron Microscopy. *JoVE J. Vis. Exp.* e62765 (2022) doi:10.3791/62765.
21. Bepler, T., Kelley, K., Noble, A. J. & Berger, B. Topaz-Denoise: general deep denoising models for cryoEM and cryoET. *Nat. Commun.* **11**, 5208 (2020).
22. Scheres, S. H. W. Chapter Six - Processing of Structurally Heterogeneous Cryo-EM Data in RELION. in *Methods in Enzymology* (ed. Crowther, R. A.) vol. 579 125–157 (Academic Press, 2016).
23. Pettersen EF, Goddard TD, Huang CC, Meng EC, Couch GS, Croll TI, Morris JH, Ferrin TE. UCSF ChimeraX: Structure visualization for researchers, educators, and developers. *Protein Sci.* **30**, 70–82 (2021).
24. Afonine PV, Poon BK, Read RJ, Sobolev OV, Terwilliger TC, Urzhumtsev A, Adams PD. Real-space refinement in PHENIX for cryo-EM and crystallography. *Acta Crystallogr. Sect. Struct. Biol.* **74**, 531–544 (2018).
25. Emsley, P., Lohkamp, B., Scott, W. G. & Cowtan, K. Features and development of Coot. *Acta Crystallogr. D Biol. Crystallogr.* **66**, 486–501 (2010).

26. Mirdita M, Schütze K, Moriwaki Y, Heo L, Ovchinnikov S, Steinegger M. ColabFold: making protein folding accessible to all. *Nat. Methods* **19**, 679–682 (2022).
27. Jumper J, Evans R, Pritzel A, Green T, Figurnov M, Ronneberger O, Tunyasuvunakool K, Bates R, Žídek A, Potapenko A, Bridgland A, Meyer C, Kohl SAA, Ballard AJ, Cowie A, Romera-Paredes B, Nikolov S, Jain R, Adler J, Back T, Petersen S, Reiman D, Clancy E, Zielinski M, Steinegger M, Pacholska M, Berghammer T, Bodenstein S, Silver D, Vinyals O, Senior AW, Kavukcuoglu K, Kohli P, Hassabis D. Highly accurate protein structure prediction with AlphaFold. *Nature* **596**, 583–589 (2021).
28. Toropova K, Zou S, Roberts AJ, Redwine WB, Goodman BS, Reck-Peterson SL, Leschziner AE. Lis1 regulates dynein by sterically blocking its mechanochemical cycle. *eLife* **3**, e03372 (2014).
29. Roberts, A. J., Goodman, B. S. & Reck-Peterson, S. L. Reconstitution of dynein transport to the microtubule plus end by kinesin. *eLife* **3**, e02641 (2014).

4.7 Acknowledgement

Chapter 4, in full, has been accepted for publication in *Nature Communications* as *Cryo-EM captures early intermediate steps in dynein activation by LIS1*. Nguyen, K.H.V.; Karasmanis, E.P.; Kendrick, A.A.; Reck-Peterson, S.L.; Leschziner, A.E. The dissertation author was the first author and primary contributor to this work.

Chapter 5: Conclusions and future directions

5.1 Regulation of dynein activation by LIS1

The work presented in this thesis provides significant progress in understanding LIS1 and its role in regulating dynein activation. In chapters 2 and 4, I presented two novel structures (Chi and Pre-Chi) that were determined, providing a mechanistic insight into how Phi autoinhibition in the motor domain is initially relieved by LIS1. By functionally testing the structures of Chi and Pre-Chi, we found that both are involved in dynein activation by LIS1. An apparent paradox is that while these structures are intermediates in dynein's activation, dynein is still in an autoinhibited state, since these structures replace dynein-dynein interactions in Phi with dynein-LIS1-dynein interfaces in Chi or Pre-Chi. In addition, the structures solved to date do not provide information on the change in the tail of dynein, which is essential for the dynein assembly process. So, how does dynein reach the conformation required to be assembled into a DDA complex? In the work presented in Chapter 3, we found that LIS1 binding to the dynein motor domain increases dynein's basal ATPase activity, and this relates to the increased number of conformations observed by cryo-EM in the dynein-LIS1 samples compared to dynein alone. I hypothesize that LIS1 has two roles for dynein activation: 1) LIS1 binding to Phi dynein relieves autoinhibition in the motor domain, and 2) once dynein is relieved by LIS1 in the motor domain, LIS1 increases dynein's conformational sampling by increasing its basal ATPase activity. Eventually, this allows dynein to associate with dynactin and an activating adaptor to form active transport complexes.

5.2 Regulation of dynein assembly by LIS1

Beyond its role in dynein activation, a recent microtubule-bound dynein/ dynactin structure containing the activating adaptor JIP3 (DDA-LIS1) shows that LIS1 also facilitates the coordination of dynein and dynactin for DDA complex assmebly[1]. In this complex, the N-terminus of LIS1 further stabilizes the interaction between dynein and dynactin's p150 subunit, highlighting LIS1's role in promoting DDA assembly on microtubules. This observation also suggests the existence of upstream DDA-LIS1 intermediate species.

In the dataset collected in Chapter 4, we observed a very low population of 2D class averages that showed a larger separation between the dynein linkers than we had seen in either the Pre-Chi or Chi intermediates (Fig. 5.1a). We termed this "Post-Chi" and we performed 2D projection matching by comparing the 2D projections from Phi and Chi to the identified 2D class averages (Fig 5.1b). However, we could not confidently determine if LIS1 is present in these 2D class averages, even though the dynein motors are not in the Phi conformation but appear to interact with each other. Given the significant separation of the linker, I hypothesize that the unresolved tail portion is undergoing the conformational rearrangements that had not taken place in Pre-Chi or Chi and that are required for dynein to be able to interact with dynactin. Furthermore, LIS1's coordination with dynactin at the tail of dynein may help stabilize the transition of Phi dynein from its autoinhibited conformation to a parallel tail arrangement that is compatible with microtubule binding and subsequent association with an activating adaptor.

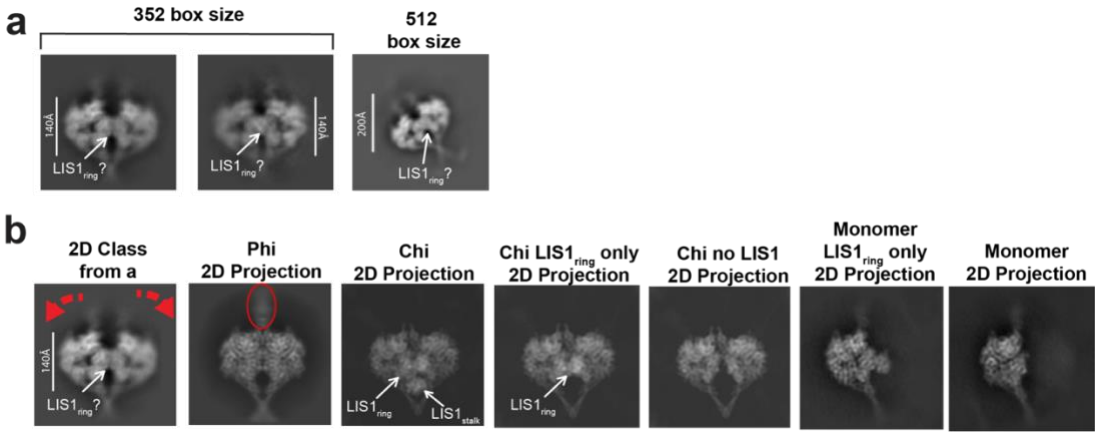

Figure 5.1. 2D class average of Post-Chi. a, 2D class average suggests a potential human Post-Chi dynein-LIS1 complex. The potential LIS1$_{ring}$ binding site is highlighted in white. **b,** 2D projection matching from the 2D class average from panel a, with Phi, Chi, and dynein monomer projection. LIS1 is highlighted in white. Red arrows in "2D Class from a" show the separation of dynein's linkers compared to the red circle in "Phi 2D Projection", which shows the linkers interact.

To capture the symmetry transition in the full-length dynein tail and to see if dynactin stabilizes the tail transition, I propose building on our established conditions of using human full-length dynein, LIS1, and ATP that yielded the Pre-Chi state and Post-Chi. From this foundation, we can introduce dynactin and an activating adaptor, both in the presence and absence of microtubules. This approach will allow us to capture later intermediate states representing the transition from Pre-Chi to fully assembled DDA complexes on microtubules.

5.3 Nde1 role in regulation of dynein activation and assembly

Another key dynein regulator is Nde1/Ndel1 (hereafter referred to as Nde1), which functions exclusively within the LIS1-mediated dynein activation pathway. Nde1 is essential for various dynein-dependent processes, including cargo transport, cell division, and neuronal migration[2]. It contains an N-terminal coiled coil domain that interacts with the N terminus of dynein intermediate chain (IC), and a disordered C-terminal region[3]. Beyond its interaction with dynein, Nde1 binds directly to the β-propeller of LIS1, the same region that engages the dynein

motor domain[4]. Like LIS1, depletion of Nde1 severely disrupts dynein-mediated transport[5,6]. Notably, the defects caused by Nde1 loss can be rescued by LIS1 overexpression or exogenous LIS1 addition, whereas Nde1 overexpression cannot rescue LIS1 deletion[7,8]. This shows that Nde1's function depends entirely on LIS1 and supports a mechanism in which Nde1 tethers LIS1 to dynein[4,8–10]. This tethering would bring LIS1 into proximity with the dynein motor domain in the Phi state, increasing its local concentration. This enables LIS1 to more effectively relieve dynein's autoinhibition and promote activation[4]. The tethering model is further supported by recent in vitro studies on Nde1, showing that it positively regulates dynein by tethering LIS1 and negatively regulates it by competing against binding with p150 of dynactin[4,11].

Furthermore, this tethering model is supported through structural data. Recently, another group obtained a Pre-Chi in their cryo-EM dataset[12]. Interestingly, when they added Nde1 into this full-length human dynein with LIS1, they found that the Pre-Chi population became the dominant population in the dataset and did not observe any Phi populations. Even though Nde1 is in the sample, they could not resolve any features of Nde1 in their Pre-Chi structure. This indicates that Nde1 may be transiently interacting with dynein's IC or fully dissociated by this point. The enrichment of Pre-Chi in the presence of Nde1 supports the model of having Nde1 tether LIS1 to dynein, enhancing LIS1 binding to a Phi dynein and priming this complex for downstream intermediate species. I hypothesize that after Nde1 delivers and tethers LIS1 to dynein, it likely dissociates from the complex to allow dynein assembly to occur. This dissociation would free the N-terminus of dynein's intermediate chain (IC), which is necessary to relieve dynactin's p150 from autoinhibition. Notably, there is no evidence that Nde1 directly relieves dynein autoinhibition as LIS1 does, suggesting its primary role is to recruit and tether LIS1 to dynein rather than regulate dynein's conformational state.

5.4 Concluding remarks

In summary, the results presented in this thesis provide a detailed mechanistic understanding of how LIS1 enhances dynein activation and assembly. We have identified two novel intermediate dynein-LIS1 complexes (Pre-Chi and Chi), and, by validating these structures with functional assays, we placed both structures along the dynein activation pathway. Furthermore, heterogeneity mining analyses revealed that LIS1 increases the distinct dynein conformational states observed in cryo-EM. While we cannot determine the full range of conformations dynein can sample, our analysis showed that LIS1 enhances dynein's basal ATPase rate. These findings significantly advance our understanding of LIS1's regulatory role in dynein activation and lay the groundwork for future studies on how LIS1 facilitates the assembly of dynein into an active transport complex.

5.5 References

1. Singh K, Lau CK, Manigrasso G, Gama JB, Gassmann R, Carter AP. Molecular mechanism of dynein-dynactin complex assembly by LIS1. *Science* **383**, eadk8544 (2024).
2. Reck-Peterson, S. L., Redwine, W. B., Vale, R. D. & Carter, A. P. The cytoplasmic dynein transport machinery and its many cargoes. *Nat. Rev. Mol. Cell Biol.* **19**, 382–398 (2018).
3. Bradshaw, N. J., Hennah, W. & Soares, D. C. NDE1 and NDEL1: twin neurodevelopmental proteins with similar 'nature' but different 'nurture'. *Biomol. Concepts* **4**, 447–464 (2013).
4. Zhao, Y., Oten, S. & Yildiz, A. Nde1 promotes Lis1-mediated activation of dynein. *Nat. Commun.* **14**, 7221 (2023).
5. Pandey, J. P. & Smith, D. S. A Cdk5-Dependent Switch Regulates Lis1/Ndel1/Dynein-Driven Organelle Transport in Adult Axons. *J. Neurosci.* **31**, 17207–17219 (2011).
6. Lam, C., Vergnolle, M. A. S., Thorpe, L., Woodman, P. G. & Allan, V. J. Functional interplay between LIS1, NDE1 and NDEL1 in dynein-dependent organelle positioning. *J. Cell Sci.* **123**, 202–212 (2010).
7. Efimov, V. P. Roles of NUDE and NUDF Proteins of Aspergillus nidulans: Insights from Intracellular Localization and Overexpression Effects. *Mol. Biol. Cell* **14**, 871–888 (2003).
8. Wang, S. & Zheng, Y. Identification of a Novel Dynein Binding Domain in Nudel Essential for Spindle Pole Organization in *Xenopus* Egg Extract*. *J. Biol. Chem.* **286**, 587–593 (2011).
9. Zyłkiewicz E, Kijańska M, Choi WC, Derewenda U, Derewenda ZS, Stukenberg PT. The N-terminal coiled-coil of Ndel1 is a regulated scaffold that recruits LIS1 to dynein. *J. Cell Biol.* **192**, 433–445 (2011).
10. Moon HM, Youn YH, Pemble H, Yingling J, Wittmann T, Wynshaw-Boris A. LIS1 controls mitosis and mitotic spindle organization via the LIS1–NDEL1–dynein complex. *Hum. Mol. Genet.* **23**, 449–466 (2014).
11. Garrott SR, Gillies JP, Siva A, Little SR, El Jbeily R, DeSantis ME. Ndel1 disfavors dynein–dynactin–adaptor complex formation in two distinct ways. *J. Biol. Chem.* **299**, 104735 (2023).
12. Yang, J., Zhao, Y., Chai, P., Yildiz, A. & Zhang, K. Nde1 Promotes Lis1 Binding to Full-Length Autoinhibited Human Dynein-1. 2024.12.30.630764 Preprint at https://doi.org/10.1101/2024.12.30.630764 (2025).